Final Technical Report

COVER PAGE

Federal Agency to which Report is submitted: DOE NE – Nuclear Energy University Program

Recipient: University of Florida
Award Number: DE-NE0008523
Project Title: Phase Transformation of Thermally Aged and Neutron Irradiated Duplex Stainless Steels used in LWRs
Project Period: 10/1/2016 to 12/31/2019

Principle Investigator: Yong Yang, University of Florida, yongyang@ufl.edu, 352-846-3791
Report Submitted by: Yong Yang, University of Florida, yongyang@ufl.edu, 352-846-3791

Date of Report: January 30, 2020
Covering Period: 10/1/2016 to 12/31/2019
Report Frequency: Final

Collaborator: Jeff Terry, Illinois Institute of Technilogy, terryj@iit.edu
Yiren Chen, Argonne National Laboratory, yiren_chen@anl.gov

Cost-Sharing Partners: NA

DOE Project Team: DOE TPOC – Stu Maloy
DOE Federal Reviewer –

Signature of Submitting Official:

(electronic signature is acceptable)

Executive Summary

The lifetime of reactor components made of duplex stainless steels can be limited by the embrittlement from thermal aging, neutron irradiation or a synergistic effect between thermal aging and neutron irradiation. There is still a large scientific knowledge gap in understanding the phase evolution in duplex stainless steels upon thermal aging with or without neutron irradiation, the synergistic effect between thermal aging and neutron irradiation, and the impacts of structural evolution on material mechanical responses.

Previous studies showed that the spinodal decomposition in the delta ferrite phase is a primary embrittlement mechanism of the duplex structure stainless steels, while the G-phase precipitates were also identified. Most of the past studies focused on characterizations of fine-scale precipitates and phase decomposition using transmission electron microscopy and atom probe tomography. The fundamental mechanism and kinetics of elemental segregations occurring in the ferrite has not been fully understood. The exact concurrent evolution mechanism of the solute clustering and spinodal decomposition is not clear. This knowledge gap has hindered the development of thermodynamics and kinetic modeling of microstructural evolution. It was also speculated that the cracks initiate in hardened ferrites and then propagate along the phase boundaries between ferrite and austenite. In addition, the fundamental mechanism of how the microstructural changes decrease materials' fracture toughness is yet to be determined, which is needed for constructing a physical model to predict materials' mechanical response in the extended reactor lifetime.

In this project, we utilize the capability of high energy X-ray facility at the MRCAT (APS/ANL), including X-ray diffraction (XRD), Extended X-ray Absorption Fine structure Spectroscopy (EXAFS) and in-situ tensile test with wide angle X-ray scattering (WAXS) to probe the elemental segregations, phase precipitations and strain status of different phases in selected CASS and welds. Particularly, the in-situ tensile tests to provide insights, for the first time in the duplex structure steels, the evolutions of micro-straining response of each individual phase, lattice strain mismatch and the loading partition between the hardened ferrite and austenitic matrix upon different thermal aging conditions. The X-ray studies were complemented by microstructural characterizations includes transmission electron microscopy (TEM) and atom probe tomography (APT) to correctly interpret the data from X-ray diffraction and scattering. In addition, finite element modeling was used to understand the load partition and transfer between two phases and to explore the future predictive model development. The following list three major objectives achieved through the project.

OBJECTIVES:

1. Complemented by the TEM/APT studies and ex-situ mechanical tests on duplex stainless steels from our existing research program, the results from X-ray diffraction/EXAFS/WAXS in-situ tensile test will provide an unprecedented multi-scale understanding on phase separations, precipitate nucleation and growth,

and lattice straining of different phases in the thermally aged and/or neutron irradiated duplex stainless steels.
2. Determine whether there is a strong synergistic effect between thermal aging and neutron irradiation from the view point of elemental diffusion and segregation at an atomic scale.
3. Support the LWRS program by provide a more accurate picture of how the CASS and welds perform over the extended service lifetime.

In total, five major tasks were completed through this project: a) the in-situ WAXS tensile tests of thermally aged cast duplex stainless steels, b) the EXAFS investigation of thermally aged cast austenitic stainless steel and welds of austenite sainless steel, c) the characterization of irradiation effect on neutron irradiated CASS using APT, d) characterize the ferrite hardening of neutron irradiated CASS using nanoindentation, and e) the FEM modelling to validate the in-situ WAXS tensile tests and to simulate the stress/strain distribution during deformation for thermally aged duplex stainless steel.

The in-situ WAXS tensile test are used to investigate the lattice response for both phases separately, thus, to analyze the mechanical characteristics of the thermally aged 1000-hours and 3000-hours duplex stainless steels in comparison to the unaged samples. The FEM modelling can be applied not only to validate the WAXS results but also can simulate the stress/strain distribution during deformation for aged/unaged CASS. The APT microstructural characterization provides insight into quantification of irradiation induced spinodal decomposition and G-phase precipitation that have substantial influences on the mechanical properties. The quantification results from APT characterization were further utilized in calculating the ferrite hardening which was compared with the nanoindentation hardness reuslt. Based on the results from all these studies, the results are summarized in following.

Thermal Aging Effect on CASS

The unaged and thermally aged duplex stainless steels were tested to understand the thermal aging effect on duplex stainless steels. The thermal aging was conducted at 475°C for 400, 1000, and 3000 hours. The synchrotron X-ray diffraction technique was employed in combination with the uniaxial tensile testing to elucidate the mechanical responses for both austenite and ferrite phases. Both displacement-controlled and load-controlled straining tests were conducted on miniature tensile samples while WAXS measurements were performed in situ at different stress levels. The deformed samples were also characterized with TEM to validate the WAXS result.

1. On the macroscopic level, the thermal aging increases the tensile strength and decreases the ductility of the duplex stainless steel. In detail, the thermal aging at 475°C up to 1000 hours significantly increases the UTS of the duplex stainless from 661 MPa to 716 MPa. Additional aging time up to 3000 hours leads to a decrease of UTS as well as the strain hardening rate.

2. With the in-situ synchrotron XRD measurement, the evolution of lattice strains of both austenite and ferrite phases is investigated and the weighted average

strains for both austenite and ferrite phases are calculated. The lattice strain clearly show anisotropy. The {200} strain is always the largest regardless in the ferrite or austenite phases, with or without thermal aging. The lattice strains for austenite phase are stable regardless thermal aging condition. The lattice strains of ferrite phase, however, are almost two times higher in the aged than in the unaged samples.

3. The unaged austenite and ferrite phases yield at around 210 MPa and 315 MPa, respectively. After thermal aging, the yield strength of the austenite remains unchanged while the yield strength of ferrite increases with aging time and starts to saturate at around 436.5 MPa after 1000 hours. A longer thermal aging time beyond 1000 hours only gives rise to a limited increment in the yield strength of ferrite, but also induced pore formation at phase boundaries after the tensile test.

4. The difference of phase-specific average lattice strains between ferrite and austenite phases is not significant without thermal aging. When the applied stress is above the yield point of austenite phase but below the yield point of ferrite phase, the average strains for both austenite and ferrite increase with the applied stress. This indicates that although the ferrite may be stronger than the austenite, both phases carry the load imposed by the straining. After the thermal aging, the average strain of austenite increases with the stress much slower than that of ferrite phase. This indicate that the ferrite bears much more load than the austenite, and consequently, the load partition between ferrite and austenite becomes more extreme after thermal aging.

5. The dislocation density is analyzed using the modified W-H model. It shows the dislocation density of austenite phase evolves similarly during deformation with or without thermal aging. The dependence between the flow stress and dislocation density shows that the dislocation glide is the main deformation mode and the multiplication of dislocations is the major reason of strain hardening.

6. The evolution of dislocation density of ferrite phase during deformation shows that although the final dislocation density is similar for all samples with or without thermal aging, the dislocation density increases much faster in the aged than in the unaged specimens before reaching to a plateau. And the 3000-hours specimen reaches the plateau much earlier than 1000-hours specimen. The faster dislocation density multiplication at early deformation for 3000-hours specimen is likely to induce more severe load partition between ferrite and austenite, therefore, leading to pore formation at ferrite/austenite phase boundaries and early fracture during bulk tensile test.

Neutron Irradiation Effect on CASS

The APT characterization was used to investigate the neutron irradiation response of ferrite phase in CASS. Two specimens were irradiated at Halden reactor at around 307°C to a dose of 3 dpa (5.6×10^{19}n/cm^2, E>1 MeV with a dose rate of 5×10^{-8}dpa/s) while four other specimens were irradiated in the Bor-60 reactor to 5, 10,

20 and 40 dpa at temperature around 320°C with a dose rate of 7×10^{-7}dpa/s. Spinodal decomposition and G-phase variant were observed and analyzed. Based on the APT and TEM characterization results and comparisons with other literatures, the following conclusion can be drawn:

1. At irradiation dose around 3 dpa, neutron irradiation has dominated the microstructural evolution. Thermal aging prior to irradiation has negligible effect.
2. Irradiation to 5, 10, 20 and 40 dpa shows the appearance of spinodal decomposition. Based on quantification of wavelength and magnitude, the spinodal decomposition shows to saturate at 5 dpa. However, a significant boost in magnitude appears between 10 to 20 dpa, which can possibley be ascribed to the G-phase induced local compositional alternations.
3. Dose rate has a significant effect on spinodal decomposition:
   a) At a low dose rate, the RED is dominated, and the irradiation will enhance the spinodal decomposition.
   b) At a high dose rate, the defects annihilations occur at irradiation-induced sinks. The atoms in the Cr-rich phase will be re-mixded back to the matrix and the spinodal decomposition will be mediated.
   c) For ion irradiation, due to high knock-on energies, the ballistic mixing effect is more predominant and even can restrain the spinodal decomposition.
4. TEM diffraction patterns show the G phase structure has formed at 5 dpa.
5. A multi-stage G phase precipitation due to neutron irradiation is proposed:
   a) At 0-5 dpa, small G phase variant forms.
   b) At 5-10 dpa, the G phase variant grows, some matrix elements are absorbed which decrease the Ni, Si, Mn concentrations.
   c) At around 10 dpa, G phase precipitates reach a critical size, and the composition adjustment starts with rejecting the matrix atoms (Fe and Cr), thus the cluster size starts to decrease. The ejected matrix atoms further diffuse to Fe rich and Cr rich region thus significantly enhancing the magnitude of spinodal decomposition.
   d) Because of the limited solubility of Ni in Cr, once the spinodal decomposition happens, it first diffuses out of the Cr rich region and forms cluster at interdomain region. As Si has smaller size, it has a higher atomic mobility than Ni and Mn, therefore, Si reaches equilibrium almost as fast as Ni while the Mn takes a very long time to reach an equilibrium condition and it is still ongoing at 40 dpa.
6. The temperature, neutron irradiation dose and dose rate can all affect the size of G-phase:
   a) Higher temperature will induce large G-phase precipitates.
   b) Higher irradiation dose will induce large G-phase precipitates.
   c) Lower dose rate will induce large G-phase precipitates.
7. The correlation between nanoindentation hardness and microstructure evolution was calculated for neutron irradiated CASS to 20 and 40 dpa.

FEM Modelling on Thermally Aged Duplex Stainless Steel

2D FEM modelling including true stress-true strain curve modelling and stress/strain distribution modelling during deformation were performed on duplex

stainless steel w./wo. thermal aging. Based on the modelling result, following conclusion can be drawn:

1. The simulated true stress-true strain curves for unaged, aged 1000 hours and aged 3000 hours conditions show a great proximity to the experimental true stress-true strain curve, suggesting the material properties acquired from X-ray data analysis is accurate and useful.
2. The 2D stress/strain distribution modelling clearly shows the ferrite phase is holding a much higher stress than austenite phase, indicating a strong load partition phenomenon. The phenomen is also proved by the result from WAXS experiment.

EXAFS characterization on thermally aged CASS and welds of austenitic stainless steel

The EXAFS analysis is really challenging, particular for the dual phase materials as the phase volume percentages in the examined volume of materials pose a significant uncertaintity. The collected data hasn’t produced any quantitative results.

TABLE OF CONTENTS

page

LIST OF TABLES

Table page

LIST OF FIGURES

Figure page

LIST OF ABBREVIATIONS

1D, 2D, 3D	One dimensional, Two dimensional, Three dimensional
ANL	Argonne National Laboratory
APS	Advanced Photon Source
APT	Atom Probe Tomography
ATR	Advanced Test Reactor
BF	Bright Field
BCC	Body Centered Cubic
CAES	Center for Advanced Energy Studies
DF	Dark Field
dpa	Displacement per atom
DP	Diffraction Pattern
e.g.	for example
Eq.	Equation
FCC	Face Centered Cubic
FIB	Focused Ion Beam
Fig.	Figure
FWHM	Full Width at Half Maximum
GB	Grain Boundary
HCP	Hexagonal Close Packed
ICDD	International Center for Diffraction Data
INL	Idaho National Laboratory
LEAP	Local-Electrode Atom-Probe
MaCS	Materials Characterization Suite (CAES)
MAE	Mechanical and Aerospace Engineering

NE	Nuclear Engineering
PWR	Pressurized-Water Reactor
Ref.	Reference
RT	Room Temperature
SD	Standard Deviation
SEM	Scanning Electron Microscopy
SS	Stainless Steel
TEM	Transmission Electron Microscopy
UF	University of Florida
US	United States
UTS	Ultimate Tensile Stress
vs	Versus
WAXS	Wide-angle X-ray Scattering
WBDF	Weak-beam Dark-Field
W-H	Williamson-Hall
XRD	X-ray Diffraction

Background

1.1 Nuclear Energy Development and Materials Challenges

Nuclear Power Plant (NPP) has safely, reliably, and economically contributed almost 20% of the total amount of electricity generated in the United States over the past decades. More importantly, most NPPs are located in the vicinity of metropolises. They greatly satisfy the enormous electricity demand of these big cities. With the great benefits of nuclear power, significant research and development was investigated in the nuclear power and great achievement has been made. Since the Generation I reactor: designs (1950s-60s), which are mostly demonstrate reactor. The Generation II reactor designed in the 1960s achieved initial commercial operation from the 1970s through the 1990s. In 1990s Generation III reactor was designed and it incorporated significant advances in safety and economics. Nowadays, people are working on developing the next generation reactor: Generation IV reactors, which include the Very-High-Temperature Reactor (VHTR), Molten-Salt Reactor (MSR), Supercritical-Water-cooled Reactor (SCWR), Gas-cooled Fast Reactor (GFR), Sodium-cooled Fast Reactor (SFR), and the Lead-cooled Fast Reactor (LFR). Comparing with Generation II and III reactors, the Generation IV reactor has attributes like increased efficiency, increased safety and reduction in waste generation, nevertheless, Generation IV reactor is still under development or construction. Currently, the majority of NPPs under service are Generation II and III reactors.

Both pressurized water reactors (PWRs) and boiling water reactors (BWRs) are two predominant reactor design for Generation II reactor. They both operate at comparable temperature (~300 ℃) and similar radiation environment. Their major difference is that BWRs consist of a single water circuit designed for boiling to occur in the core with steam flowing directly to the turbine, which eliminates the steam generator and pressurizer found in the PWRs. Both types of design are utilizing the light water, therefore, both can be classified as Light Water Reactors (LWRs).

At present, most commercial LWRs have been served for almost 60 years, it is worthwhile to extend their lifetime to another 20 years considering the cost of building a new NPP. Extending the lifetime of Light Water Reactors demands a high integrity of materials and components in reactors. Therefore, an accurate prediction of material's performance under anticipated operation conditions is of particular importance to ensure the safety of nuclear power plants over their extended lifetime.

1.2 The application of duplex stainless steels in LWRs

Stainless steels are very important to our society considering plenitude of applications that rely on their use. The application ranges are so wide that LWRs are not excepted. Stainless steels may be classified by their crystalline structure into four main types: austenitic, ferritic, martensitic, and duplex. Different stainless steel has their own advantages. The austenitic stainless steel is the most widely used stainless steel because of its good formability and corrosion resistance. Comparing with austenitic stainless steel, the ferritic stainless usually has a higher strength as well as a better

stress corrosion cracking resistance. For martensitic stainless steel, it has the highest strength but poor ductility. As for duplex stainless steel, since it has two crystalline structures, it usually has a good combination of the properties of both structures. Among all the different duplex stainless steels: ferritic-austenitic, martensitic-ferritic, and ferritic-martensitic in the market, ferritic-austenitic stainless steel is the one that is most widely applied. The CF-3 cast duplex stainless steel is one of the ferritic-austenitic stainless steel that are widely used in the LWRs as structural materials. A general description of the various types of steels used in LWRs is shown in Figure 1-1. For CF-3 CDSS, it is mostly applied at the primary pressure boundary components, such as, coolant pipes, elbows, valve bodies and pump casings. The predominant reason for choosing CDSS in LWRs is because of its excellent corrosion resistance.

Both the CASS and welds of austenitic stainless steel are duplex stainless steels. They are featured with a duplex structure that consists of α-ferrite and γ-austenite phase. The ferrite contents improve the tensile strength and stress corrosion cracking resistance while the austenite contents improve the ductility and corrosion.

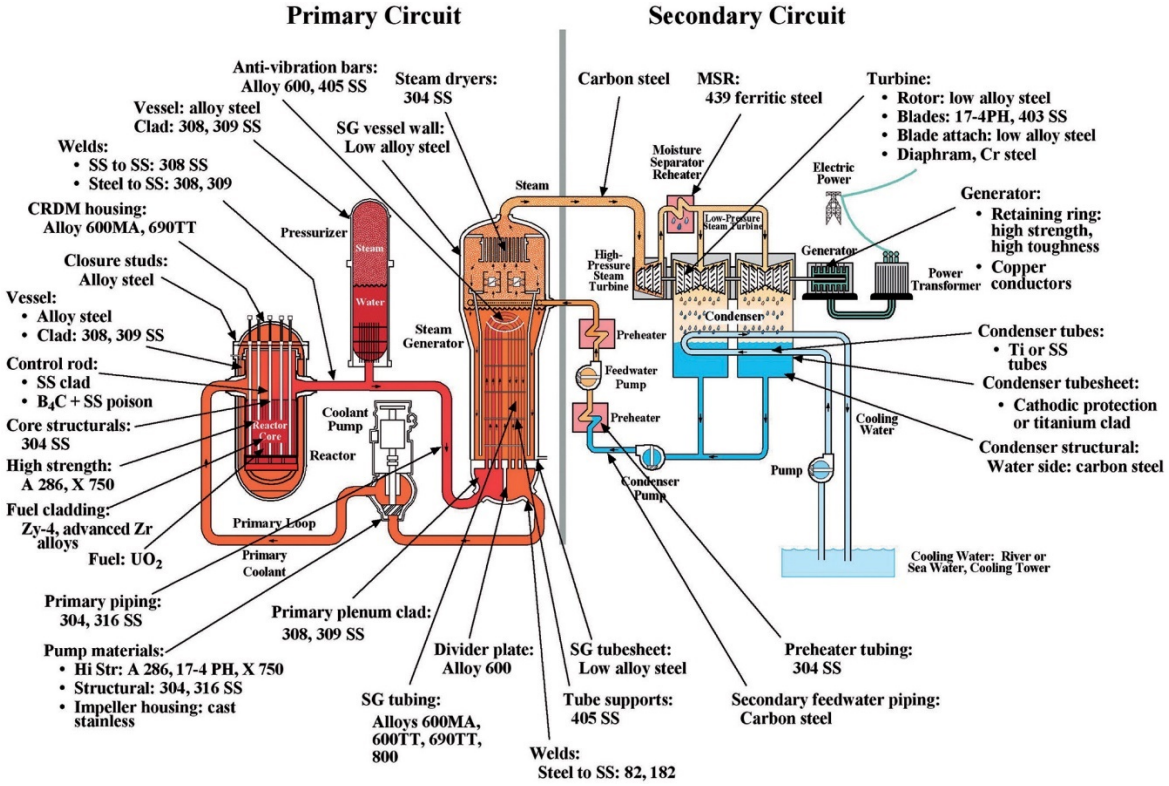

Figure 1-1. Various types of steels used in PWRs.

1.3 Introduction of cast austenitic stainless steel

1.3.1 Formation of cast austenitic stainless steel

Like shown in Figure 1-2, the CASS usually contains around 20%Cr and 10% Ni, which judging from the phase diagram, if the alloy in the liquid state is cooled extremely slowly (approaching equilibrium solidification), the final structure should be 100% γ-austenite. However, the equilibrium condition never occurs in reality, and the final

microstructure of CASS is duplex structure: the matrix is γ-austenite while the δ-ferrite is island shape within the austenite matrix.

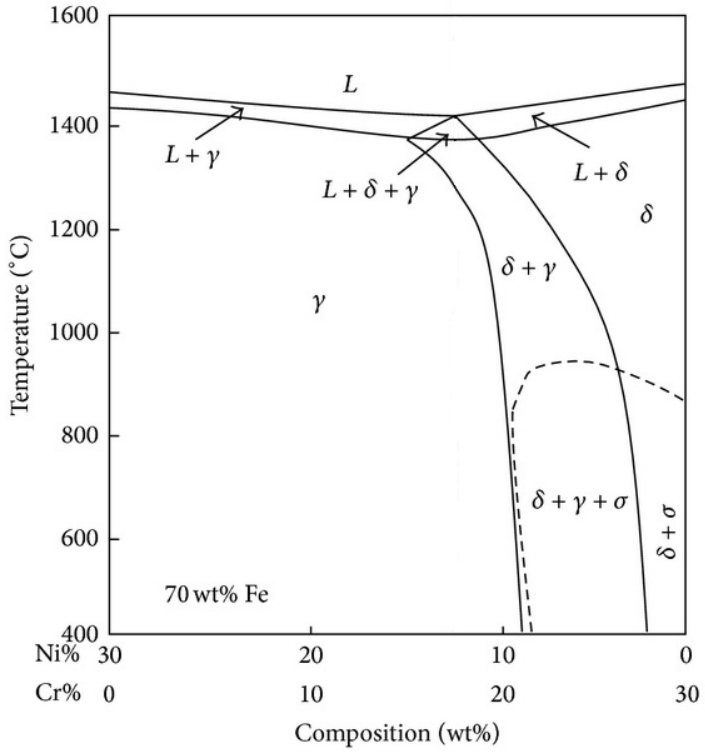

Figure 1-2. The Fe-Cr-Ni phase diagram.

1.3.2 Crystallographic structure difference between austenite and ferrite

γ-austenite phase has a F.C.C. structure, with lattice parameter around 3.598 Å while the δ-ferrite phase has a B.C.C. structure with lattice parameter around 2.865 Å. For F.C.C. structure, {111} type planes are the close-packed planes. Since the close-packed plane has the smallest lattice spacing, less activation energy is required for slip to occur compared with other planes. Each close-packed plane contains three <110> slip directions, therefore, F.C.C. structure has 12 slip systems in total. For B.C.C. structure, it is well known that it does not have close-packed planes but has close packed direction <111>. The slip can happen in {110}, {112} and {123} planes with <111> direction. There are 6 possible {110} planes, 12 possible {112} planes and 12 possible {123} planes respectively. For each {110} plane two <111> directions are possible while one possible <111> direction for the {112} and {123} planes, therefore, all together 48 slip systems for B.C.C. structure [1].

Overall, because of the difference in crystal structure, the ferrite and austenite have a different property. For austenite, since F.C.C. structure has close packed plane and direction, it is more likely to slip when the load is applied. Therefore, austenite

phase has better ductility than ferrite. In contrast, the ferrite is usually believed to be stronger than austenite.

1.3.3 Compositional difference between austenite and ferrite

The alloying elements are of great importance in the steel especially in the duplex stainless steel because it can affect the formation of both phases. Some alloy elements tend to form austenite and thus termed as austenite former while other elements are more likely to form ferrite and are regarded as ferrite former. Nickel, nitrogen, carbon, manganese and copper are generally believed to be the austenite former while the chromium, silicon and molybdenum are ferrite former. The compositional difference between two phases can also result in the difference of the property. For example, the reason that austenite is more susceptible to stress crossion cracking is attributed to the higher concentration of nickel.

Generally speaking, the duplex structure has improved stress corrosion cracking resistance, compared with austenitic stainless steels and improved toughness and ductility, compared with the ferritic stainless steels [2].

1.4 Aging effect of CASS used in LWRs

1.4.1 Thermal aging effect on CASS

It has been well known that the CASS is susceptible to thermal aging embrittlement. As has been reported by several researchers, thermal aging will induce a variety of new phases, which then induce the embrittlement. A schematic of the time-temperature transformation plot is shown below in Figure 1-3, along with the potential influence of alloying elements on these curve shifts [3]. It can be clearly seen that as thermal aging temperature increases, more phases will precipitate. Here for the nuclear reactor case, as temperature range is around 280-320 ℃, the embrittlement is attributed to phase transformations in ferrite include spinodal decomposition and Ni-Si-Mn rich G-phase precipitates.

Thermal aging will induce the spinodal decomposition of the ferrite phase into chromium-rich α’ phase and iron-rich α phase. The reason for the spinodal decomposition is due to the presentation of the miscibility gap in Fe-Cr system. As shown in Figure 1-4, the region between M and N point is defined as spinodal region. Inside the spinodal region, for example, the original composition is given by X_c, then the free energy is given by the point P. Due to the fluctuation, the previous uniform solution decomposes into a mixture of two solutions represented by point A and B, respectively. The free energy of this nonuniform mixture lies along the line AB and given by the point Q. As the free energy curve is concave down, the free enery at point Q is always lower than at point P even for an infinitesimal fluctuation. Therefore, this process is thermodynamically spontaneous, this process will continue, and the points A, B will gradually become points M, N. As the concentration departs the spinodal region, further spinodal decomposition will increase the free energy as the curve switch from concave down to concave up, thus, the decomposition is no longer spontaneous. The further

phase decomposition progress through nuclearation and growth. Ultimately, the starting single uniform phase will decompose into a stable two-phase mixture with composition given by the common tangent construction shown in Figure 1-4.

Besides spinodal decomposition, G-phase precipitation is another microstructural evolution that is commonly seen for CASSs after thermal aging. The G-phase is a ternary intermetallic compound with stoichiometric composition of $M_6Ni_{16}Si_7$, M= Mn, Cr. It has a face centered cubic (fcc) structure with lattice parameter exactly four times that of body centered cubic (bcc) ferrite. After thermal aging, G-phase always forms at the α/α' interface accompanied with spinodal decomposition. In contrast to the final composition of G-phase can be easily confirmed by TEM and APT [4], the precipitate mechanism of G-phase during thermal aging cannot be easily clarified. The earlier researchers, A. MATEO claimed that the the G-phase formation may consists of two steps. The first one is described by the mechanism illustrated in Fig 1-5: spinodal decomposition leads to an Fe-rich α and Cr-rich α' phase, While the α domain rejects Si and Mo atoms, the α' domain rejects Ni and Mn atoms. Therefore, spinodal decomposition leads to an interdomain region that is rich in Si, Mn, Ni and Mo and serves as a precursory site for the development of the G-phase. For the second step, it involves the attainment of the critical chemical composition close to G-phase for the α/α' interdomain region. Then the intermetallic compound will precipitate through nucleation and growth [5]. Later, Y. Matsukawa performed a full investigation on thermally aged ferrite/austenite duplex stainless steel using APT, TEM and simulation of electron diffraction patterns. A different two-step nucleation process was proposed: first spontaneous growth of Ni-Si-Mn solute clusters, then structural change transforming into the G-phase. Besides, structural change was found through another two-step process: the growth of clusters to become a critical size first, followed by solute enrichment within the clusters to become a critical composition [4]. Recently, Timothy conducted Pearson correlation analysis on G-phase elements on thermally aged CASSs and found the Ni segregation happened before Si and Mn. In equilibrium, Si and Mn has a miscibility in Ni that is greater than in Cr [6-8], therefore, it is attributed that the thermodynamic driving force is the reason that cause these elements segregate as Ni precipitates out of the Fe and Cr [9].

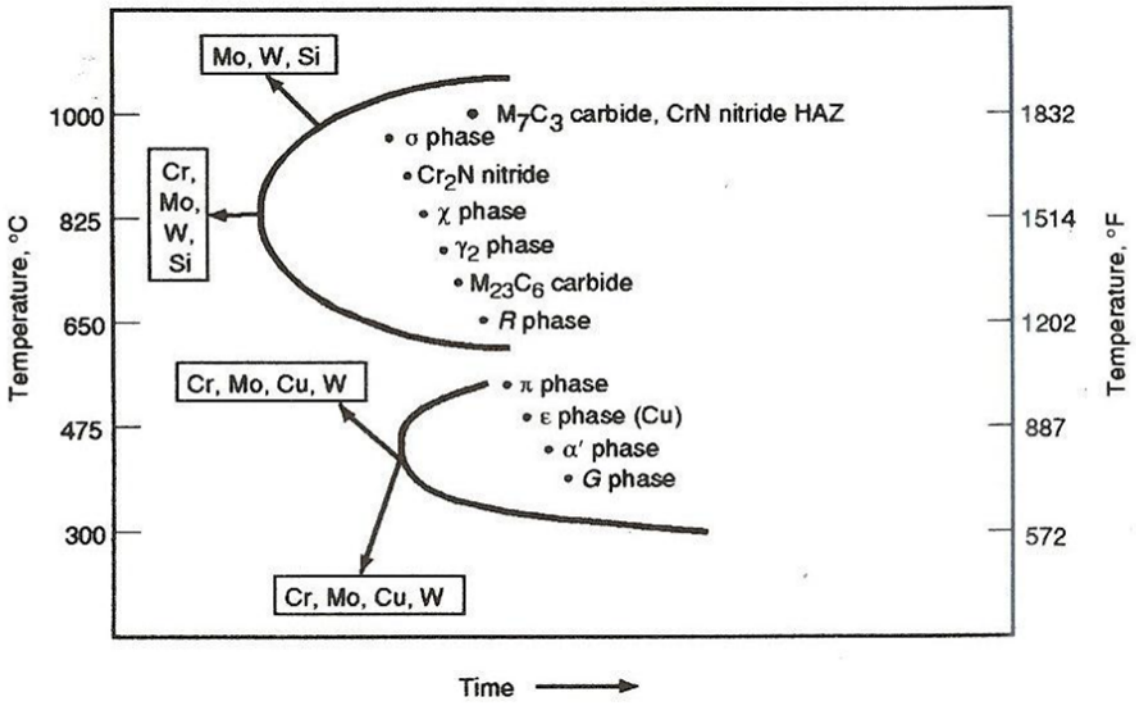

Figure 1-3. Time - temperature transformation diagram for CASS, showing the influence of alloying elements on precipitation reactions in duplex stainless steels. (Source: Ref.[3].

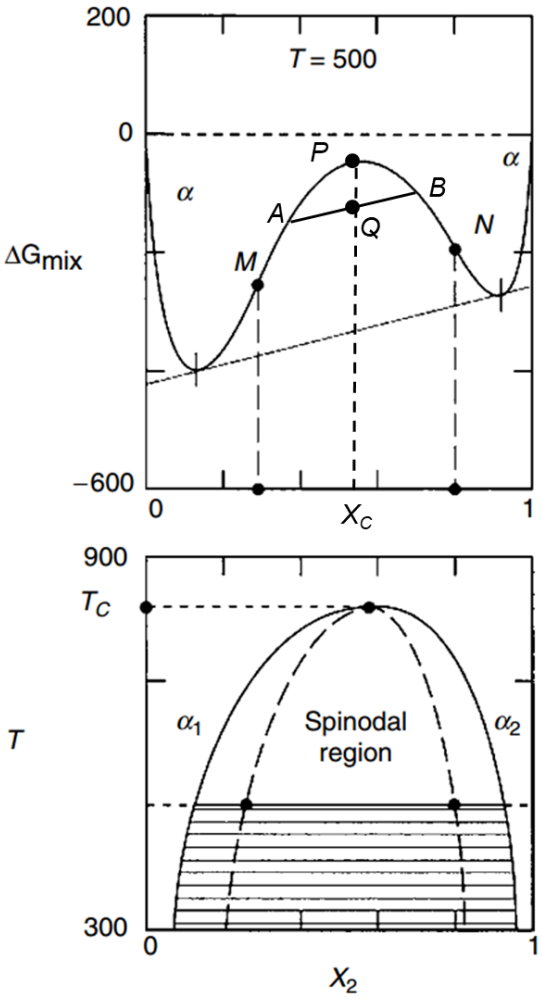

Figure 1-4. The thermodynamic basis for the spinodal region inside a miscibility gap. (Source: Ref. [10])

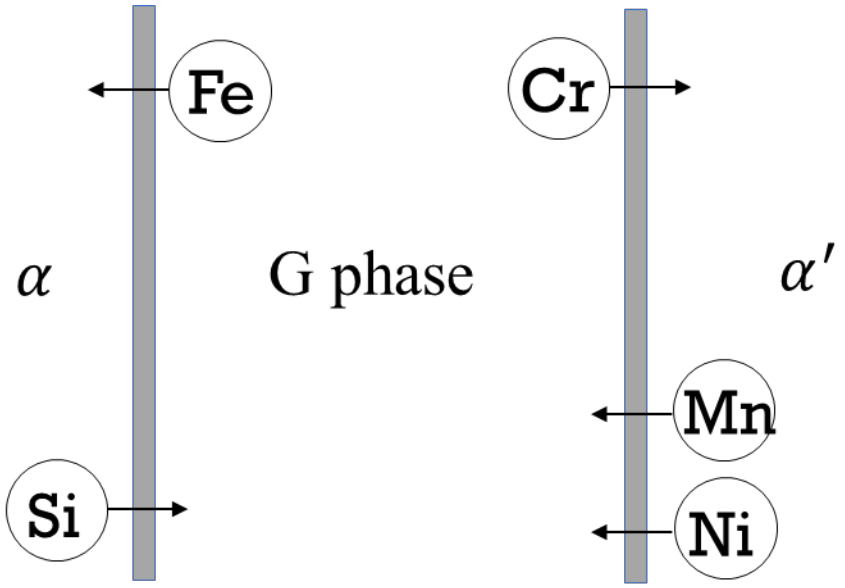

Figure 1-5. Fluxes of the elements during the G-phase formation and the spinodal decomposition of the ferrite. (Source: Ref. [5])

1.4.2 Accelating aging mechanism

In reality, the operating temperature of CASSs in LWRs is around 280-320 ℃. To extend the lifetime of LWRs beyond 60 years, it is ideally to have the materials that are actually aged at the same temperature as operating condition for 60 years. Unfortunately, it is not practical to pursue a real-time aging experiment for 60 years or beyond in a reactor environment. Therefore, an accelating aging at higher temperature is necessary to make the experiment more achievable. As mentioned in last section, thermal aging at different temperature may introduce different microstructural evolution, thus, attention is needed to carefully select the accelerating temperature. It should be high enough to reduce the aging time substantially and meanwhile the aging mechanism must not differ from those found at CASS service temperature. Besides, thermal embrittlement depends on many material and heating parameters such as chemistry of the material, processing conditions, and aging temperature [11]. Previous publications have used several methods to acquire a reasonable temperature to simulate the aging situation under reactor environment and a custome of using 400 ℃ as the accelerate aging temperature is formed. However, as reviewed by T.S. BYUN [12], the activation energy is not constant over the temperature range of 290-450 ℃. A small variation of temperature may induce a huge difference in the prediction of the embrittlement of CASSs. Though currently 400 ℃is widely accepted, more detailed research is still needed to confirm the fundamental mechanisms of microstructural evolution and associated activation energy over the temperature range between service temperatures and accelerated aging temperatures.

To calculate the aging time t(T) in an accelerated aging experiment at an elevated temperature T, the Arrhenius-type equation is used:

$$t(T) = t_0[e^{\frac{Q}{RT}}/e^{\frac{Q}{RT_0}}]$$

where t_0 and T_0 are the time and temperature for service lifetime, respectively, and Q is the activation energy (in kJ/mol) and R is the gas constant (8.314 J/mol K).

1.4.3 Neutron irradiation effect on CASS

Currently, the structural materials in (2nd-generation) commercial light water reactors are subjected to moderate temperatures (~290-330°C) and relatively low doses (<0.1 dpa, for the reactor pressure vessel steel and 10 to 30 dpa for core internal structures) [13]. Though CASSs components are applied as structural material and only has very limited irradiaton exposure, the evaluation of irradiation-induced degradation is still necessary.

Irradiation has several effects on CASS. It can induce defect formation and aggregation as well as phase transformation thus leading to the mechanical property degradation. For CASSs with duplex structure, the irradiation response is different for different phases. For austenite phase, it has been reviewed that the microstructural evolution for austenitic stainless steels due to neutron irradiation varies with the irradiation temperature, irradiation dose and dose rate. Irradiation at the 'low-temperature' regime usually generates small 'black-spot' defect clusters and faulted dislocation loops while bubble, voids, dislocation loops, network dislocations and precipitations forms at the 'high-temperature' regime [14-17]. For ferrite phase, the microstructural evolution due to neutron irradiation follows a similar trend to austenite, nevertherless, as ferrite phase is generally stronger than the austenite phase, the size or number density of defects within ferrite phase is usually much smaller and lower [18].

1.5 Motivation and Objective, Complementary Research Methods, Significances

1.5.1 Motivation and Objective

The majority of the current nuclear reactor in service in United States are generation II reactors, which are built in 1960s, with original designed lifetime to be 40 years. Even though a 20-year extension of licenses is granted on a case-by-case basis, these nuclear reactors are going to reach the end of their 60-year operating licenses soon. In the meantime, the domestic electricity demand is still growing at around 1% annually. If those old reactors are no longer in use, a huge electricity shortage can be anticipated in the future. Certainly, building a new fleet of reactors is another option, however, considering an estimated 5 to 6-year construction and startup testing schedule for nuclear reactors providing 1.1–1.7 GWe (electric), even 4 reactors are assumed to be built every year starts at 2021, it will not be possible to have continued growth of generating capacity beyond 2029 as the current commercial reactors retires once reaching their 60-year limit. Therefore, extending the lifetime of current nuclear power plants to 80 or even 100 years is the optimal solution. Besides, it has been estimated that it would cost around 500 biliion to replace the current fleet of reactors [16]. Although it is finicially possible to replace the old nuclear power plants with traditional fossil plants, hugh amount of greenhouse gas emission from fossil fuel combustion will cause

serious environmental problem. Overall, extending the lifetime of current nuclear power plants to another 20-years is the best solution to satisfy the great electricity demand for the country not only economically, but also environmental-friendly.

When 47 US nuclear utility executives were polled about reactor lifetimes beyond 60 years, two-thirds cited plant reliability as the key issue with materials aging and cable/piping as the top concerns for plant reliability [19]. Therefore, developing a scientific basis for better understanding and more accurately predicting the long-term environmental degradation behavior of the primary system, structure and components in current LWRs is necessary. Although great effort has been input in this area, those studies performed were focused on either the characterization of microstructural evolution or mechanical property degradation. The knowledge gap still exists about the correlation between microstructure and mechanical property is still the major limitation that inhibits us to accurate evaluate and predict the performance of materials under anticipated operation conditions.

1.5.2 Complementary Research Methods

CASSs consists of duplex structure: ferrite phase within austenite matrix. Both phases are having different microstructural evolution during thermal aging and neutron irradiation. The difference makes it more difficult to correlate the mechanical properties with microstructural of CASSs, therefore, complementary techniques are needed to fully reveal the correlation.

In this research, two types of techniques are included. The first type is utilizing the high energy synchrotron X-ray. Synchrotron sourve has two advantages, and the first one is the capability to provide X-ray with high resolution and low inelastic background. It makes it possible to incorporate tensile test with wide angle X-ray diffraction and the new technique is called in-situ Wide Angle X-ray (WAXS) tensile test. The tensile test is able to record the mechanical information while the WAXS can resolve the peaks from both phases, thus making it a perfect tool for investigation of the mechanical response of different phases within an alloy [20-25]. For our case, the ferrite and austenite can be easily resolved by synchrotron X-ray, thus their mechanical property can be probed. Nevertheless, the X-ray diffraction still has deficiency due to its fundamental mechasim and resolution, it cannot probe the spinodal decomposition and G-phase precipitation within ferrite. Spinodal decomposition makes ferrite decomposes into Fe-rich α and Cr-rich α’ phase. Both of them are BCC structure with very close lattice parameter, thus, XRD cannot dissolve them. Besides, the nano-sized G-phase precipitation has a very low volumetric fraction less than 1%, which is beyond the lower limit of X-ray diffraction, therefore, a second high energy X-ray technique is needed. The second X-ray related technique is Extended X-ray Absorption Fine structure Spectroscopy (EXAFS), which has been used to probe microstructural changes of local atomic environments in several classes of alloys [26-28]. Thanks to the benefit of synchrotron X-ray, a variety of beam enery can be easily selected during the experiment. Therefore, beam energy can be set close to the absorption edge of different elements and probe various elements within the specimen. When the characteristic X-ray is absorbed by central atom, the rest of X-ray can be regard as spherical waves propagating outward from the absorber atoms. The outgoing photoelectron waves will

be scattered by the atoms surrounding the absorber. The scattered waves will interfere with the original outgoing waves, resulting an oscillation in the absorption spectrum. The EXAFS oscillations of the X-ray absorption spectrum begin approximately 40 eV above the absorption edge and continue to higher photon energy. The measurements of the oscillations can reveal the local atomic environment of the absorbing atom, providing local structural parameters such as atom types, coordination number and atomic distance of neighboring atoms. Comparing with WAXS, EXAFS has a much higher resolution. However, the data analysis for EXAFS is very complicated, especially for materials having several different structures. As EXAFS can dissolve each structure, the final absorption spectrum is the average result of all the potential structures. For our case, the CASSs has two phases at the beginning. With thermal aging or neutron irradiation induced spinodal decomposition and G-phase precipitation, a third structure is introduced, making the data analysis rather challenging. Therefore, great effort is needed while analyzing the EXAFS data.

Besides the advantages mention previously, synchrotron X-ray techniques have another benefit over ordinary microstructural characterization technique, which is the capability to probe a large amount of volume, therefore, the results are statistically more convincing. However, the information from X-ray relies heavily on the data analysis, to accurately interpret the X-ray results, it is always necessary to incorporate the microstructural characterization e.g. Transmission Electron Microscopy (TEM) and Atop Probe Tomography (APT).

Other than in-situ WAXS tensile test, the mechanical property for both ferrite and austenite phases are also investigated using nanoindentation. Nanoindentation as characterization of neutron irradiated materials using the X-ray techniques is very challenging. Not only because it is hard to acquire tensile specimens for neutron irradiated materials but also is that the public user facility such as the Advanced Photon Source (APS) has a very strict safety rule for handling the radioactive materials.

Finally, Finite Element Method (FEM) modelling is also included in this project. The modelling work is focused on the stress/strain distribution between ferrite and austenite during tensiletest. Besides, it is also applied to validate the in-situ WAXS tensile test analysis. As X-ray diffraction can disseminate ferrite and austenite phase, their individual stress and strain curve can be calculated with WAXS data analysis. These data can work as input parameters for FEM to calculate the true stress-true strain curve for bulk tensile curve. Hence, the calculated bulk tensile test curve can be compared with the experimental results, and the in-situ WAXS tensile test analysis can be validated.

1.5.3 Significance

It is important to extend the lifetime of current LWRs as it is the most economic, environmental-friendly and practical way to satisfy the electricity demand of US. To extend the lifetime of LWRs, the most important issue to ensure the structural used in reactors can perform properly. While the microstructural characterization has been conducted extensively, the current largest knowledge gap is to build the correlation between microstructural and mechanical property.

In this project, a bunch of different experimental techniques are utlized including synchrotron X-ray (the in-situ WAXS tensile test, EXAFS) and microstructural characterization (APT, TEM) to find the correlation between microstructural and mechanical property. The combination of in-situ WAXS tensile test and post-tensile TEM characterization can yield a thorough understanding of the microstructure and the mechanical behavior of the thermally aged CASSs. The TEM, APT and nanoindentation can reveal the correlation between mechanical property and microstructural evolution of neutron irradiated CASSs. Besides, to help predict the mechanical property of structural material, FEM is also included. The material property acquired from the in-situ WAXS tensile test is used as input parameters to simulate the stress-strain curve for thermally aged CASSs. The experimental and simulation result in this project is able to help evaluate mechanical performance of materials served in nuclear reactors for long a long time, therefore, providing scientific basis to extend their lifetime.

EXPERIMENTAL DETAILS

2.1 In-situ Wide Angle X-ray (WAXS) Tensile Test

2.1.1 Experimental Setup and material selection

The in-situ WAXS tensile test were carried out at the 10-ID-B beamline at the Advanced Photon Source (APS), Argonne National Laboratory (ANL). The experiment setup as well as the specimen geometry for both in-situ WAXS tensile test are the same and are shown in Figure 2-1. The dimensions of the miniature tensile specimens were 1.12mm × 0.48 mm × 5.00 mm (width × thickness × gauge length). Figure 2-2 shows a 2D raw diffraction pattern, which is a serious of concentric rings. To analysis the mechanical response of the material, the DP at two different azimuths are of great importance, which are the transverse and longitudinal direction corresponding to $\eta = 0^{\circ}$ and 90°, respectively. The 1D profile is then integrated from ±15 azimuth at transverse and longitudinal direction to acquire the d-spacing, peak intensity. Finally, lattice stain ε_l in this direction is calculated using:

$$\varepsilon_l = \frac{d - d_0}{d_0} \tag{2-1}$$

where d_0 is the specific d-spacing prior to deformation and d is the instantaneous d-spacing during deformation.

As can be seen from the data analysis process, it relies heavily on the integration of diffraction rings. For some case, for example single crystals, their DP are discrete points. The diffraction points distribution is random, they may or may not fall into the region at ±15 azimuth at transverse and longitudinal direction, therefore, it is unlikely to acquire any useful information with this technique for single crystals.

Although CASSs are not single-crystal material, their grain size is huge (around 500 um). Considering the X-ray beam size is usually around 500 μm × 500 μm, CASSs are performing just as single crystal under the X-ray diffraction, therefore, using CASSs directly for in-situ WAXS tensile test is not ideal. To circumvent this dilemma, special treatment is needed for CASSs before conducting the in-situ WAXS tensile test. The as-cast steel ingot was cold rolled to a total reduction of around 70%, and subsequently annealed at 1100 °C for 5 min, followed by water quenching. The wrought and anneal process significantly reduce the grain size and the final average grain sizes of austenite and ferrite are about 60 and 20 μm, respectively.

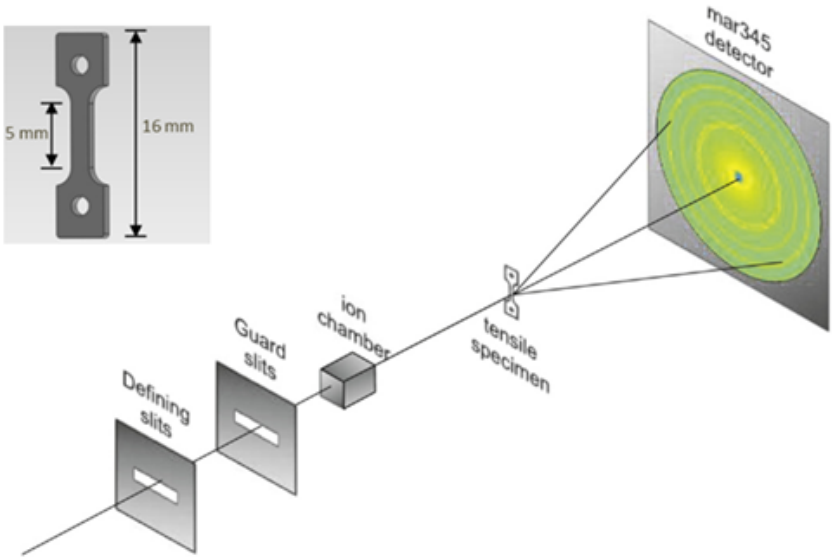

Figure 2-1. In-situ WAXS tensile test experiment setup and specimen geometry.

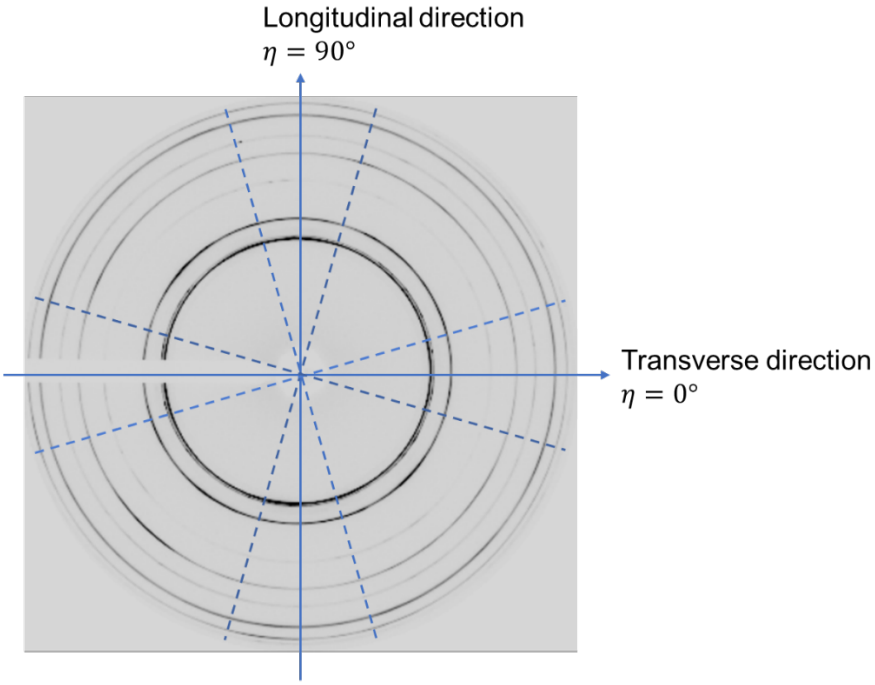

Figure 2-2. Schematic figure showing the azimuthal angle selection for peak fittings to calculate the longitudinal and transverse lattice strains.

The chemical composition for the as-cast steel ingot is listed in Table 2-1 and the volume fraction of ferrite is appropriate 10%. Due to the capability of penetration of synchrotron X-ray, the standard tensile specimen is not applicable here, thus, electrical discharge machined miniature tensile specimens were used for the experiment. Some of the miniature tensile specimens were thermally aged under 475°C for 400, 1000 and 3000 hours, while others were not thermally aged and kept as comparison.

Table 2-1. Chemical composition (wt%) of the CASSs.

Ni	Si	P	S	Mn	C	N	Cr	Mn	Fe
10.2	1.15	0.026	0.0032	1.02	0.031	0.091	20.45	0.2	Bal.

2.1.2 Experiment Details

Two separate in-situ WAXS tensile test with same specimen geometry and similar experiment setup were carried out at the 10-ID-B beamline at the Advanced Photon Source (APS), Argonne National Laboratory (ANL). Both in situ WAXS experiment setup and the tensile specimen geometry are the same and are shown in Figure 2-1. Due to the different research purpose and the facility issue, two experiments have a little difference in the experiment setup.

In the first experiment, monochromatic X-ray beam with energy about 64 keV (λ = 0.1925 Å) with beam size about 600 μm × 600 μm was used. The tensile specimen was mounted on a Deben 5 kN dual leadscrew tensile stage. The specimen was strained incrementally until fracture. Uniaxial tensile tests were performed in the displacement control mode, with a displacement step of 0.001 mm in the elastic region and 0.05–0.10 mm in the plastic region. Position was kept constant after each displacement to acquire the X-ray diffraction pattern. During the tensile test, the mar345 image plate X-ray detector was used to acquire X-ray diffraction patterns. To maximize the signal-to-noise ratio without saturation the X-ray exposure time was set to be 30 seconds for each pattern.

According to ToMOTA et al [29, 30], the stress-strain curve of CASSs can be divided into four stages: (1) both ferrite and austenite are elastic (2) only the soft austenite phase deforms plastically while the hard ferrite phase remains elastic. (3) both ferrite and austenite phase deform plastically (4) stage leads to the fracture accompanying the decohesion at the interface or the fracture of the hard ferrite phase. After the first experiment, it is found that too few data points were recorded in the linear region (before austenite yields), which makes it hard to determine the yield strength of austenite phase. Therefore, for the second experiment, uniaxial tensile tests were performed in the constant load mode, with a load step around 10N in the elastic region and 20-50N in the plastic region. Diffraction pattern was acquired the same way as the first experiment except that in the linear region, less exposure time was applied to avoid over saturation. The monochromatic X-ray beam with energy about 52 keV (λ = 0.2394 Å) with beam size about 400 μm × 400 μm was used for the second experiment.

2.2 Atom probe tomography characterization of neutron irradiated CASSs

2.2.1 Irradiated Material Preparation

The chemical composition of cast stainless steel CF-3 used in this study is listed in Table 2-2. The volumetric fraction of ferrite is 24%. The neutron irradiated specimens are in the form of 3-mm discs (~120 um in thickness). The discs prepared for irradiation were electropolished to reveal the ferrite and austenite phase boundary. Two sets of

specimens were prepared, the first set is to investigate the effect between thermal aging and neutron irradiation to 3 dpa. For this set of specimens, some 3-mm discs were aged at 400°C for 10,000 hours prior to irradiation. The neutron irradiation on the unaged and aged samples was conducted in the Halden reactor at around 307°C to a dose of 3 dpa with a dose rate of 5×10^{-8}dpa/s. The second set of specimens are aimed to investigate the neutron irradiation effect at extremely high dose to fully understand the neutron irradiation effect on ferrite phase. For this set of specimens, 3-mm discs were irradiated in the Bor-60 reactor to 5, 10, 20, and 40 dpa at temperature around 320°C with a dose rate of 7×10^{-7}dpa/s. The detailed neutron irradiation condition is listed in Table 2-3.

Table 2-2. Chemical composition (wt%) of the neutron irradiated CF-3 CASS.

Ni	Si	P	S	Mn	C	N	Cr	Mo	Fe
8.59	1.13	0.015	0.005	0.63	0.023	0.028	20.18	0.34	Bal.

Table 1-3. Detailed neutron irradiation condition.

Dose	Reactor	irr. temperature	Irradiation environment	Estimated dose rate
3 dpa	Halden	303-311℃, avg. 307℃	Helium	5×10^{-8} dpa/s
5 dpa	BOR60	315-325℃	Sodium	7×10^{-7} dpa/s
10 dpa	BOR60	315-325℃	Sodium	7×10^{-7} dpa/s
20 dpa	BOR60	315-325℃	Sodium	7×10^{-7} dpa/s
40 dpa	BOR60	315-325℃	Sodium	7×10^{-7} dpa/s

2.2.2 Atom Probe Characterization

The APT probe specimens were fabricated using a focused ion beam (FEI 3D Quanta FEG FIB), and the samples were finished using ion beam imaging for 2 min at beam energy of 2 kV and current of 27 pA to ensure a minimal Ga implantation and radiation damage from ion beam. For each condition, a minimum of 6 tips were fabricated, however, due to the limitation of instrumental time, not all the tips were investigated in APT. For 3 dpa w./wo. thermal aging, 6 tips were analyzed while for the 5, 10, 20 and 40 dpa condition only 1 tip, 2 tips, 3 tips and 3 tips were analyzed, respectively.

The atom probe experiment was carried out in a local field atom probe (LEAP) 4000 XHR at 55 K with ion detection efficiency at 37%. For 3 dpa condition, the voltage mode is applied with a pulse fraction of 20%, detection rate of 0.005 atoms/pulse and pulse repetition rate of 200 kHz. For specimens irradiated to 5, 10, 20 and 40 dpa, the laser mode is applied with laser pulse rate set at 200 kHz and pulse energy at 60 pJ. The detection rate was kept between 0.1% - 0.5% to allow for large dataset collection. Reconstructions and analyses were performed using Cameca's Integrated Visualization and Analysis Software 3.8.0 (IVAS). The 3-D reconstructions were conducted by following the standard procedure of the Recon Wizard in the software, and SEM tip images were used for defining tip profiles. The evaporation field value was 33.0 V/nm and k factor of 3.30 was used.

2.3 TEM Characterization

Transmission Electron Microscopy (TEM) characterization is always a good complementary technique to better interpret the X-ray and APT result. In this project, all the TEM lemallas were prepared with FIB. All the FIB and TEM work were performed withFEI HELIOS 600i and FEI Tecnai F30 S/TEM in the Microscopy and Characterization Suite (MaCS) of the Center for Advanced Energy Studies (CAES) at Idaho Falls, ID.

2.3.1 Post-tensile TEM characterization

In order to validate the WAXS result, TEM was used to measure the dislocation density for both unaged and aged conditions. To prepare the TEM specimens, post-tensile specimen was glued onto a steel plate holder with wax, and further polishing was carried on a Struers Tegramin-25 to flatten both surfaces and remove the EDM sectioning damage layer. The rotation speed of the wheel was set at 150 rpm. The sample surface was finished with 800 grit SiC sandpaper. Later, to eliminate the grinding damage layer, further polishing with a 3 μm diamond suspension was used. Finally, the specimen was polished with 0.06 μm silica suspension. This step not only can further remove the damage layer but also as silica suspension has some corrosivity, it can reveal the ferrite-austenite boundaries.

The polished post-tensile specimens were transferred to FIB, and TEM lamellas were lifted out at the ferrite-austenite phase boundary from the gauge part of the miniature specimens.

2.3.2 TEM Diffraction Pattern of Neutron Irradiated Ferrite Phase

TEM diffraction was performed on the same neutron irradiated specimens as APT characterization. The main purpose of TEM diffraction pattern here is to determine whether the Mn-Si-Ni cluster has formed the G-phase crystallographic structure. The FIB was used to prepare TEM lamellas for 5, 10 and 20 dpa conditions. All the lamellas were finished using low energy ion beam cleaning with voltage of 2kV and current of 27pA to ensure a minimal Ga implantation as same as APT tip preparation. For TEM characterization, all the diffraction patterns were taken at the 110 zone axis of the ferrite phase.

2.4 EXAFS characterization of thermally aged CASSs

2.4.1 Sample Preparation

The material is 308L weld and CF-3 cast stainless steel. Their composition is listed below in Table 2-4. A total of 8 samples were prepared. For weld, the samples were thermally aged at 400°C for 3000, 6000 and 10,000 hours while an unaged sample was included as comparison. For the cast stainless steel, 4 samples were prepared. While two of them have about 10 percent ferrite, the other two have about 25 percent ferrite. For CASSs with different ferrite fraction, one was thermally aged at

400°C for 10,000 hours, while the other one was unaged counterparts. The detailed sample information is listed in Table 2-5.

Table 2-4. Composition of 308L weld and CF-3.

Materials	Composition (wt%)								
	Mn	Si	P	S	Mo	Cr	Ni	N	C
308L weld	1.80	0.55	0.023	0.008	0.31	18.62	8.95	0.067	0.015
CF-3, ~10%	0.57	0.92	0.012	0.005	0.35	19.49	9.4	0.052	0.009
CF-3, ~25%	0.63	1.13	0.015	0.005	0.34	20.18	8.59	0.028	0.023

Table 2-5. Information about the samples.

Sample ID	Materials	Ferrite %	Aging Temp (°C)	Aging time (h)	Thickness (micron)
W-1-U	308L weld	~7%	-	-	215
W-1-3k	308L weld	~7%	400	2226	222
W-1-6k	308L weld	~7%	400	6,000	272
W-1-10k	308L weld	~7%	400	10,000	189
CF-3_1-U	CF-3, Cast	~10%	-	-	215
CF-3_1-A	CF-3, Cast	~10%	400	10,000	207
CF-3_2-U	CF-3, Cast	~25%	-	-	228
CF-3_2-A	CF-3, Cast	~25%	400	10,000	269

Then EXAFS experiment was performed at Materials Research Collaborative Access Team (MRCAT) beamline 10-ID, Advance Photon Source (APS) in Argonne National Lab. As the sample is too thick for X-ray to penetrate, the absorption spectra of the CF-3 CASS and 308L welds were recorded at the Fe, Cr, Ni, Mn and Mo K-edges in the fluorescence geometry at room temperature. To get a statistic result, multiple scanning was performed for each different element. For example, the Fe, Cr, Ni has a relatively large concentration within the material, thus, the data quality is satisfying and only 10 scanning was performed. However, for Mn and Mo, due to their low concentration, it is necessary to perform 25 or even 36 scanning to get a better statistic result.

2.5 Nanoindentation Experiment

Nanoindentation was conducted at CAES/INL by the project ANL collaborator. Due to the size limit of both the thermal aged and irradiated specimen (3mm disks) in this program, it's not feasible to perform mechanical tests such as tensile test or fracture toughness test on them. Nano indentation has the advantage of using nano size indent

on the area of interest to enable deformation within a few microns and thus obtaining mechanical properties of hardness and young's module.

To ensure that the indent tip can scan the sample surface successfully while differentiating austenite and ferrite, the sample was prepared using an electro-polishing method with a 3 mm jet nozzle for 5 second at -20°C. Electrolyte was a mixture of10% perchloric acid balanced with methanol. Hysitron triboindenter 900 was used for this nano-hardness test, and the indenter used here is a cube tip. All indentations were performed after proper. To avoid interference between austenite and ferrite phase, the load of 600 μN was used for the indentation and the indentation depth was about 150 nm.

2.6 Finite Element Method Modelling

2.6.1 Acquistion of 2D Microstructure

The 2D modelling starts with acquiring the microstructure of the duplex stainless steels. The CF-3 cast duplex stainless steel was grinded using the 600 and 800 grit sandpaper to flat both surfaces, later, one surface was further polished using the 3 μm polycrystalline diamond suspension with lubricant. The final step was using the 0.06 μm colloidal silica suspension to remove all the scratch and to etch the surface. After all the grinding and polishing, the specimen was rinsed with the micro organic soap solution and then sonicated in acetone and methanol to remove the silica particles and any potential contamination. The optical image of duplex stainless steel is acquired from the Nikon Eclipse LV100 optical microscope.

The optical image (Figure 2-3 (a))was first transferred into the binary pixelated images (Figure 2-3 (b)) using public domain ImageJ software (available through NIH) [31]. Then the binary image was vectorized using the RasterVect® v.26.5 software. Vectorized image was imported into commercial software (AutoCAD® 2019), and visually adjusted computational artifacts as shown in Figure 2-3 (c). Finally, the output file was imported to Abaqus® 6.14 through sketch function, a spline plot was applied here to further eliminate the unreal sharp angle that result from the image vectorization (as shown in Figure 2-3 (d)).

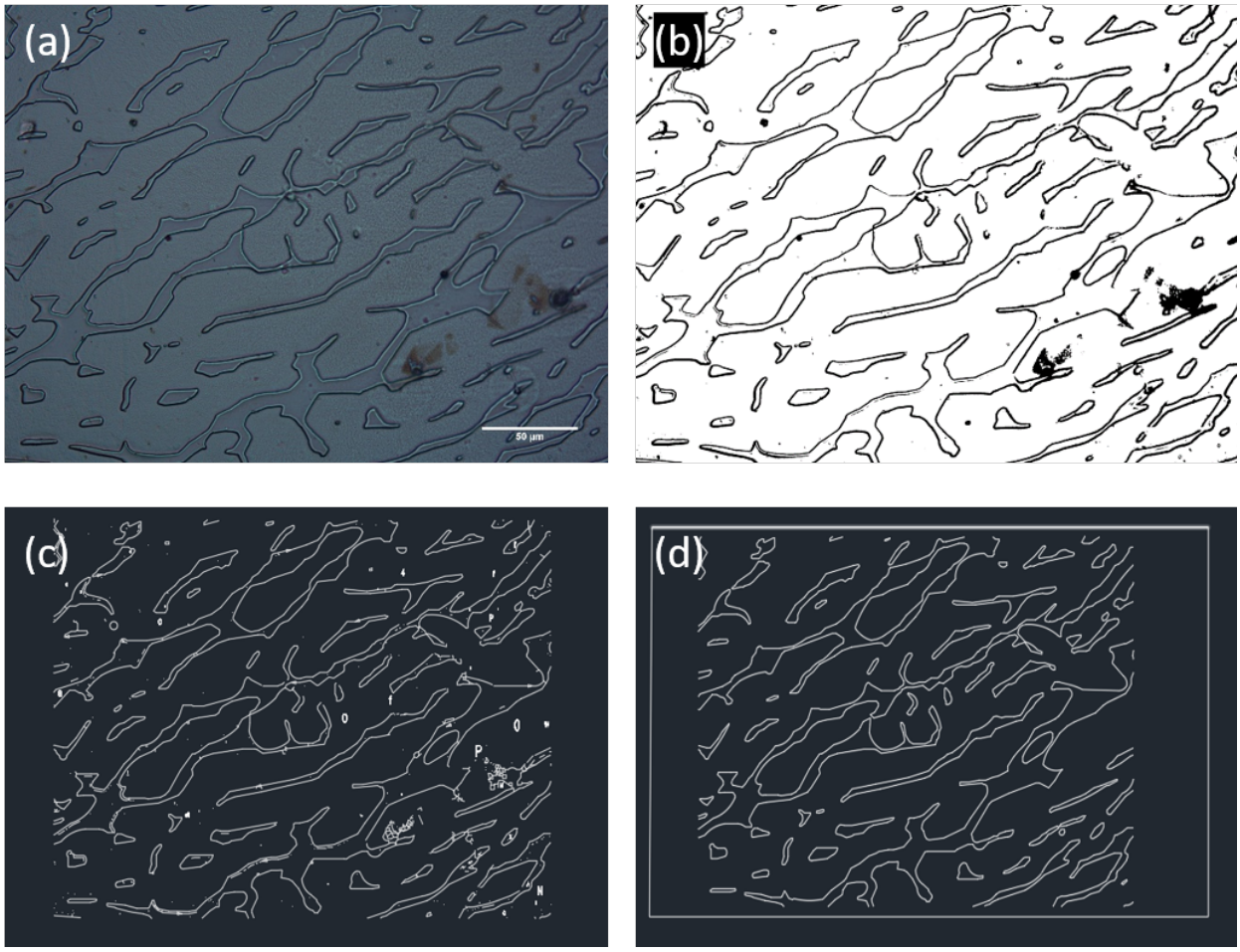

Figure 2-3. (a) Optical image of CF-3 duplex stainless steel. (b) The binary image acquired using ImageJ. (c) Vectorized image in AutoCAD. (d) Vectorized image after modification in AutoCAD.

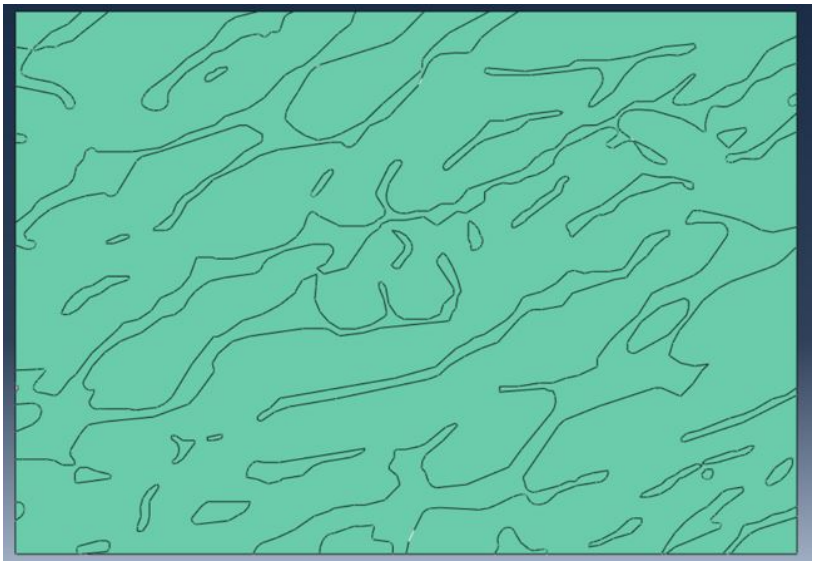
Figure 2-4. The final appearence in Abaqus.

2.6.2 Validation of In-situ WAXS Tensile Test Through True Stress-True Strain Curve Modelling

Modelling of the true stress-true strain curve of thermally aged duplex stainless steel was conducted using the same strategy from a reference paper [32]. First, a 2D dogbone was created in Abaqus® 6.14. The tensile specimen has a total length of 16 mm and its gauge area (1.2 mm × 5 mm) which is the same geometry as our experimental specimen, was finely meshed with elements having an edge length of 200 × 200 μm (as shown in Figure 2-5). The material property needed for the simulation contains three parts: general property: e.g. density, the elastic property: e.g. elastic modulus, the plastic property: e.g. yield strength and plastic stress-plastic strain data. All these properties were acquired from either reference paper or our in-situ wide angle X-ray (WAXS) tensile test performed at Argonne National Lab. The capability of synchrotron X-ray allows us to understand the mechanical response of both ferrite and austenite phase individually. The details about the WAXS experiment setup, acquisition of necessary input data for modelling is discussed in section 2-1 and section 3-6, and this section is focused on introduction of the simulation work in Abaqus® 6.14.

During the simulation, the left side of the dogbone was set to be encastre while the right side was set to be 0.005, 0.01, 0.05, 0.1, 0.5, 0.75, 1, 1.25, 1.5 and 2 mm, which correspons to 0.1%, 0.2%, 1%, 5%, 10%, 15%, 20%, 25%, 30% and 40% strain. The displacements of an element in the middle of the gauge length were transferred to the corner nodes of the mesoscale model and linearly interpolated for all nodes located between the corner nodes. For the 200 × 200 μm mesoscale model, another separate simulation was conducted. The displacement for each edge was input to the simulation and the reaction force for each node at the right edge was recorded and summed to acquire the total reaction force. The reaction force was then used to calculate the stress. Thus, the real true stress–true strain curve of duplex microstructure resulting from macroscopic loads can be studied. The simulation result comparing with the experimental result for unaged, aged 1000 hours and aged 3000 hours are listed in section 3-6.

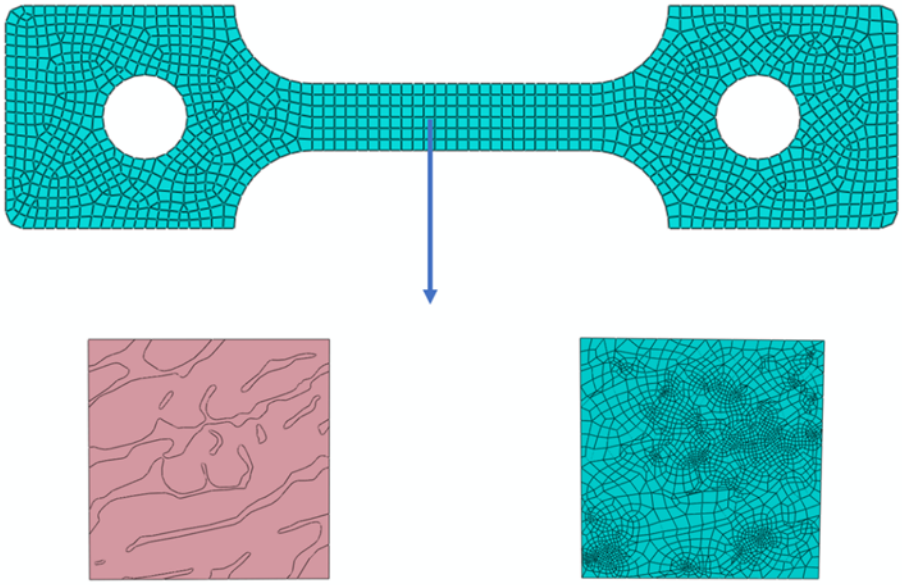

Figure 2-5. 2D model of the dogbone, finely meshed in order to transfer the displacements to the mesoscale model.

2.6.2 2D Simulation of Stress/Strain Distribution

As the material properties acquired from in-situ WAXS tensile test has been validated, a 2D modelling work is performed to reveal the stress/strain distribution within CASSs w./wo. thermal aging during tensile test. The 2D structure based on the real unaged ferritic-austenitic cast duplex stainless steel with geometry of 0.2322 mm × 0.3186 mm was acquired using optical micrographs as described previously. The left edge was set to be encastre while on the right side, applied displacements were set equivalent to 0.1%, 1%, 2%, 5% and 10% strain using the boundary condition function. The von Mises stress distribution and in-plane principal strain distribution for both ferrite and austenite phase for unaged, aged 1000 hours and aged 3000 hours with 0.1%, 1%, 2%, 5% and 10% strain are shown in section 3-6.

RESULT

3.1 In-situ WAXS Tensile Test Result

3.1.1 Macroscopic tensile properties during aging

The macroscopic tensile data for the first and second WAXS experiments are shown in Figure 3-1 and Figure 3-2, respectively. The engineering stress–strain curves for both the as-received and aged specimens are shown in Figure 3-1 (a) and Fig 3-2 (a). The true stress and the true strain are calculated from the engineering stress and engineering strain using $\sigma_t = \sigma_e\ (1 + \varepsilon_t\ )$ and $\varepsilon_t = ln(1 + \varepsilon_e\ )$ and are plotted in Figure 3-1 (b) and Figure 3-1 (b), respectively. The corresponding strain hardening rate $\frac{d\sigma}{d\varepsilon_t}$ is shown in Figure 3-1 (c). The ultimate tensile strength (UTS) for both experiments are listed in Table 3-1. Since using the constant load mode does not satisfy the requirement of standard tensile test. The quantitative analysis is focusing on the result from first experiment.

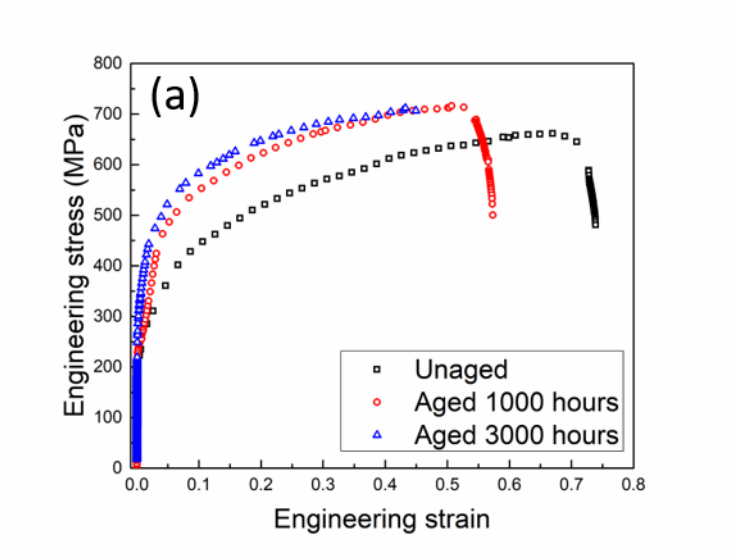

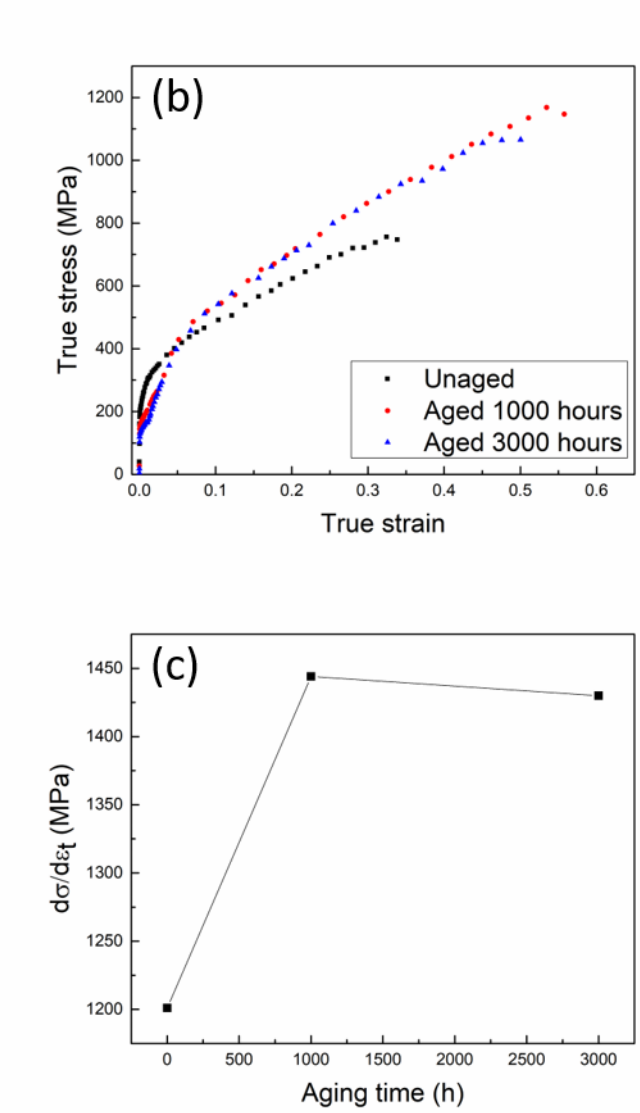

Figure 3-1. Macroscopic tensile test data for unaged/aged duplex stainless steels: (a) engineering stress vs engineering strain; (b) true stress vs true strain; and (c) strain hardening rate $d\sigma/d\sigma_t$.

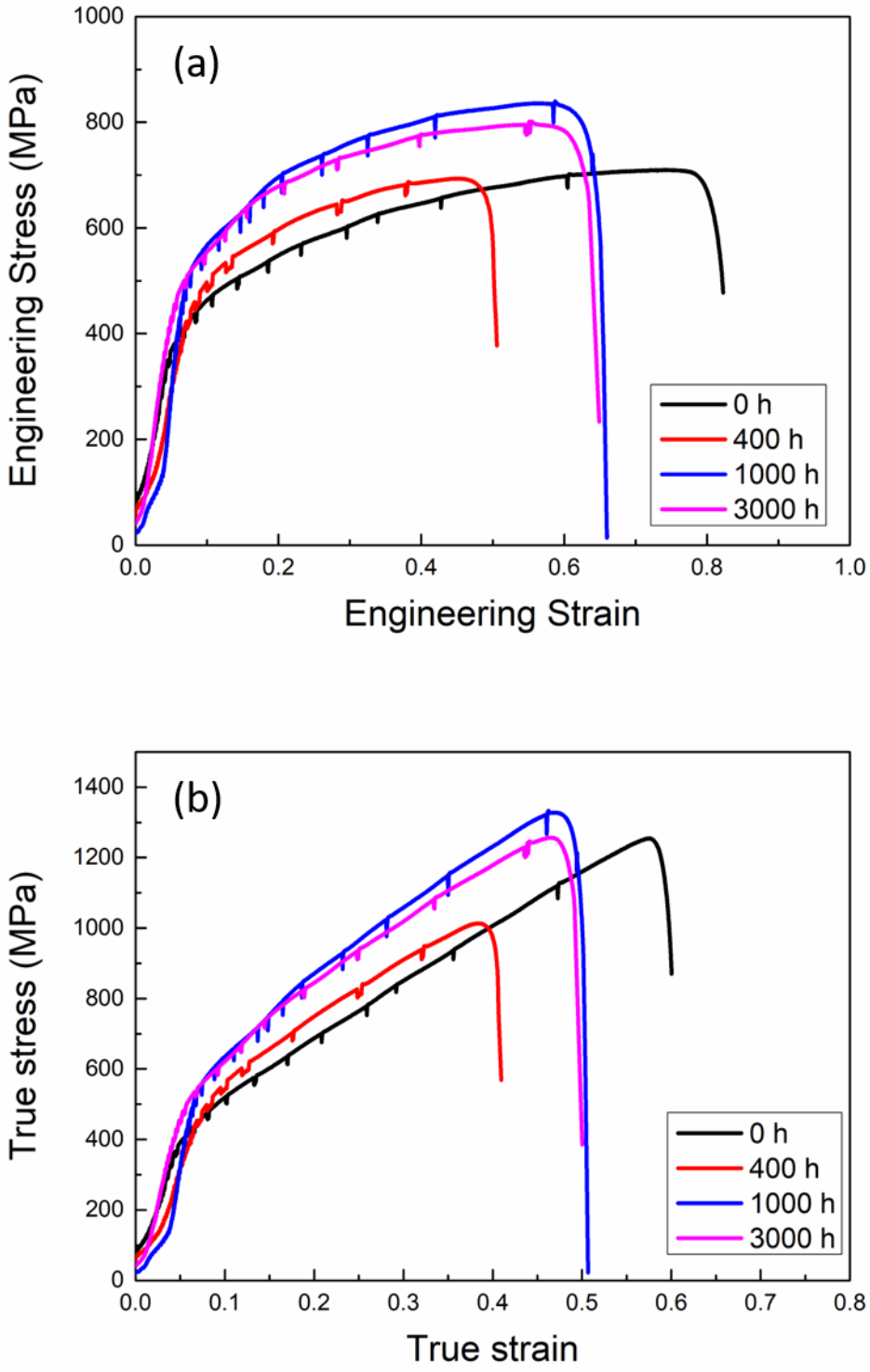

Figure 3-2. Macroscopic tensile test data for unaged/aged duplex stainless steels: (a) engineering stress vs engineering strain; (b) true stress vs true strain.

Table 3-1. UTS of the unaged/aged duplex stainless steel from two experiments using two different tensile mode.

	0 hour	400 hours	1000 hours	3000 hours
Displacement mode	661.4	N/A	716.1	711.6
Constant load mode	709.99	693.85	839.33	801.09

3.1.2 Lattice strain evolution of ferrite and austenite

The 1D profile is integrated from ±15 azimuth at axial direction to acquire the d-spacing, peak intensity and full width half maximum (FWHM). Lattice stain ε_l in this direction is calculated using equation 2-1. WAXS measurements of the undeformed samples gave a lattice parameter of 3.589 ± 0.0015 for austenite phase w./wo. thermal aging. For ferrite phase, the lattice parameter calculated from the undeformed samples were 2.869 ± 0.0008, 2.864 ± 0.0008 and 2.866 ± 0.001 for unaged, aged 1000 hours and aged 3000 hours, respectively. The average lattice parameter and standard deviation were obtained by averaging the lattice parameters given by all the {hkl} families (calculated from the fitted d-spacings) within each sample.

Figure 3-3 shows the lattice strains ε_l in the loading direction as a function of the stress from the first experiment. Six reflections: {111}, {200}, {220}, {311}, {222}, {420} for austenite phase and three reflections: {110},{200},{211} for ferrite phase are presented. The X-ray measurements of the lattice strain shows different characteristics, not only between different specimens but also between different crystal planes within one specimen. For the as cast specimen, lattice strain of different reflections from both austenite and ferrite evolve similarly, however, after thermal aging for 1000 or 3000 hours, the lattice strain difference between ferrite and austenite phase becomes obvious. Besides, the lattice strain shows an obvious anisotropy. The lattice strain of {200} is always the largest no matter in ferrite or austenite phase w./wo. thermal aging.

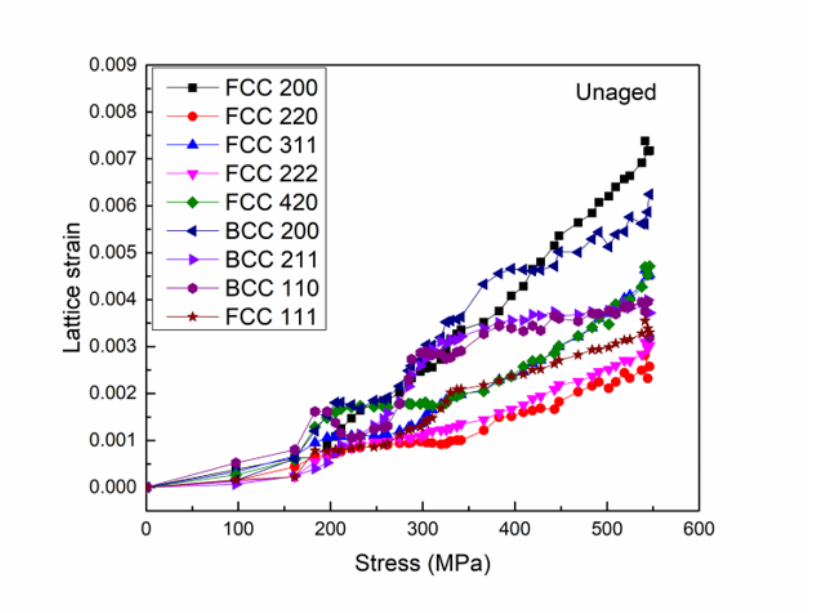

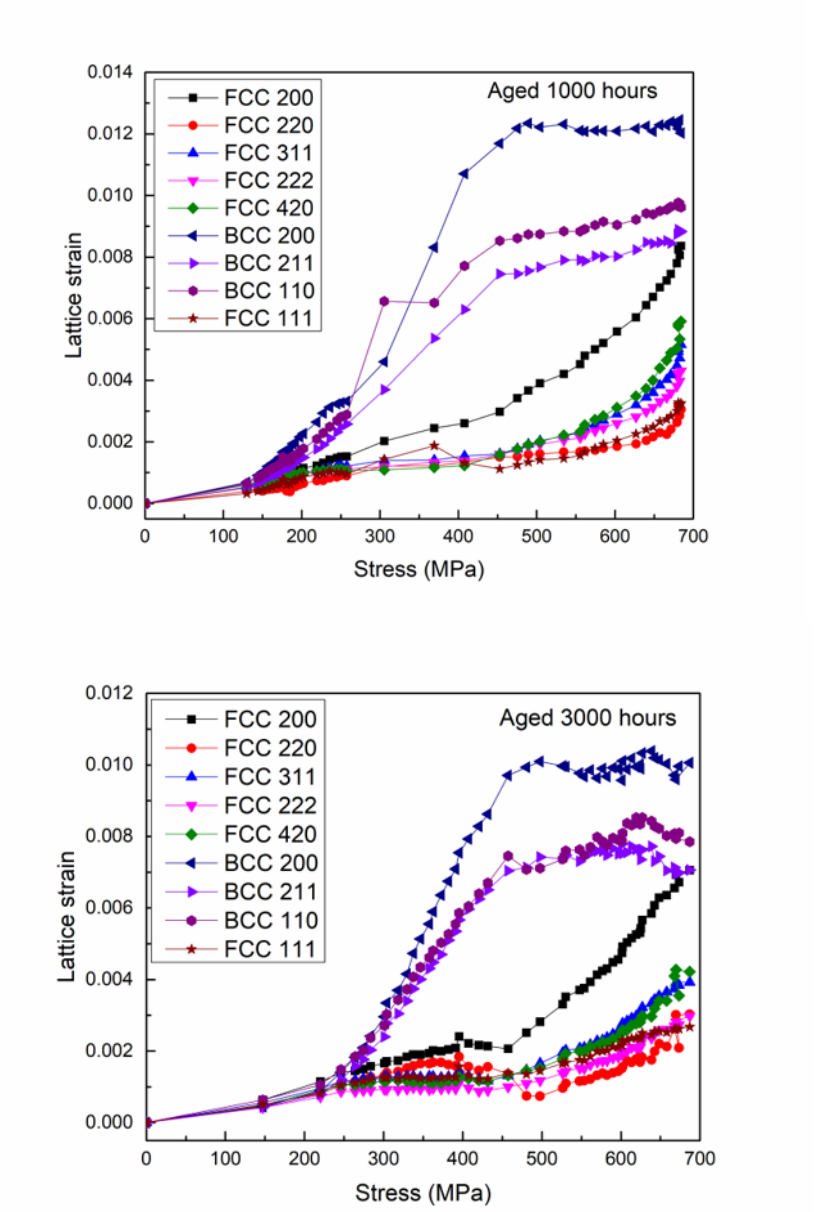

Figure 3-3. Lattice strain evolution relative to stress measured with displacement control mode.

As mentioned previously, based on the theory from ToMOTA et al [29, 30], the stress-strain curve of CASSs can be divided into four stages. Unfortunately, for the first experiment, we can only see the edge between stage (2) and (3), which correspond to the yield strength of ferrite. It is hard to see the boundary between stage (1) and (2), thus, unable to determine the yield strength of austenite. Because of that, a second experiment using the constant load mode is performed and results are listed in Figure 3-4. Using the constant load, plenty of data points below 200 MPa were successfully collected, which is especially useful to determine the yield strength of austenite. Nevertheless, due to too many reflections in Figure 3-3 and Figure 3-4, the yield strength determination is still challenging. Therefore, the detailed yield strength is

determined after the weight average lattice strain for both phases are calculated in the next section.

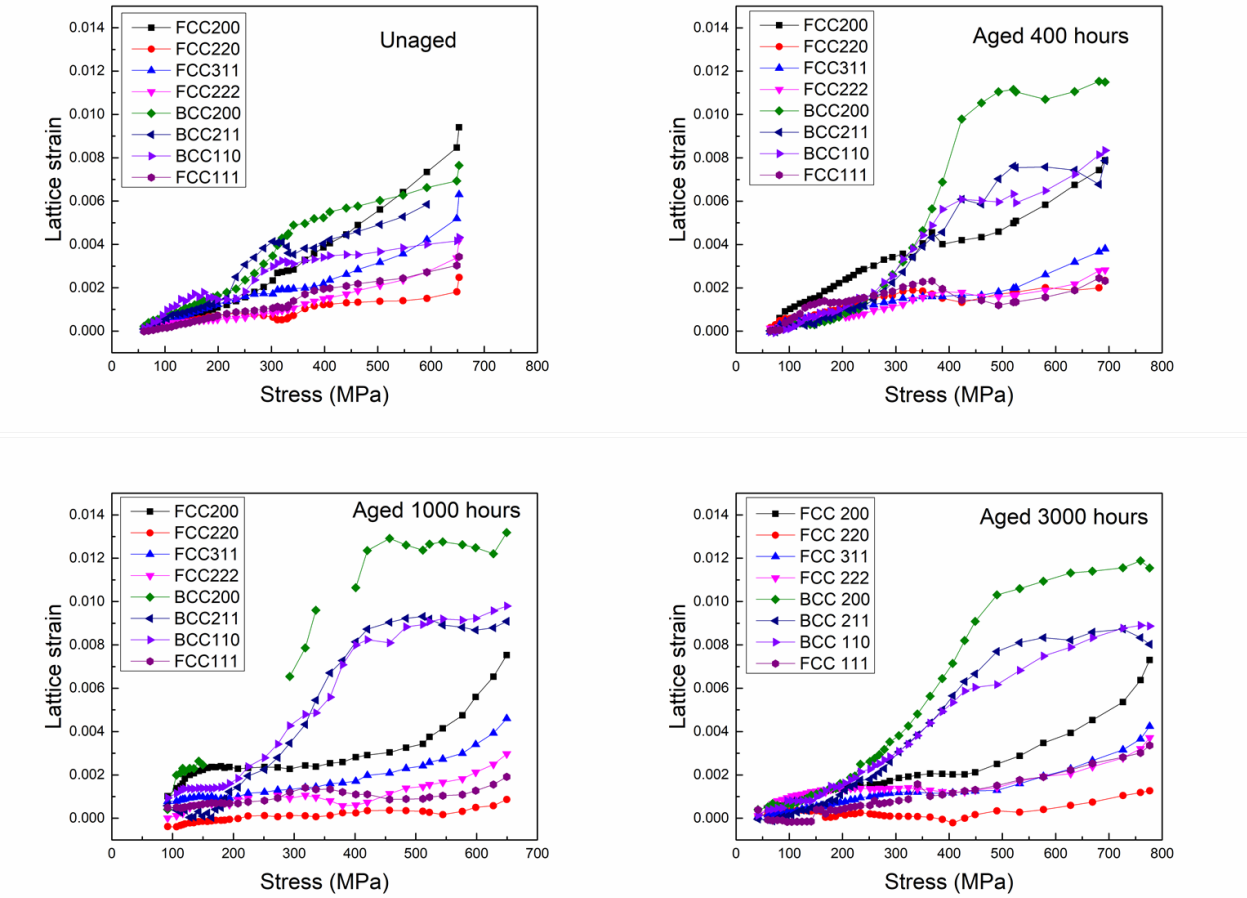

Figure 3-4. Lattice strain evolution relative to stress measured with constant load mode.

3.1.3 Load Partition Phenomenon

To better elucidate the load partition phenomenon, the weight average lattice strain was calculated using the data from both experiments. For the first experiment, the average bulk lattice strain for austenite was calculated from the lattice strains of {111}, {200}, {220}, {311} and {420} reflections while for ferrite phase it was calculated from the lattice strains of {110}, {200}, {211}. The second experiment basically used the similar lattice reflections for the weight average lattice strain calculation, however, due to the low beam energy used, the {420} reflection cannot be seen in the detector and it is excluded for the calculation. The weighted averaging algorithm developed by Daymond [33] was used for the calculation:

$$\bar{\varepsilon} = \frac{\sum_{hkl} \alpha_{hkl} \varepsilon_{hkl}}{\sum_{hkl} \alpha_{hkl}} \tag{3-1}$$

where $\bar{\varepsilon}$ is the average bulk lattice strain of the matrix, ε_{hkl} is the lattice strain of the {hkl} reflection, and α_{hkl} is the weight coefficient with the following definition:

$$\alpha_{hkl} = \frac{T_{hkl} p_{hkl} E_{hkl}}{\bar{E}} \tag{3-2}$$

p_{hkl} is the multiplicity of the {hkl} reflection, E_{hkl} is Young's modulus of the {hkl} orientation, $\bar{E}$ is the average Young's modulus of the bulk austenite matrix, and T_{hkl} is the Harris texture index [34]:

$$T_{hkl} = \frac{I_{hkl_j}/R_{hkl_j}}{\frac{1}{n}\sum_{j=1}^{n} I_{hkl_j}/R_{hkl_j}} \tag{3-3}$$

where I_{hkl} is the integrated intensity of the {hkl} reflection and R_{hkl} is the theoretical integrated intensity of the {hkl} reflection produced by an untextured sample. Due to the capability of the detector, both experiments were conducted using the step mode, the data points linear region have some fluctuation, which may affect the accurate determination of the lattice modulus. To avoid this effect, the lattice modulus is referred from other experiments [21-24, 35] whose signal was acquired using a electronic detector that allow the DP to be recorded simultaneously and continuously during the tensile test. The weight average lattice strain plot for first experiment is shown in Figure 3-5 while the Figure 3-6 shows the result from second experiment. From these plots, the three different stages are much clear comparing with the lattice strain plot.

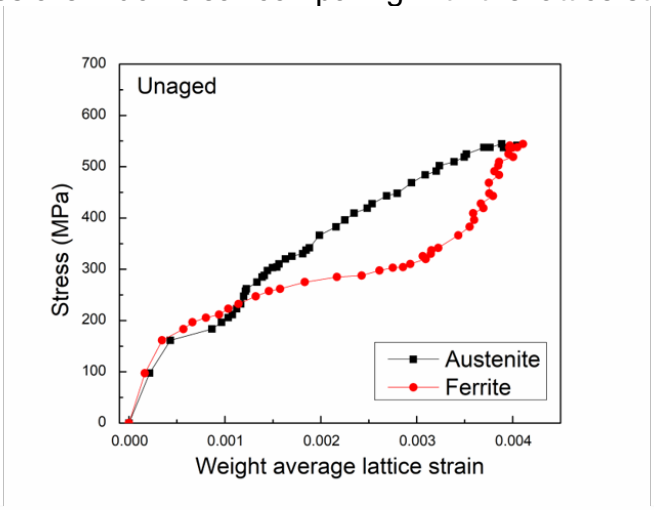

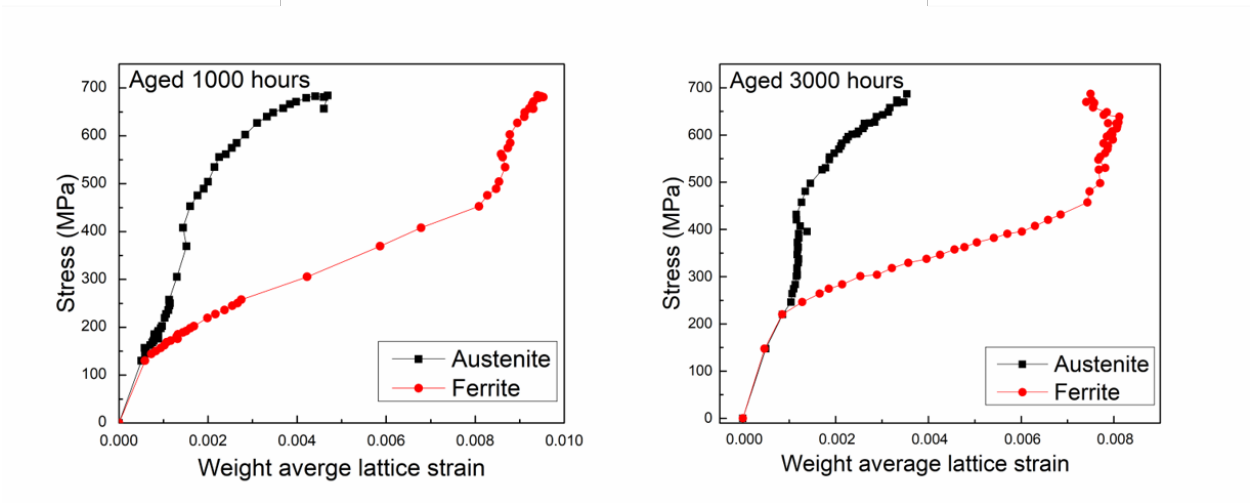

Figure 3-5. Stress versus weight average lattice strain measured with displacement control mode.

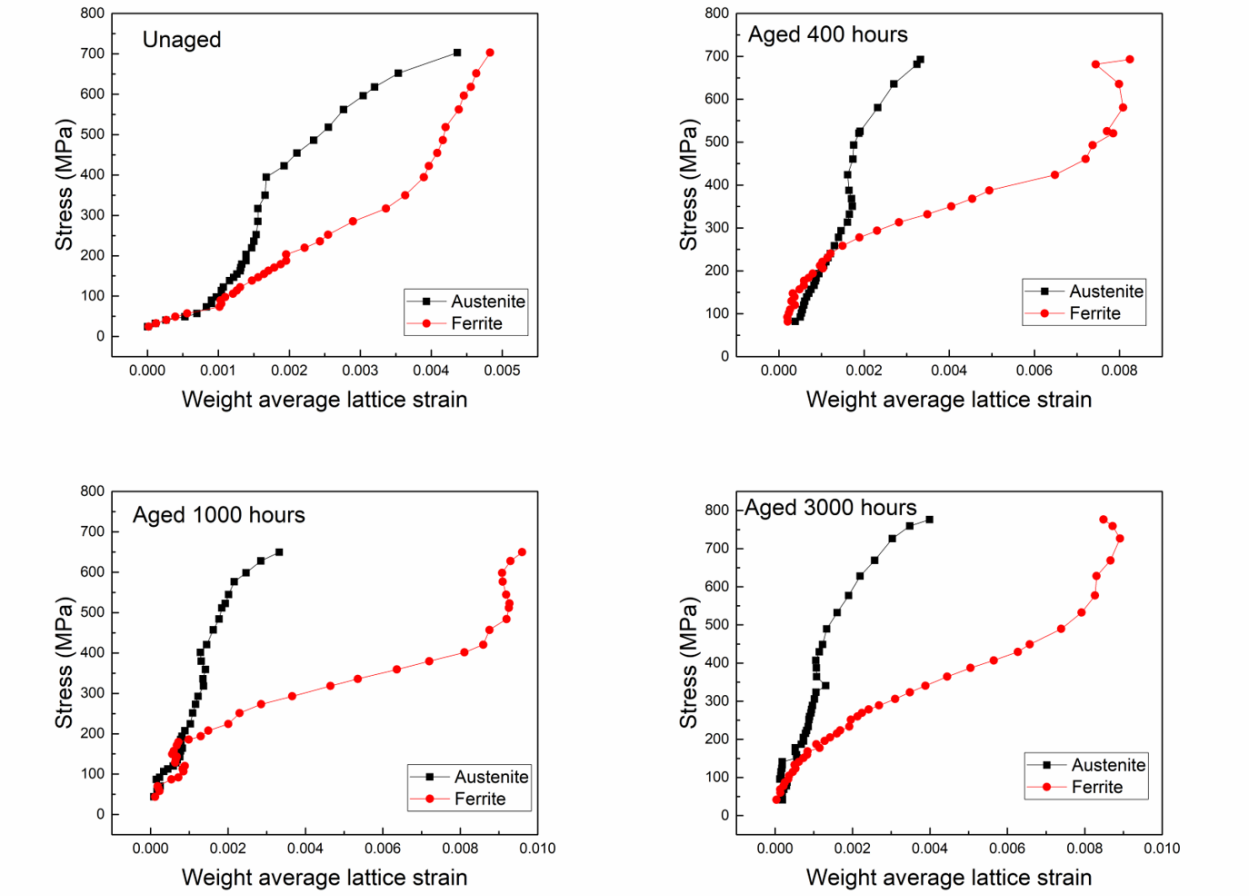

Figure 3-6. Stress versus weight average lattice strain measured with constant load mode.

The yield strength of both austenite and ferrite phase are determined based on ToMOTA's theory and the results are listed in Table 2-3. Both experiments can give us the yield strength of ferrite phase, while only using constant load control mode can determine the yield strength of austenite. The "CL" stands for constant load mode while "DC" stands for displacement control mode.

Table 3-2. Yield strength of austenite/ferrite phase from both experiments using displacement control mode and constant load mode.

	Austenite_CL	Ferrite_CL	Ferrite_DC	Ferrite_ave
Unaged	216	320	310	315
Aged 400 hours	230	388	N/A	388
Aged 1000 hours	185	420	453	436.5
Aged 3000 hours	211	449	457	453

3.1.4 Dislocation density evolution

The dislocation density evolution analysis is performed using the data from first experiment, not only because the first experiment is a more strictly defined tensile test but also it has more data points than the second experiment. The evolution of dislocation density is obtained by analyzing the diffraction peak broadening in the full width at half maximum (FWHM) for both ferrite phase and austenite phase using modified Williamson-Hall (W-H) model [36]. In the modified W-H model, the FWHM is affected by both dislocation density and crystalline size. The equation is

$$\Delta K \cong \frac{0.9}{D} + (\frac{\pi M^2 b^2}{2})^{\frac{1}{2}} \rho^{\frac{1}{2}} K C^{\frac{1}{2}} + O(K^2 C) \quad (3\text{-}4)$$

ΔK is related to the peak broadening by $\Delta K = \frac{2\cos\theta \Delta\theta}{\lambda}$ (where θ is the diffraction angle and λ is the incident X-ray wavelength). On the right-hand side of equation 2-5, the first term represents the contribution of crystalline size, where D is the average crystalline size. The second term represents the contribution of dislocations, where $K = \frac{2\sin\theta}{\lambda}$, M is a constant related to the cutoff radius of the dislocations, b is the Burgers vector, and C is the average dislocation contrast factor. In cubic systems, the contrast factor is determined by $\bar{C} = \bar{C}_{h00}(1 - qH^2)$, where $\bar{C}_{h00}$ is the average contrast factor of {h00} reflections and H^2 is a fourth order invariant given by $\frac{h^2k^2+h^2l^2+k^2l^2}{(h^2+k^2+l^2)^2}$. The values of $\bar{C}_{h00}$ and q are material dependent and are different for screw and edge dislocations.

For the CASSs under three different conditions, since the diffraction rings deviate from circles due to deviatoric strains, the patterns were not integrated over the entire azimuth initially; instead, it is caked at every 20 azimuths. Because of the texture effect, five cakes were selected for the analysis to make sure all the peaks considered here have strong enough intensity for peak fitting. The integrated 1D profiles is later fitted to get the FWHM using the Matlab code. The instrumental broadening is subtracted by analyzing the FWHM of LaB_6. After subtracting the instrumental FWHM, the result is averaged using integrated intensity weighting. Finally, the dislocation density and the optimal edge/screw dislocation fraction was obtained by linear fitting in the Matlab using equation 2-5. The crystal plane (111) (200) (220) (311) (222) (420) and the crystal plane (200) (211) (220) (310) are included for peak width analysis for both austenite phase and ferrite phase, respectively.

It is necessary to get the dislocation contrast factor for both phases before the linear fitting using modified W-H model. For austenite phase, the specific parameters that were used to calculate the contrast factor are acquired from reference [24]. For ferrite phase, dislocation contrast factors were calculated using the ANIZC software [37] as illustrated in reference [22]. Dislocation contrast factors were calculated under two scenarios, namely, assuming the dislocation population is all edge type dislocations {110} <111> or all screw type dislocation <111>. Since both edge and screw dislocation exist in the crystal, the $\bar{C}$ has the following expression:

$$\bar{C} = \upsilon_s C_{screw} + (1 - \upsilon) C_{edge} \quad (3\text{-}5)$$

To find the optimum $\bar{C}$, the modified W-H fitting was performed sing the $\bar{C}$ with the screw/edge ratio ranging from 0 to 1 with step size 0.01 in Matlab, and the $\bar{C}$ that gave the highest R_{square} value was selected, giving the optimum edge/screw dislocation

fraction. In this way, the evolution of the edge/screw dislocation fraction can be tracked with deformation. The burger vector used for austenite is $b = \frac{a}{2} < 110 >= 2.553$ and $b = \frac{a}{2} < 111 >= 2.481$ for ferrite. For simplicity, M=1 was used for dislocation density calculation.

The dislocation density evolution during plastic deformation of austenite phase for three different condition are listed in Figure 3-7 (a). The dislocation density is calculated from the WAXS result. The error bar was calculated from the uncertainties of peak fitting and are first order estimates of the deviation of the 1D line profile from ideal pseudo-Voigt functions. As can be seen, the dislocation density evolution for austenite is consistent w./wo. thermal aging, which means that the thermal aging does not affect the dislocation density evolution in austenite phase. In Figure 3-7 (b), the true stress is plotted versus square root of dislocation density $\sqrt{\rho}$. The good linearity shows the dominance of dislocation glide in plastic deformation in austenite. Also, the hardening behavior of austenite is not significantly altered by thermal aging. For ferrite phase, its dislocation density evolution is plotted in Figure 3-8. It shows that although the ferrite phase has the similar dislocation density when it is close to failure for both unaged and aged condition, the dislocation density of aged ferrite phase propagated faster at the early stage of plastic deformation comparing with the unaged condition. The dislocation density calculated from WAXS for both austenite and ferrite phase that is close to elastic region and close to failure w./wo. thermal aging is listed in Table 3-3, respectively.

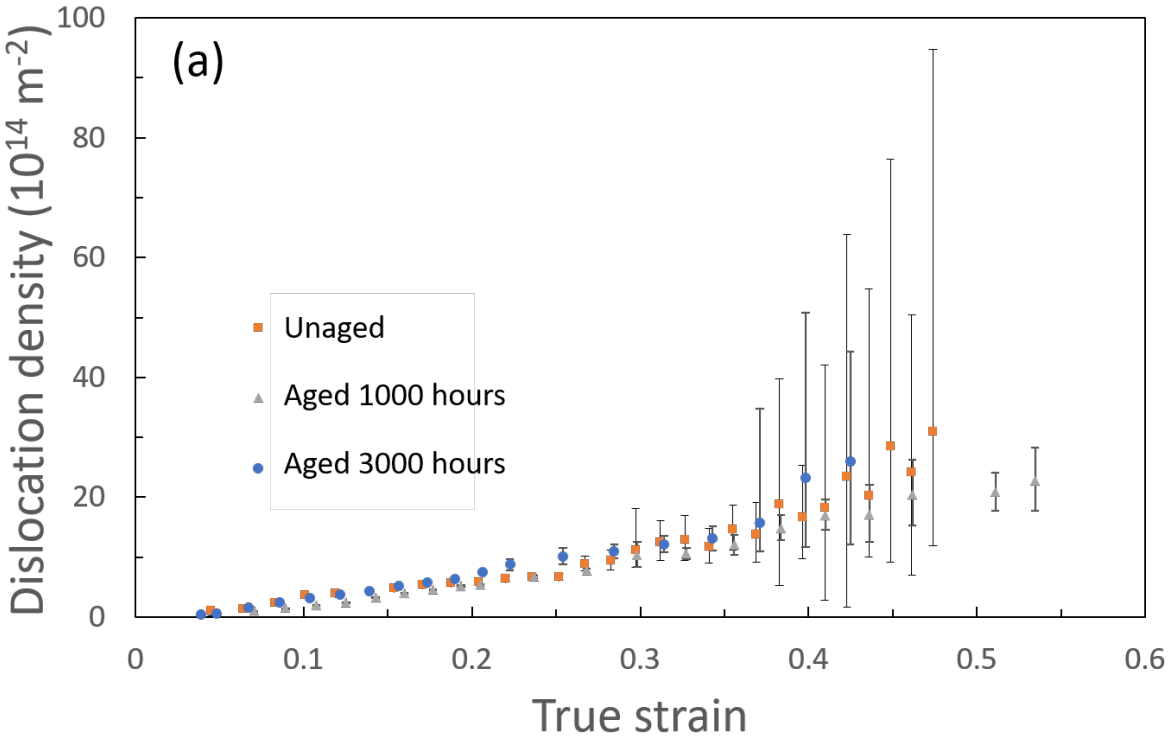

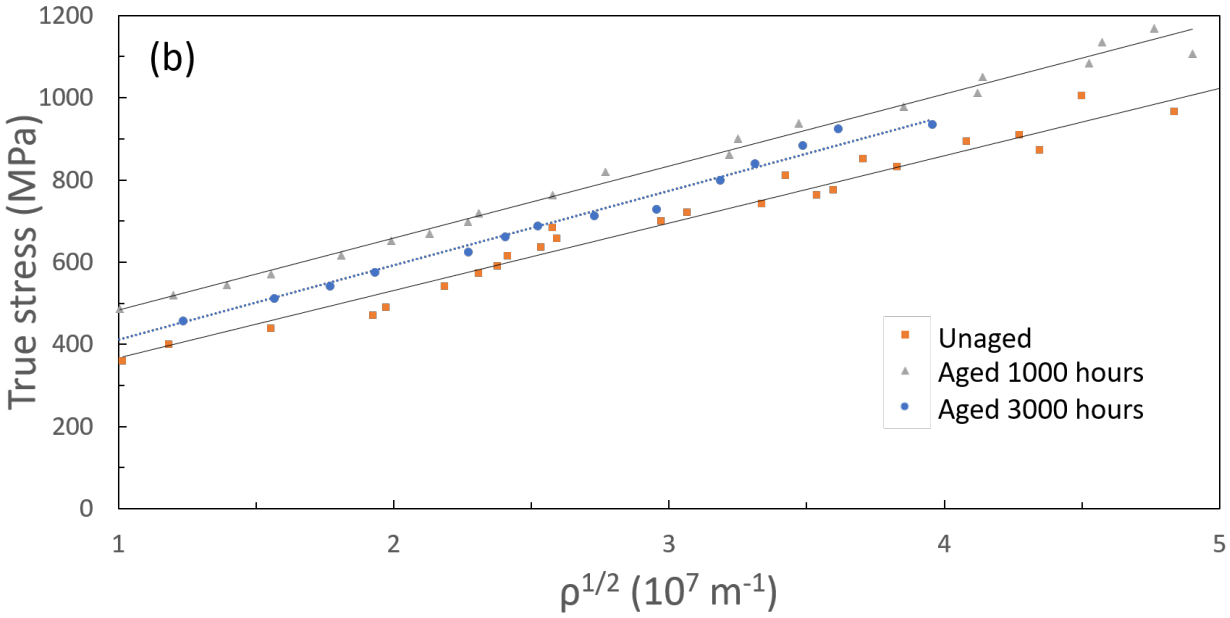

Figure 3-7. (a) Dislocation density evolution for austenite. (b) Linear fit of true stress vs $\sqrt{\rho}$.

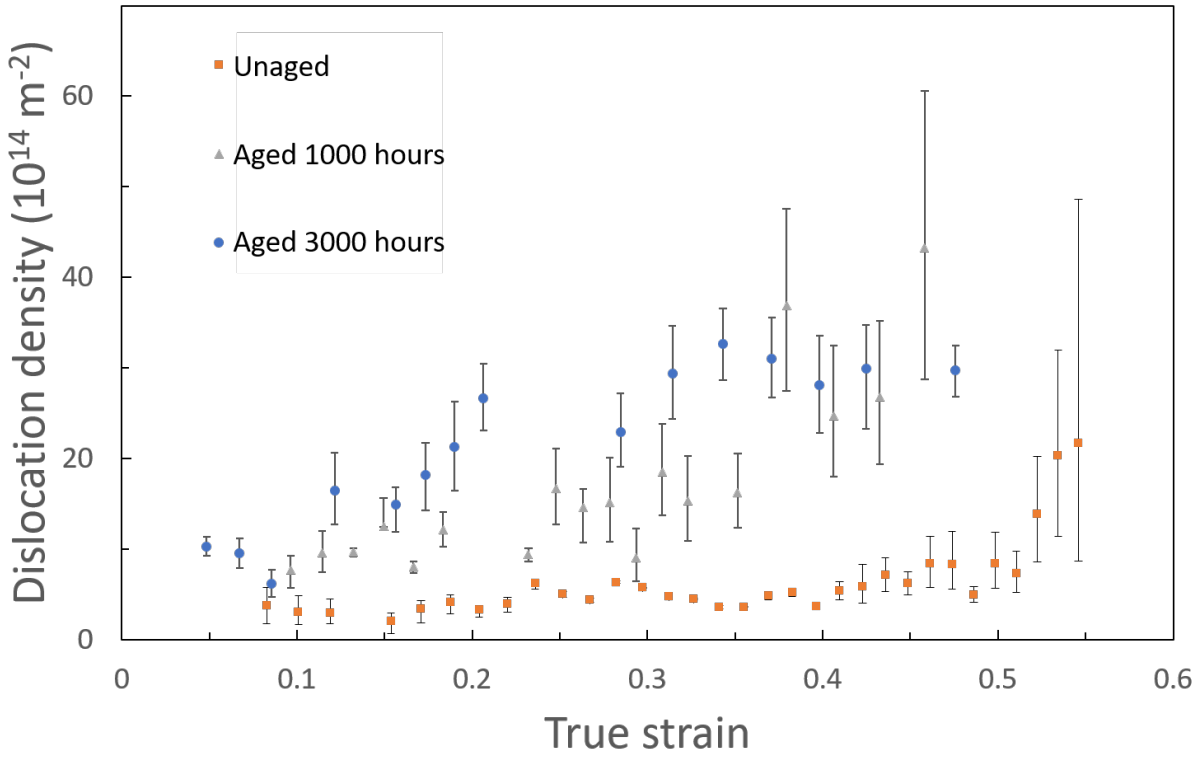

Figure 3-8. Dislocation density evolution for ferrite.

Table 3-3. Dislocation density calculation for both ferrite and austenite phase close to elastic region and close to failure.

	Austenite		Ferrite	
	Elastic region	At failure	Elastic region	At failure
unaged	1.4×10^{14}	2.9×10^{15}	3.7×10^{14}	2.2×10^{15}
1000 hours	1.4×10^{14}	2.8×10^{15}	7.7×10^{14}	4.3×10^{15}
3000 hours	1.5×10^{14}	2.6×10^{15}	6.1×10^{14}	3.0×10^{15}

3.1.5 Deformation-induced Martensite Transformation

It has been reported that the HCP ε-martensite forms in the duplex stainless steel after ~20% deformation and the deformation induced ε-martensite has a preferred azimuth angle in the Debye ring, usually at around the 45˚, 135˚, 225˚and 315˚[38]. During the data processing, the $\{10\bar{1}0\}$ peak shows at the 1D profile that was integrated at 245˚over a range of $\pm10°$ as the strain increases (as shown in Figure 3-9). However, the intensity of the deformation induced ε-martensite is very low comparing with the peak from austenite phase, therefore, the appearance of ε-martensite has minor effect on our peak width analysis on austenite.

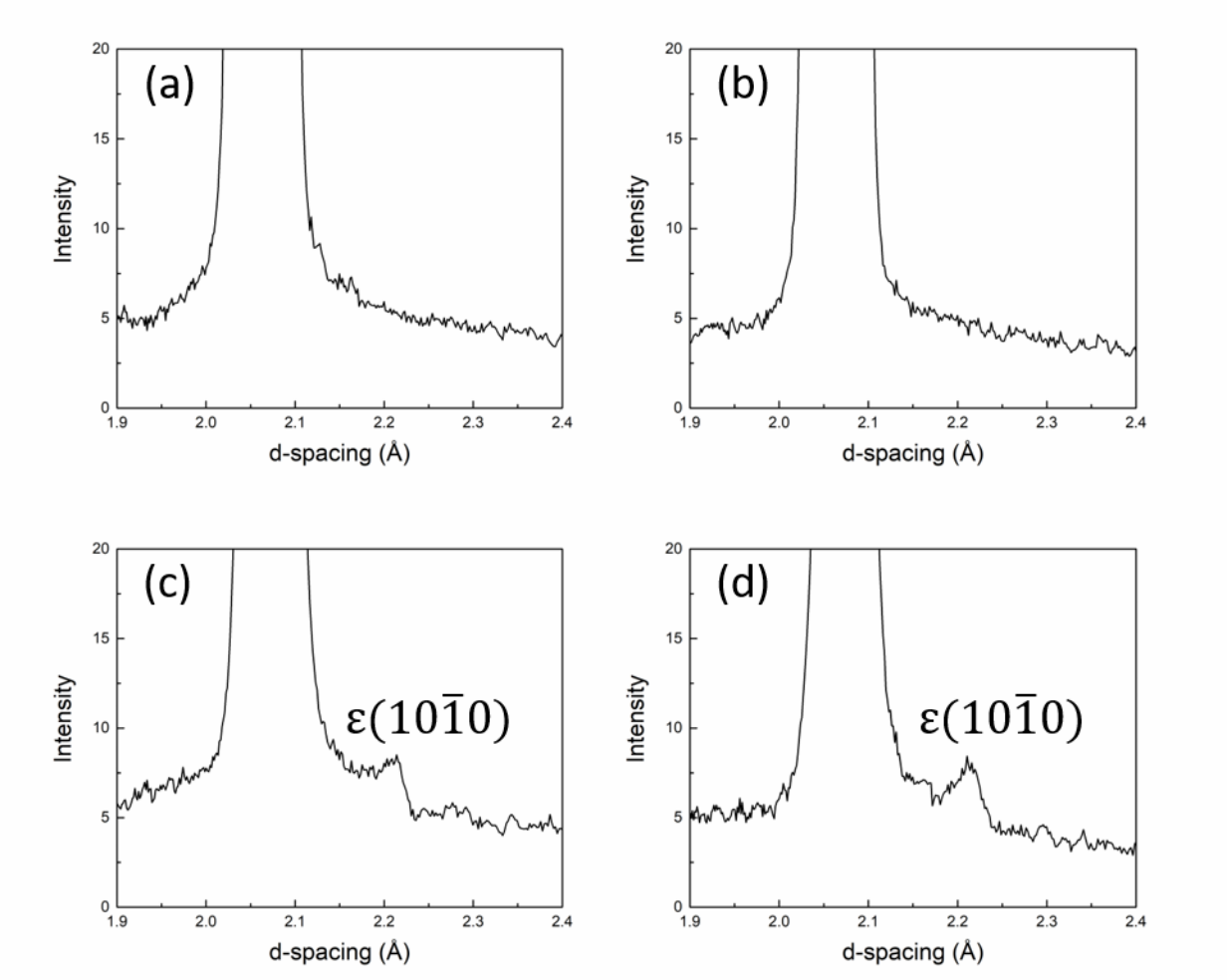

Figure 3-9. The 1D profiles along the 245˚azimuth for the duplex stainless steel after different amount of deformation, from the left to right, the deformation is 0%, 1.1%, 16.1% and 36.1%.

3.2 APT Investigation of Neutron Irradiated CASSs

3.2.1 Chemical Composition of Ferrite

APT measured chemical compositions of the ferrites at different conditions was listed in Table 3-4 and the standard deviations (SD) are calculated over all the measured specimens. For all the alloying elements in the stainless steel, the concentrations show a great consistence.

Table 3-4. APT measured chemical composition (wt.%) of the ferrite at difference conditions.

	Fe	Cr	Ni	Si	Mn	Mo	V	C	S	P
3 dpa aged	68.400	24.358	4.992	1.108	0.465	0.560	0.091	0.001	0.014	0.011
3 dpa unaged	68.137	24.628	5.037	1.057	0.479	0.538	0.098	0.002	0.015	0.008
5 dpa	68.388	24.620	4.953	1.004	0.492	0.455	0.070	0.007	0.007	0.005
10 dpa	67.905	25.023	4.965	1.019	0.518	0.470	0.067	0.002	0.027	0.003
20 dpa	68.259	24.562	4.950	1.040	0.481	0.555	0.097	0.030	0.019	0.008
40 dpa	68.271	24.627	4.931	1.057	0.478	0.496	0.084	0.040	0.009	0.007
SD	0.183	0.230	0.079	0.040	0.024	0.044	0.015	0.021	0.012	0.003

3.2.2 Spinodal Decomposition

Figure 3-9 shows the Cr atom map in different conditions. The Cr atomic maps were constructed from a slice of 5 nm in thickness at the Y middle plane of each APT tip. The corresponding Cr frequency distribution in ferrite is plotted in Figure 3-10**.**Error! Reference source not found. Since spinodal decomposition is one of the primary microstructural evolution during thermal aging and neutron irradiation, and previous research has claimed its negative effect on mechanical property of cast duplex stainless steel. Therefore, it is beneficial if we can quantify the spinodal decomposition due to thermal aging and neutron irradiation. With spinodal decomposition being quantified, it is possible to reveal the mathematical relationship between spinodal decomposition and mechanical property like Chen and R. Badyka [39, 40] has reported. In this present paper, a new method proposed by Zhou [41] using radial distribution function (RDF) analysis was applied to quantify the wavelength and magnitude of the spinodal decomposition based on Cr atom. RDF analysis provides an average radial concentration around each atom in the APT reconstruction data for a particular element as a function of radial distance from the center atom. This average radial concentration profile for each element, when divided by the average bulk concentration of that element, provides the bulk normalized concentration plots. The compositional amplitude is calculated using the bulk normalized concentration in the Cr-Cr RDF value at a distance of 0 nm (RDF (0 nm)) using the following equation:

$$A = C_0\sqrt{2\big(RDF(0nm)\big) - 1)} \tag{3-6}$$

where C_0 is the bulk Cr composition of the atom probe reconstruction. In the RDF plot, the second peak specifies a statistically nearest distance between two Cr-rich regions in three dimensions, and thus the distance of the second peak is captured as the wavelength of spinodal decomposition. This method has been applied by Timothy [42] and gives a reasonable result.

For our situation, the same method is applied, however, comparing with Zhou and Timothy, our specimens showed a much more significant spinodal decomposition, the wavelength is larger than 10 nm (as shown in Figure 3-11), which is beyond the RDF limitation of the IVAS software. Under this condition, it is reasonable to assume that spinodal decomposition is symmetric and two times the distance of the first trough is the wavelength of spinodal decomposition. The calculated results are listed in Table 3-5. Comparing with 5 dpa and 10 dpa condition, it seems either the wavelength or the magnitude of spinodal decomposition does not show an obvious change, indicating the spinodal decomposition has saturated at neutron irradiation to 5 dpa under that dose rate. However, once the dose reaches 20 dpa, something happened and induce the further spinodal decomposition, thus its magnitude boosts significantly. Besides, it is noticed that comparing 3 dpa and 5 dpa condition, 3 dpa condition has a smaller wavelength and larger magnitude, as irradiation dose does not change them too much, these differences should result from the dose rate difference.

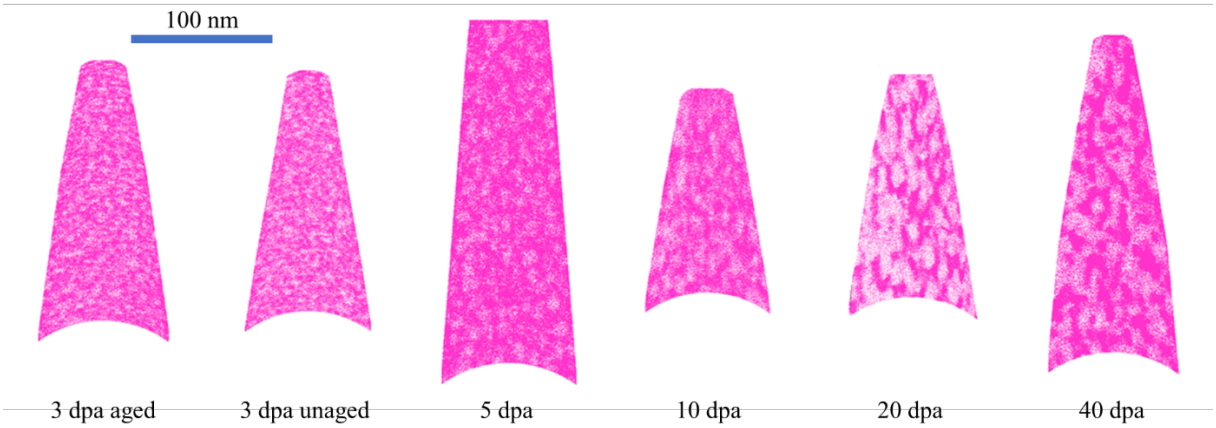

Figure 3-9. Spinodal decomposition of ferrite in cast stainless steels, the blue color represents Cr atoms.

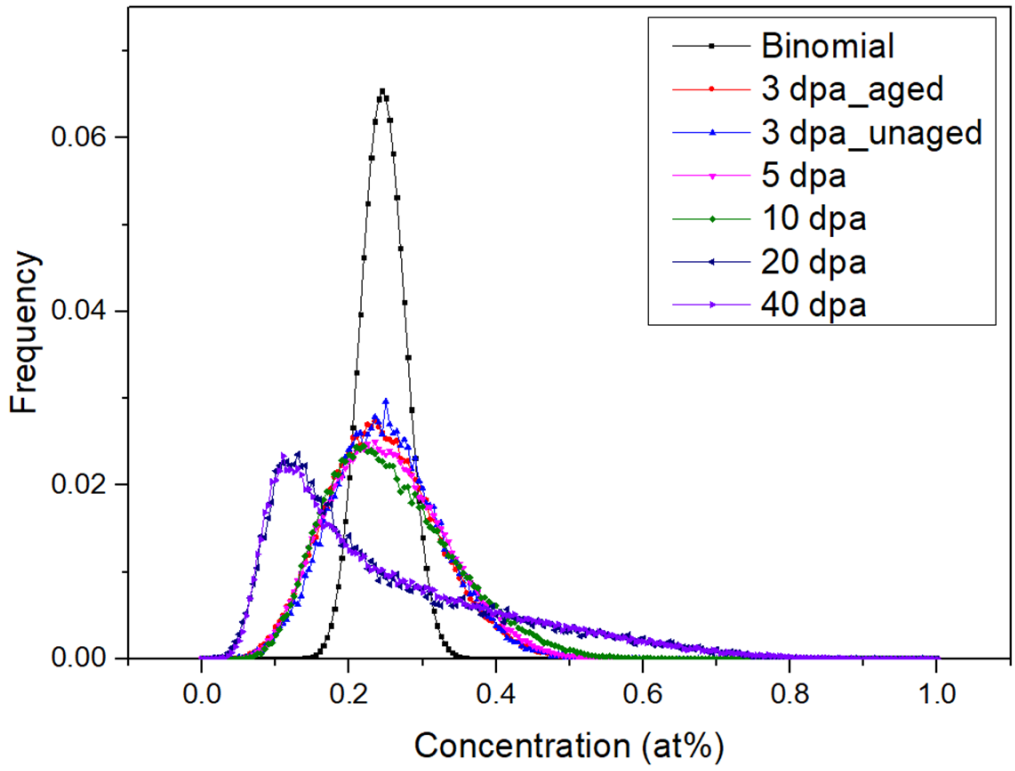

Figure 3-10. Cr elemental frequency distributions in ferrites upon different conditions.

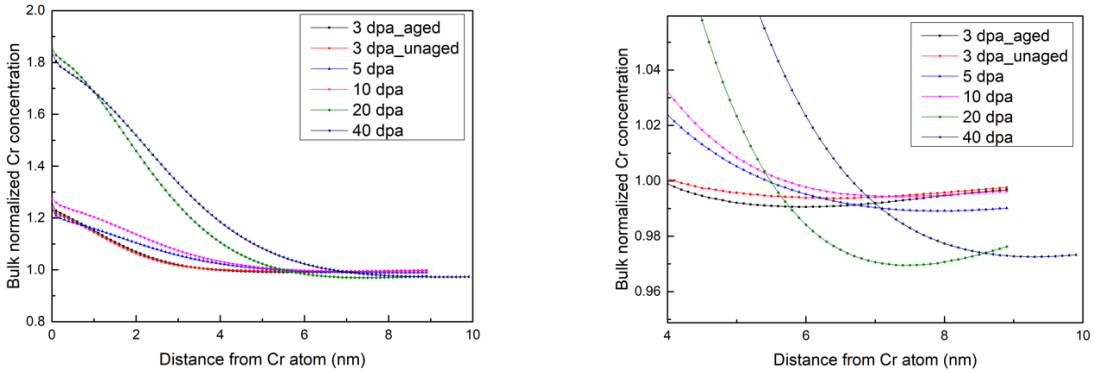

Figure 3-11. Cr-Cr Radial distribution function plots: bulk normalized Cr composition at a distance from a Cr atom. The right picture is a magnification of the left one to show the trough.

Table 3-5. Amplitude (at%) and wavelength (nm) from Cr-Cr radial distribution functions in bulk ferrite phase.

	Wavelength, λ (nm)	Amplitude (at%)
3 dpa unaged	13.2	16.72
3 dpa aged	12.4	16.99

5 dpa	16.4	15.99
10 dpa	15.5	16.86
20 dpa	14.93	29.66
40 dpa	16.47	32.74

3.2.3 G-phase Precipitation

Low temperature thermal aging (< 400°C) of ferrite phase in cast duplex stainless steel is likely to induce the formation of G, R and π phases. Figure 3-12 shows the G phase precipitation represented with the Mn, Si and Ni atomic map. Similar to spinodal decomposition, the atomic map was constructed from a slice of 5 nm in thickness at the Y middle plane of each APT tip. Like the result from low dose neutron radiation [43], the atomic map of Mn, Si and Ni show a cluster phenomena. Comparing the position of Mn-Si-Ni cluster with the spinodal decomposition induced Cr rich phase, it is apparently the clusters are forming at the interdomain region of spinodal decomposition. The position of G-phase forming at interdomain region of spinodal decomposition has been reported by several publications. A. MATEO [5] claimed that the spinodal decomposition implies an enrichment of Cr and Fe rich region, respectively. The Fe rich region rejects Si and Mo atoms while the Cr rich region rejects Ni and Mn atoms. As a consequence, the rejected solute atoms: Ni, Si and Mn, form G-phase at the interdomain region. Timothy [42] conducted Pearson correlation coefficient analysis on different elements and claims that the Ni is following a similar trend with Fe and Cr while Si and Mo show a clear delay during phase separation. They gave an explanation based on the thermodynamics. The Ni has a high concentration in ferrite but a very low miscibility in equilibrium in both Cr and α-Fe. Therefore, they thought the Ni clustered at interdomain region first. As Si and Mn has greater solubility in Ni than in bcc-Fe and bcc-Cr, they have higher potential to diffuse into Ni and form G-phase.

Either A. MATEO or Timothy are investigating the G-phase formation due to thermal aging. Whether the G-phase formation due to neutron irradiation will be the same as thermal aging still need to be clarified. In this present paper, the Pearson correlation coefficient analysis is performed on the major elements of G-phase cluster and the result is plotted relative to irradiation dose in Figure 3-13. The Pearson correlation (μ) is based on the chi square (χ^2) test with datasets that vary in size [44], therefore, it is useful here for compare ferrite of different conditions since each tip has different volume. The Pearson coefficient is as follows, where N is the number of bins containing 200 ions within the sample:

$$\mu = \left(\frac{\chi^2}{\chi^2 + N}\right)^{0.5} \tag{3-7}$$

the value of μ is between 0 and 1, with 0 corresponding to fully homogeneous and 1 to a high degree of phase separation.

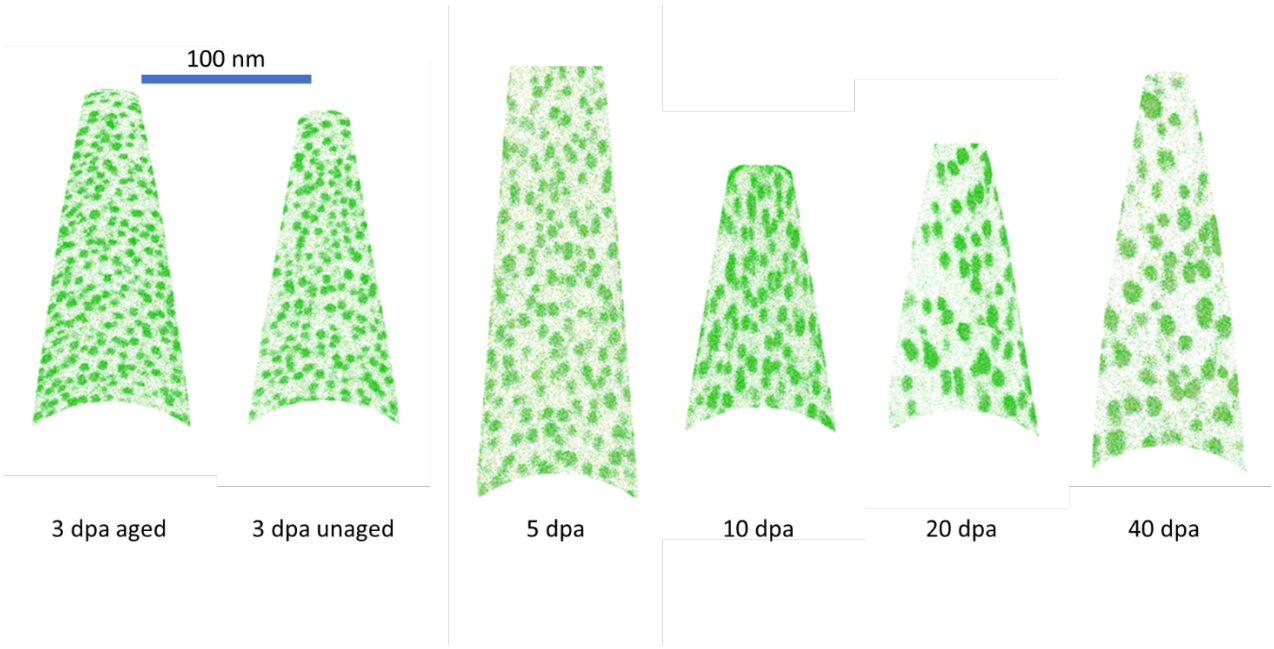

Figure 3-12. Mn-Si-Ni atomic map upon different conditions.

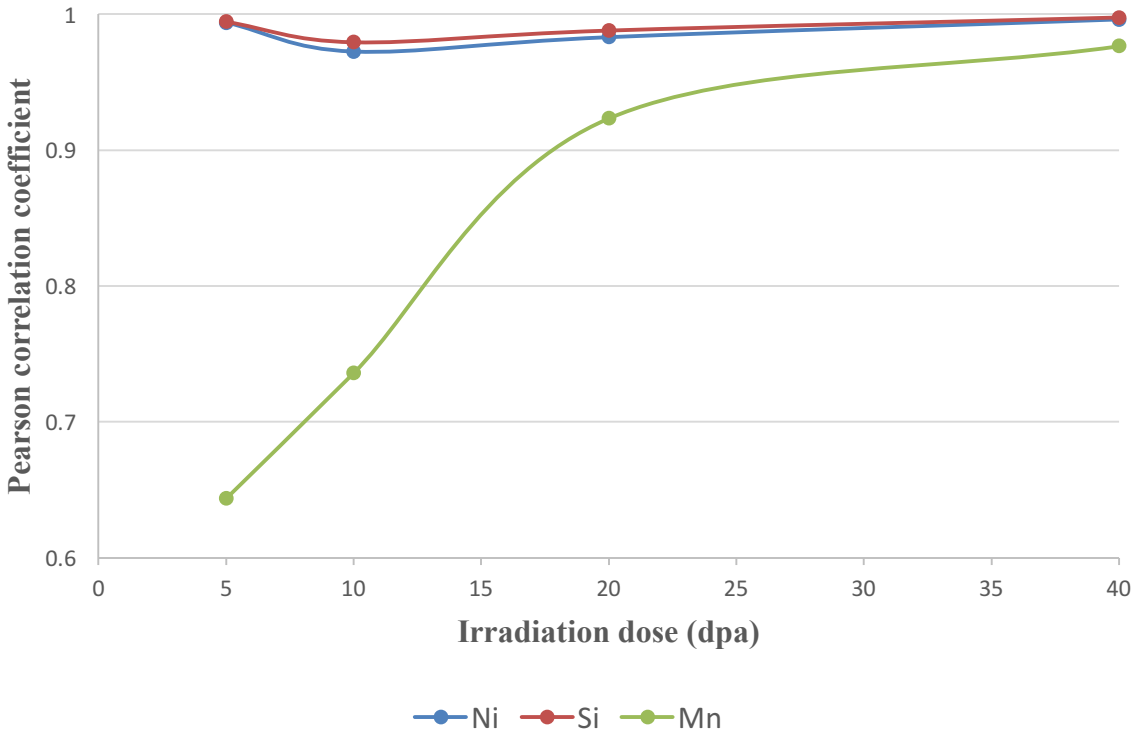

Figure 3-13. Pearson correlation coefficient of Ni, Si and Mn as a function of irradiation dose.

Besides understanding atomic evolution during the G-phase cluster formation, its chemical composition, cluster size, number density and volume fraction also need to be investigated. The Mn-Ni-Si cluster was quantified using a widely accepted maximum

separation method (MSM) [43, 45]. To create a cluster analysis using IVAS software, parameters of "ions" (element), "orders" (ions), "erosion distance d_e", "d_{max} (nm)", "N_{min}" and "envelop parameter L (nm)" have to be specified. As suggested by our previous research, the Mn ion is most representative of the G-phase cluster as Ni and Si ions is sometimes are prone to aggregate themselves. For the parameter determination in the present paper, the 4th order nearest neighbor distribution of Mn is selected and fitted with two Gaussian distributions. The value of dmax is determined as the distance between zero and the crossover of two fitted Gaussian distributions while the value of d_e is the distance between the peak of left Gaussian distribution and the crossover of two Gaussian distributions (as shown in Figure 3-14). The N_{min} is determined followed the IVAS manual by performing the cluster size distribution analysis. An ideal N_{min} (cluster size) to use for a cluster analysis is one to the right of where the line represents of the random distribution goes to zero (as shown in Figure 3-15).

The chemical composition of precipitates is shown in Table 3-6. Two inverse phenomena are observed. From 5 to 10 dpa, the concentration of Si-Mn-Ni in the cluster is decreasing while matrix atoms Fe/Cr is increasing, however, from 10 to 20 dpa, just the inverse, the concentration of Si-Mn-Ni in the cluster is increasing while matrix atoms Fe/Cr is decreasing. This phenomenon is interesting as it is closely correlating with the spinodal decomposition. Either the enhancement of spinodal decomposition induce the matrix atoms (Fe/Cr) in the precipitates decompose to the Fe-rich and Cr-rich phase or the compositional change of the precipitate leading to the ejection of matrix atom. The ejected matrix atom further diffused to the to the Fe-rich and Cr-rich phase and increase the magnitude of spinodal decomposition. An explanation is proposed in this paper and the details are presented in the discussion section.

The mean size, number density and volumetric fraction of the precipitates have been listed in Table 3-7. The A mean size evolution of the precipitates versus the dose is plotted in Figure 3-16.

Table 3-6. Chemical composition of G-phase precipitates upon different irradiate co ndition.

	Fe	Cr	Ni	Si	Mn	Mo	V	C	S	P
3 dpa_unaged	55.274	16.958	17.595	7.620	1.728	0.235	0.056	0.007	0.060	0.061
3 dpa_aged	56.577	16.012	17.312	7.638	1.667	0.275	0.053	0.002	0.031	0.081
5 dpa	56.937	15.784	17.117	6.550	1.427	0.167	0.059	0.029	0.013	0.037
10 dpa	57.537	16.310	13.268	5.048	1.374	0.200	0.089	0.011	0.010	0.017
20 dpa	52.901	11.699	21.632	9.237	2.394	0.416	0.054	0.098	0.058	0.065
40 dpa	45.822	10.247	27.098	11.846	3.036	0.494	0.036	0.128	0.017	0.089

Table 3-7. The number density, mean size and volumetric fraction of the G-phase precipitates.

	Number density (m^{-3})	Mean radius (nm)	Volume fraction (%)
3 dpa unaged	$(1.48 \pm 0.17)\times10^{24}$	1.06±0.05	0.72±0.05
3 dpa aged	$(1.44 \pm 0.06)\times10^{24}$	1.06±0.03	0.72±0.07
5 dpa	9.61×10^{23}	1.39	1.11

10 dpa	$(7.44 \pm 0.16)\times10^{23}$	1.72±0.05	1.67±0.17
20 dpa	$(7.16 \pm 0.73)\times10^{23}$	1.51±0.15	1.01±0.26
40 dpa	$(4.18 \pm 0.31)\times10^{23}$	1.76±0.03	1.17±0.15

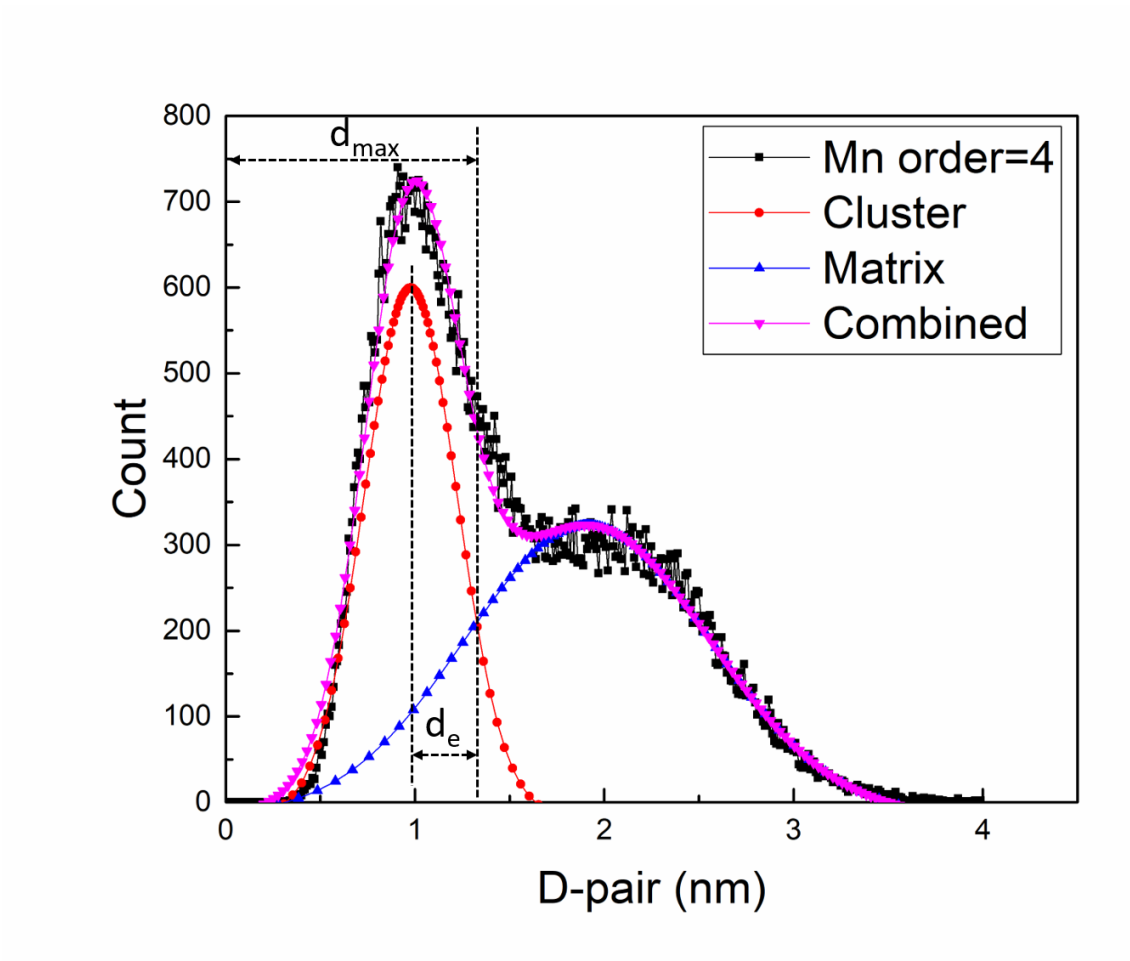

Figure 3-14. Gaaussian peak deconvolution for the 4 th order nearest neighbor distribution and determination of d_{max} and d_e.

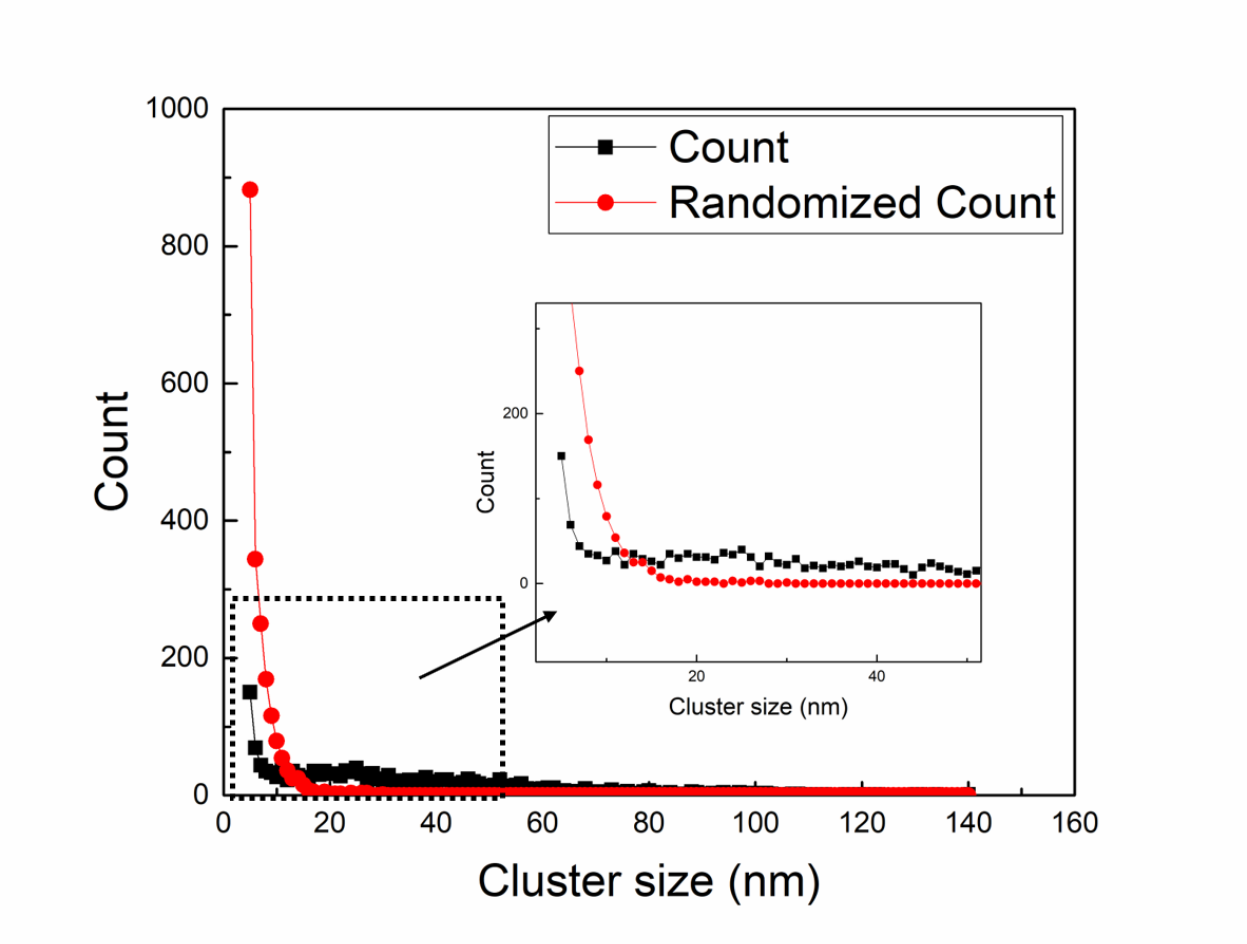

Figure 3-15. Plot of cluster size distribution to determine N_{min}.

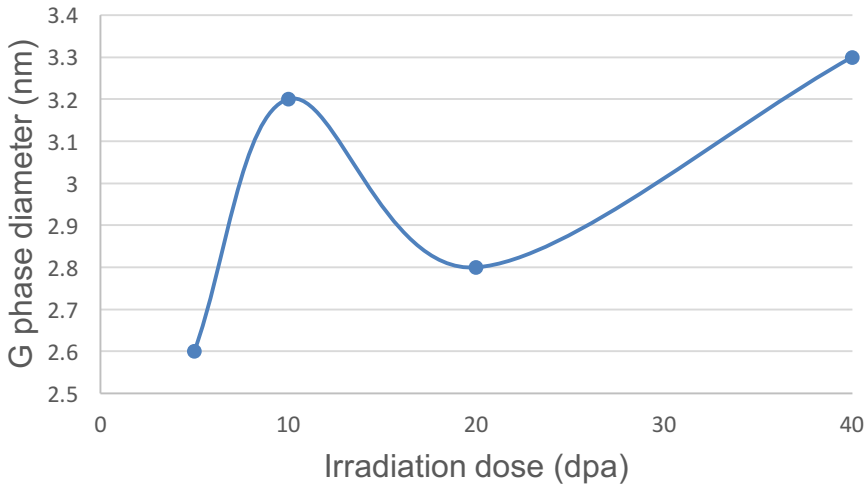

Figure 3-16. The evolution for mean size of G-phase precipitates versus the neutron dose.

3.3 TEM Characterization Result

3.3.1 Post Tensile Specimen characterization

The TEM characterization (Figure 3-17) of post-tensile specimens were performed using the STEM mode at different zone axes. The images of unaged condition were taken at 011 and 113 zone axes for austenite and ferrite, respectively. The images of both austenite and ferrite for aged 3000 hours condition were taken at 001 and 001 zone axes.

The TEM characterization shows a good agreement with the result from WAXS calculation. The dislocation density for unaged condition is $3.35\times10^{15}m^{-2}$ and $1.27\times10^{15}m^{-2}$ for austenite and ferrite, respectively. The dislocation density for aged 3000 hours condition is $1.23\times10^{15}m^{-2}$ and $1.38\times10^{15}m^{-2}$ for austenite and ferrite, respectively.

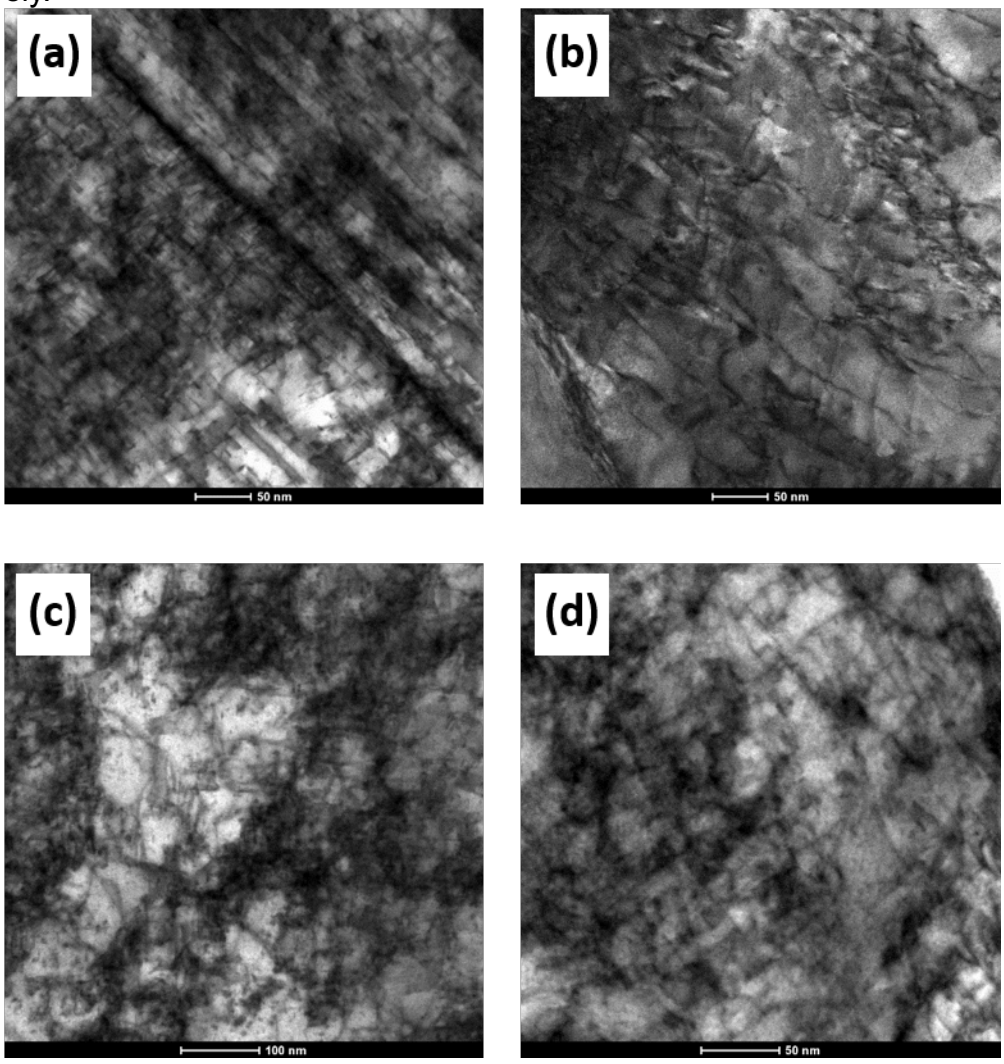

Figure 3-17. TEM characterization of DSS (a) austenite unaged (b) ferrite unaged (c) austenite aged 3000 hours (d) ferrite aged 3000 hours.

3.3.2 TEM Diffraction Pattern of Neutron Irradiated CASSs

The APT analysis shows that Mn-Ni-Si clusters form at the interdomain region of spinodal decomposition, which agrees with what Either A. MATEO or Timothy have observed. Nevertheless, whether these clusters already formed G-phase crystallographic structure remains in doubt. Therefore, it is necessary to use the diffraction pattern from TEM to determine whether these atoms are just clusters or already formed the G-phase structure. The diffraction pattern from TEM is shown in Figure 3-18**.** The diffraction pattern was taken at 110 zone axis of ferrite phase. As reported by several researchers [5, 46], the G phase always precipitates with $(1\ 1\ 0)_G$ // $(1\ 1\ 0)_\alpha$ orientation. Here, in our result, two sets of diffraction spots having the same orientation as the reference papers were observed. The diffraction pattern of 20 dpa condition was indexed and found having a very close lattice parameter (11.37 Å) as the normal G phase (11.2 Å). The minor difference could result from the neutron irradiation, as widely known that irradiation can alter the lattice parameter.

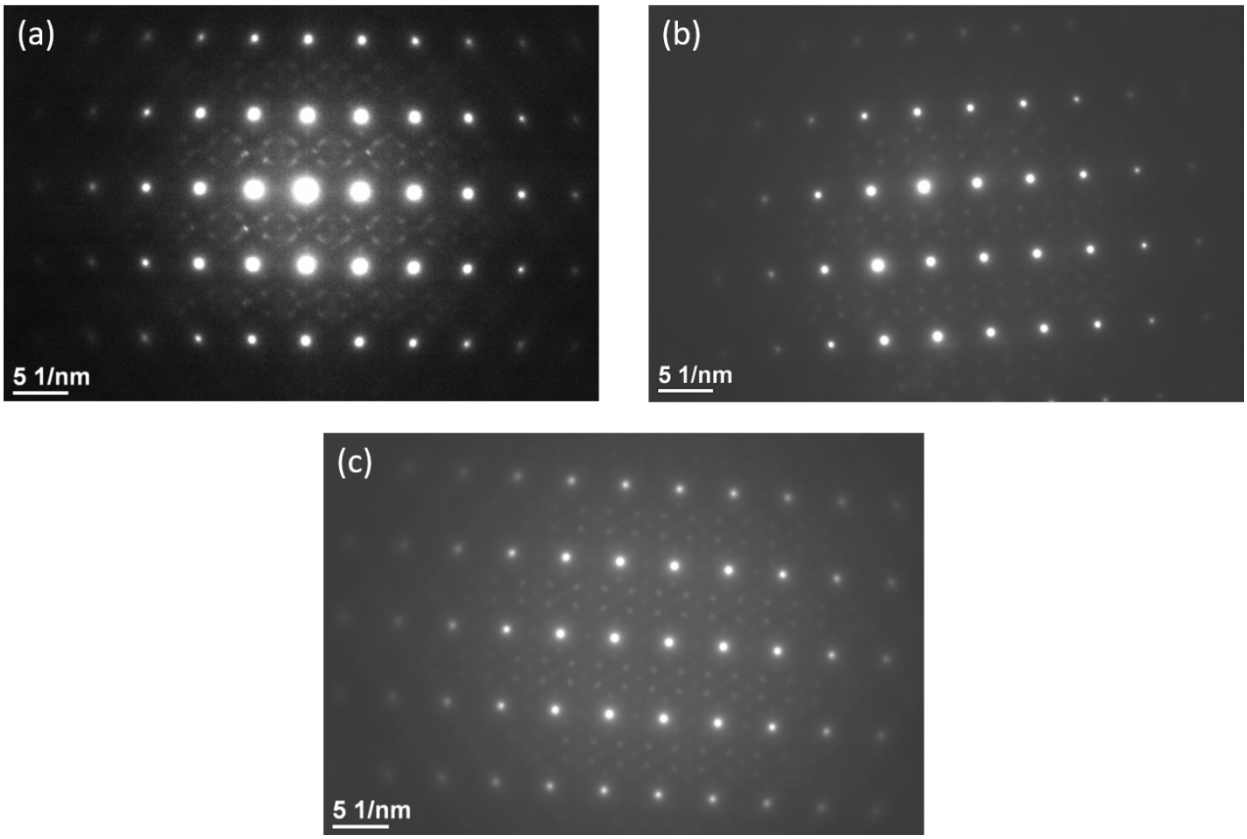

Figure 3-18. Diffraction pattern of CASSs irradiated to (a) 5 dpa, (b) 10 dpa and (c) 20 dpa.

3.4 EXAFS Characterization Result

The EXAFS raw data is conducted in Athena [47], which is an interactive graphical user interface (GUI) software for processing EXAFS data. It handles most of the common data acquired at the synchrotron beamline and prepare them for analysis. As fluorescence geometry was applied, it is necessary to convert the fluorescence

spectrum into transmission spectrum first using the calibrated parameters acquired from pure metal foil. This step is also known as self-absorption correction. Among different self-absorption correction algorithms, the Booth algorithm is applied as it is suitable for samples with finite thickness [48]. The corrected absorption spectrum is normalized, background subtracted and converted into EXAFS χ(k) spectrum. The output EXAFS χ(k) spectrum is then imported to Artemis, which is a GUI software that can perform Feff calculation to get the scattering path and conduct fitting for measured EXAFS χ(k) spectrum [49].

A total of four parameters that need to be fitted for each shell according to the EXAFS function [50, 51]:

$$\chi_i(k) \equiv \frac{(N_i S_0^2) F_{eff_i}(k)}{kR_i^2} \sin[2kR_i + \varphi_i(k)] e^{-2\sigma_i^2 k^2} e^{\frac{-2(R_{oi}+\Delta R_i)}{\lambda(k)}} \quad (3\text{-}1)$$

they are amplitude reduction factor S_0, disorder term σ, wave vector k and atomic distance change ΔR.

Since k can be calculated from ΔE which is relative to the absorption energy of the central atom using equation:

$$k^2 = \frac{2m_e(E - E_0 + \Delta E_0)}{\hbar} \quad (3\text{-}1)$$

E is the energy of incident X-ray, E_0 is absorption edge energy and ΔE_0 is change in absorption edge energy in measured spectrum. As ΔE_0 is only dependent on the absorbion edge, it is the same for all the scattering path within the same spectrum. Therefore, in real fitting, only one ΔE_0 is fitted instead of fitting multiple k for each shell, individually. However, for S_0, ΔR and σ, they are different for different shells and need to be fitted within each shell separately. Besides, the amplitude reduction factor S_0 is always fitted together with the nominal coordination number for each shell N_i, and their combination gives the actual coordination number for the shell.

As CASSs have duplex structure, scattering path from both structures need to be included in the EXAFS fitting, therefore, a large number of scattering paths are involved in the fitting. With each scattering path has three variables to fit, the total fitting variables can easily exceed the max allowable fitting variables. Besides, as there are too many variables, if they are not constrained correctly, it is likely to get a mathematically optimal results instead of a physically reliable result. Therefore, correlation between each scattering path is necessary for accurate EXAFS fitting.

In this project, as our sample is crystalline, the scattering path should follow a geometric relationship as determined by crystal structure. Hence, the correlation for ΔR between each scattering paths can be decided by crystal structure geometry. Besides, many attempts are needed to find the correlation for coordination number between different scattering paths.

3.5 FEM Modelling Result

3.5.1 Material Property Acquistion

For the input parameters for bulk 2D dogbone modelling, the elastic modulus, yield strength and Poisson's ratio were referenced from Samuel's paper, in which a various of

CASS with similar composition to ours were tensile tested [52]. The elastic modulus for ferrite and austenit phase were acquired from reference paper [53]. The mechanical properties for both ferrite and austenite were acquired from the in-situ Wide Angle X-ray (WAXS) tensile test. According to [29] and the plot in Figure 3-5 and Figure 3-6, it is determined that austenite phase yields at around 210 MPa no matter the specimen is unged or aged for different hours while ferrite phase yields at around 315 MPa, 388 MPa, 436.5 MPa and 453 MPa for unaged, aged 400 hours, aged 1000 hours, aged 3000 hours, respectively.
The yield strength is not enough for Abaqus to perform FEM modelling, the plastic stress and plastic strain is also needed. In this project, the principle stress after yield point is calculated and used as plastic stress for both ferrite and austenite phase with the following equation:

$$\sigma_{11} = \frac{E}{1+\nu}\varepsilon_{11} + \frac{\nu E}{(1+\nu)(1-2\nu)}(\varepsilon_{11} + \varepsilon_{22} + \varepsilon_{33}) \quad (2\text{-}2)$$

ε_{11} and ε_{22} is the weight average lattice strains at axial and transverse direction as discussed in in section 3.1.3, E is elastic modulus, ν is Poisson ratio and ε_{33} is assumed to be the same as ε_{22}. As for the plastic strain, by definitation, it is the true strain minus the strain at yield point. According to the EBSD investigation from Samuel [53], the extent of plastic deformation is similar between and ferrite and austenite, therefore, the strain of ferrite and asutenite can be set to be equivalent to the bulk strain. To here, all the input parameters that are needed for the simulation can either be acquired or calculated from the existing data.

3.5.2 Validation of In-situ WAXS Tensile Test

The true stress-true strain curve for both simulation and experiment results for unaged, aged 1000 hours and aged 3000 hours CASS are shown in Figure 3-19 to Figure 3-12, respectively.

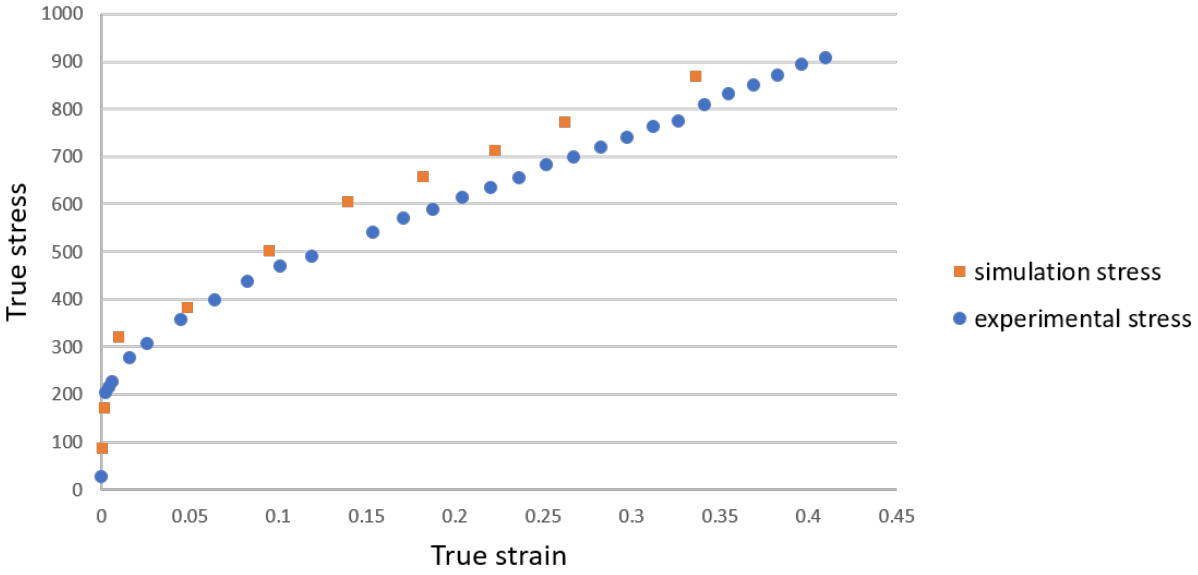

Figure 3-19. Simulated and experimental true stress-true strain curve for unaged CASS.

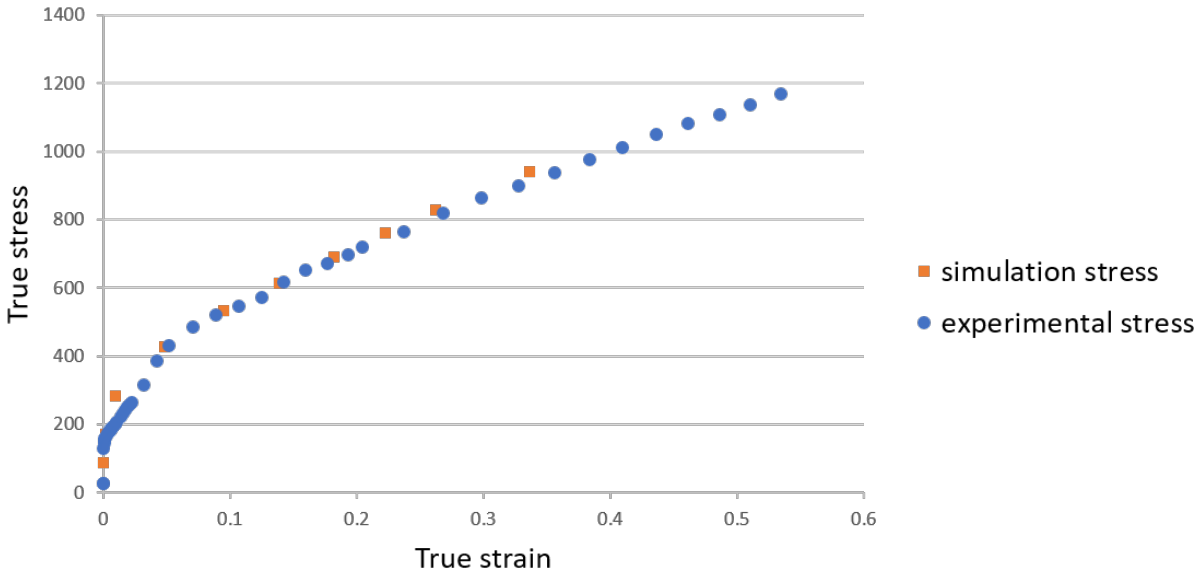

Figure 3-20. Simulated and experimental true stress-true strain curve for aged 1000 hours CASS.

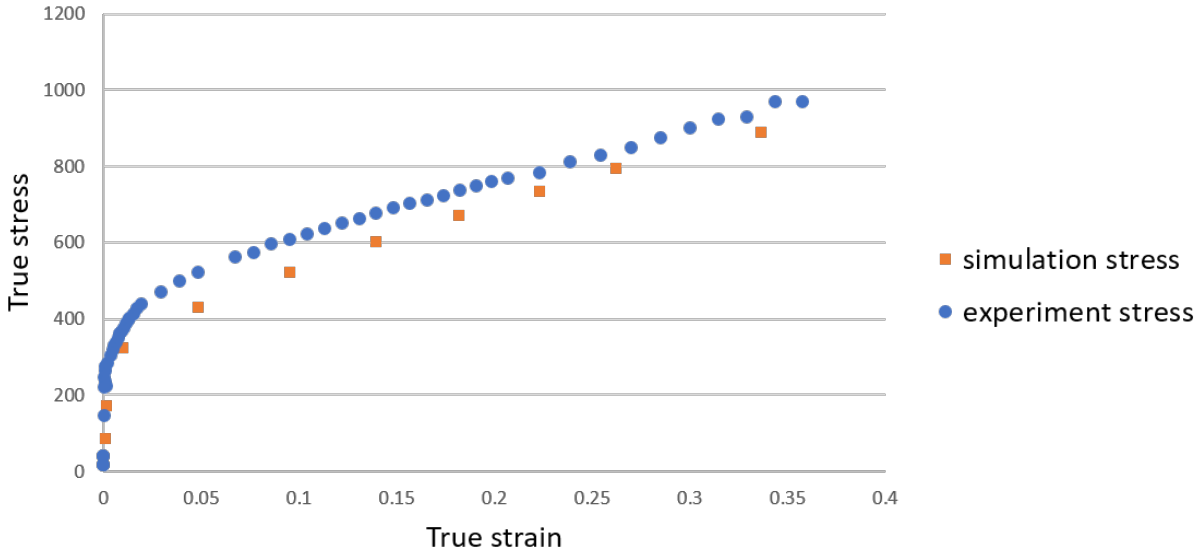

Figure 3-21. Simulated and experimental true stress-true strain curve for aged 3000 hours CASS.

3.5.2 2D Stress/Strain Distribution

As the material property acquired from in-situ WAXS tensile test data analysis has been validated from the tensile curve simulation. It can be applied in the 2D stress/strain distribution analysis. with input parameter exactly the same as previous section, the 2D von Mises stress and the in-plane

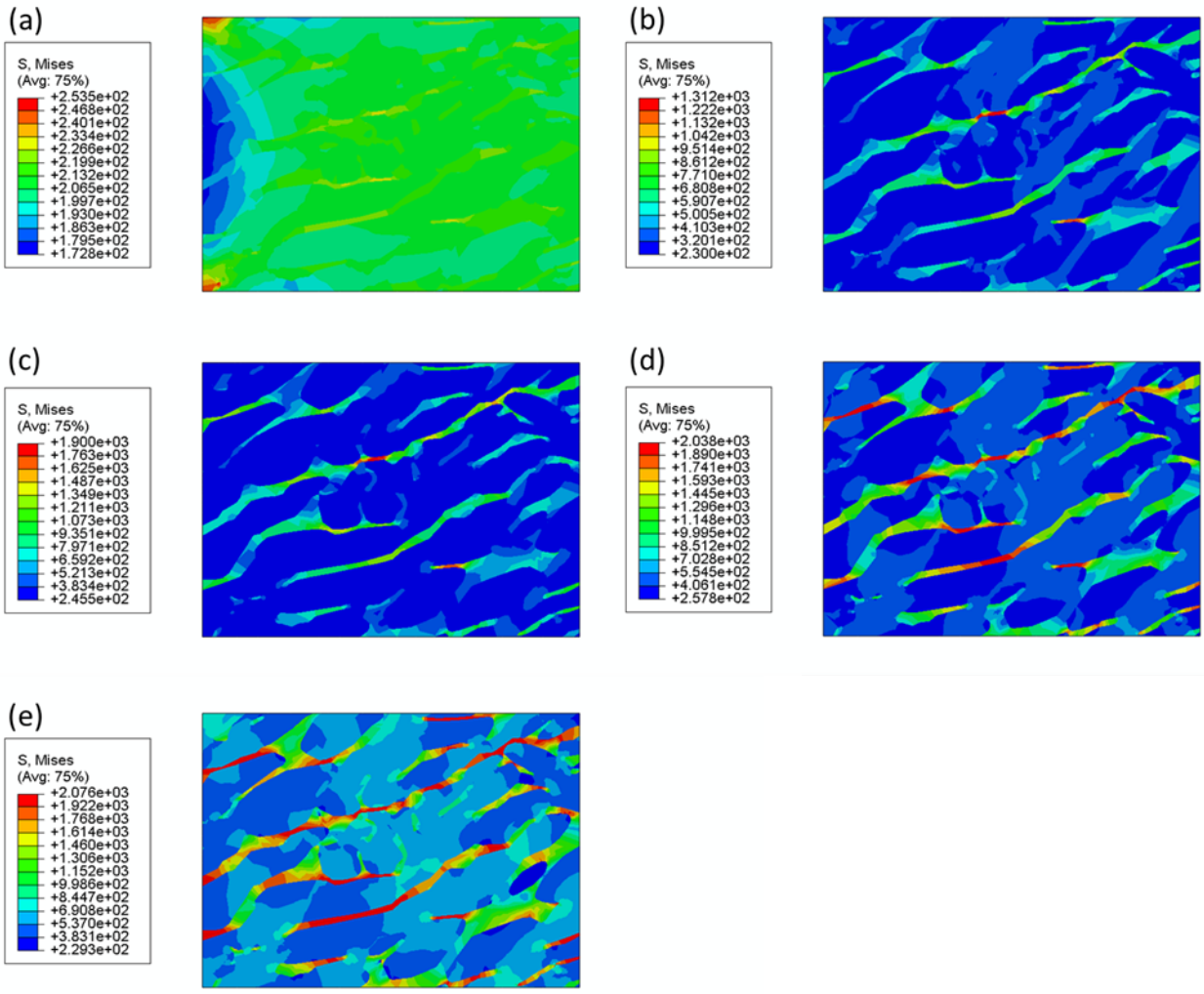

Figure 3-22. The von Mises stress distribution for both ferrite and austenite phase for duplex stainless steel aged 3000 hours with 0.1%, 1%, 2%, 5% and 10% strain, respectively.

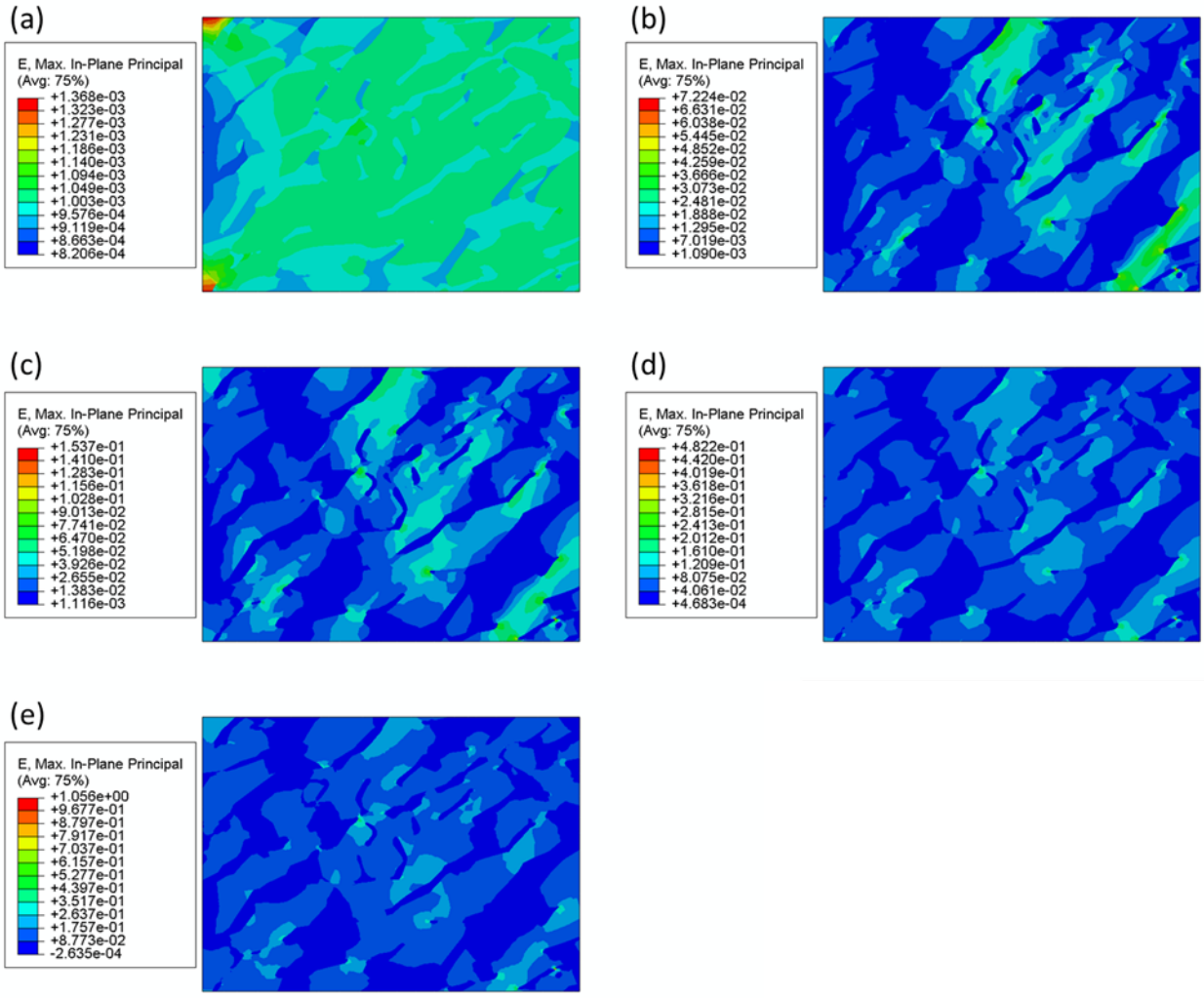

Figure 3-23. The in-plane principal strain distribution for both ferrite and austenite phase for duplex stainless steel aged 3000 hours with 0.1%, 1%, 2%, 5% and 10% strain, respectively.

DISCUSSION

4.1 Thermal Aging Effect on Mechanical Behavior of CASSs

4.1.1 Thermal Aging Effect on Ultimate Tensile Strength and Strain Hardening Rate

Based on the two in-situ WAXS tensile test, it is obviously that thermal aging has hardening effect on the CASSs. During the first experiment, thermal aging 1000 hours has increased the UTS around 55 MPa. On the contrary, when thermal aging time increases from 1000 to 3000 hours, instead of keep increasing, the UTS decreases. The strain hardening rate shows a similar trend. Figure 3-1 (c) clearly shows that the strain hardening rate has a big increment after aged 1000 hours and then decreases slightly from aging 1000 hours to 3000 hours.

For the second in-situ WAXS tensile test, although it is not a standard tensile test, it can still elucidiate some qualitative information about the mechanical property change due to thermal aging. Generally, the thermal aging increases the tensile strength while decreases the ductility, however, some exception exists. The aged 1000 hours condition shows a higher UTS than aged 3000 hours condition, which is consistent with our first experiment's result. Besides, although the aged 400 hours condition shows a higher strength than unaged condition at the same strain, it fails at a very early stage, therefore, the final UTS is lower than unaged condition instead. Since we only performed one tensile test on the aged 400 hours condition because of the limitation of the instrumental time, it is highly suspected that the failure at such an early stage is due to some defects from the manufacture.

4.1.2 Yield Strength of Ferrite and Austenite

Yield strength (YS) is defined to identify the stress at which plastic deformation begins. As YS represents the upper limit to forces that can be applied without producing permanent deformation, it is often used to determine the maximum allowable load in a mechanical component in structural engineering. For structural material like CASSs used in nuclear reactors, yield strength is even more important, as failure in mechanical componenet in nuclear reactors may cause a catastrophe.

As previously mentioned, ferrite within CASSs undergos phase transformation: spinodal decomposition and G-phase precipitation. How the microstructural evolution of ferrite will affect the mechanical property really a big concern, as it can directly determine the lifetime of a nuclear power plant.

As described in section 2.1, in- situ WAXS tensile test was performed on the thermally aged CASSs and the result is listed in section 3-1. From the plot in Figure 3-5, Figure 3-6 and Table 3-2, it is evident that austenite phase yields at around 210 MPa no matter the specimen is not aged or aged for different hours. On the contrary, ferrite phase yields at around 315 MPa, 388 MPa, 436.5 MPa and 453 Mpa for unaged, aged 400 hours, aged 1000 hours, aged 3000 hours, respectively. The YS evolution of ferrite phase relative to thermal aging hours is plotted in Figure 4-1 (a). The YS of ferrite increases drastically after thermal aging up to 1000 hours, in contrast, comparing with the dramatic increase between unaged to aged 1000 hours, the YS of ferrite only

increases a little from aged 1000 hours to 3000 hours. It seems that the thermal aging effect is starting to saturate at 1000 hours.

4.1.3 Thermal Aging Effect on Fractrure Behavior of CASSs

As discussed in section 4.1.1, UTS increases as thermal aging time up to 1000 hours. However, as discussed in section 4.1.2, the YS of ferrite is though slower but still increasing beyond 1000 hours. The result seems contradictory to each other, in fact, it can be explained by the SEM images (Figure 4-1 (b)) taken while preparing the TEM lamella for post-tensile specimen characterization. It shows the appearance of pores at phase boundary in the aged 3000 hours specimen while no pores were observed in aged 1000 hours specimen. Therefore, it can be concluded that although the further thermal aging hours beyond 1000 hours does not increase the YS of ferrite phase too much, it made the phase boundary more vulnerable to break. Therefore, the ageing 3000 hours shows a lower UTS and lower strain hardening rate compared with ageing 1000 hours. It has been reported that several precipitation forms at the ferrite-austenite phase boundary during thermal aging and these precipitations may undermine the strength of phase boundary, making it an easy path for crack formation and propagation [54-58]. However, most of these precipitates need high temperature (above 500°C) to form. Carbide is one of the most common precipitates that forms at phase boundary at a relatively low temperature. For some CASS with higher carbon concentration, carbide can form at phase boundary after aging at 400°C for 10000 hours [58]. However, based on the X-ray spectrum, no peaks from carbide phase were observed. Besides, as plotted by T. S. Byun and J. T. Busby [3], for low carbon CASSs, it may take up to 10000 hours for carbide formation. Therefore, the undermine of phase boundary is not likely to caused by carbide formation, it is more likely to be induced by elemental segregation before carbide formation. However, further investigation is still needed to prove this assumption.

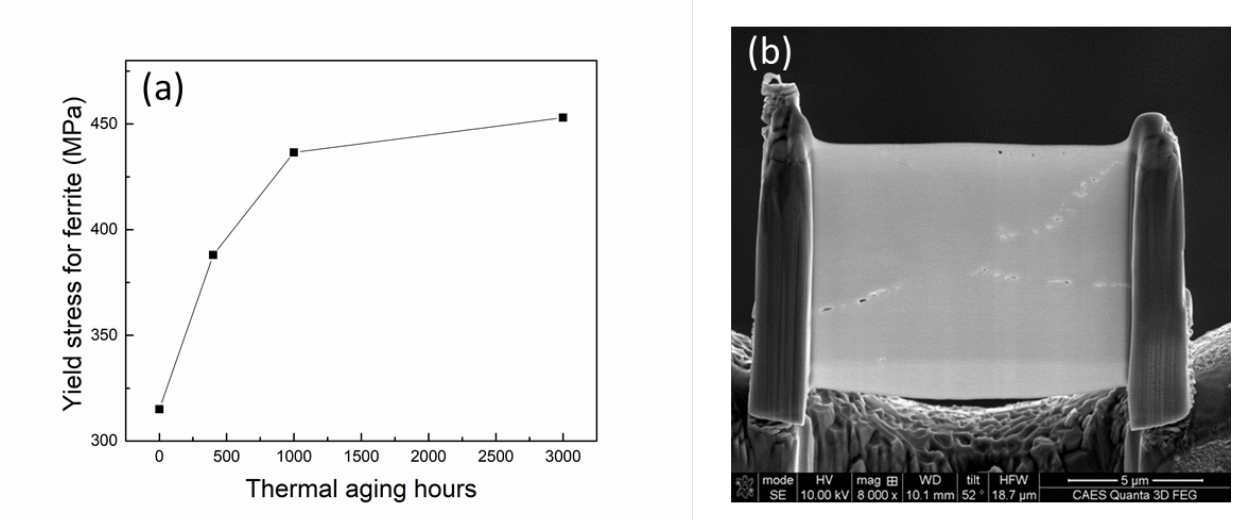

Figure 4-1. (a) Yield strength evolution of ferrite phase as thermal hours (b) TEM lamella cut at the necking zone of the DSS that is aged 3000 hours.

4.2 Plastic Deformation of Austenite and Ferrite Phase

As shown in Figure 3-7 (b), the true stress is plotted versus square root of dislocation density $\sqrt{\rho}$ for austenite phase. The good linearity shows the dominance of dislocation glide in plastic deformation in austenite Besides, dislocation evolution for both ferrite and austenite are plotted in Figure 3-7 (a) and Figure 3-8. The dislocation density for austenite phase shows a linear increase as strain increases w./wo. thermal aging. The plots in Figure 3-7 suggest that plastic deformation behavior of austenite is not significantly altered by thermal aging. In contrast, dislocation density plot for ferrite phase in Figure 3-8 shows although the ferrite phase has the similar dislocation density when it is close to failure for both unaged and aged condition, the dislocation density of aged ferrite phase propagated much faster at the early plastic deformation stage comparing with the unaged condition. The higher dislocation density at early defomation stage is likely result from the microstructural evolution within ferrite. Both periodic strain field produced by the sinusoidal composition modulations resulting from spinodal decomposition or G-phase precipitates work as obstacle that inhibit dislocation movement. As the present dislocation is pinned, new dislocation is generated rapidly with deformation continuing.

To make sure the WAXS result is accurately interpreted, dislocation density calculated from WAXS is compared with the dislocation density counted from TEM characterization. The result shows a good consistent with each other (within the same order of magnitude), suggesting in-situ WAX tensile test is a great tool to investigate the dislocation evolution inside the material. Although little discrepancy still exists, mostly because of three reasons: first, large amount of dislocation exists inside the post-tensile specimens, making it too hard to count very precisely; second, the TEM is focusing on a relative small area and the dislocation distribution may not be uniform; third, the calculation of dislocation through X-ray went through multiple data analysis process, uncertainty may be introduced in each step especially for ferrite phase, as its peak intensity is much weaker than austenite phase.

4.3 Neutron Irradiation Effect on CASSs

4.3.1 Dose Rate Effect of Spinodal Decomposition

The Cr atomic map as well as the frequency distribution of Cr indicate a moderate spinodal decomposition below 20 dpa, which seems contradictory to our previous paper where 0.08 dpa has already induced a significant spinodal decomposition. In fact, this phenomenon is result from the different dose rate. For 0.08 dap irradiation, the dose rate is 5×10^{-9} dap/s, while dose rate here for 3 dpa and 5-40 dpa are 5×10^{-8} dap/s and 7×10^{-7} dap/s, respectively. Previous research has proved that the spinodal decomposition is more affected by dose rate rather than the dose [59, 60]. The fundamental reason that irradiation can accelerate the spinodal decomposition is relied on the Radiation Enhanced Diffusion (RED). As well known, the radiation can create the vacancy and self-interstitial atom (SIA). Their generation and recombination are largely determined by the dose rate. At high dose rate, recombination will be significantly enhanced and thus the spinodal decomposition will be mediated. Besides,

the ballistic mixing is another factor that cannot be overlooked especially in ion irradiation. During irradiation, atomic recoils will lead to the ejection of Cr cluster solutes back into the matrix and Fe matrix atoms into the cluster. For low dose rate, a relative longer irradiation period still allows the back diffused Cr and Fe atoms to reach a near thermodynamic equilibrium composition. However, when the dose rate is high, the irradiation time is not enough for full diffusional recovery, a non- equilibrium state will be retained giving a lower Cr contents than thermodynamic equilibrium condition. This can also be the reason that K. Fujii found the irradiation decrease the spinodal decomposition [61]. Besides, they were using the Fe^{3+} for irradiation, which may further add the uncertainty in the spinodal decomposition result.

4.3.2 Spinodal Decomposition Due to High Dose Irradiation

Comparing 5, 10, 20 and 40 dpa, it is found that the wavelength and magnitude is relatively stable at 5 to 10 dpa, similar to the result reported by Elaina [59]. It seems the spinodal decomposition has saturated at 5 dpa under this dose rate. However, between 10 to 20 dpa, a dramatic increase in magnitude is observed. Considering the stable magnitude and wavelength at 5 to 10 dpa and the Elaina's result, the magnitude boost of spinodal decomposition between 10 and 20 dpa is not likely to result from irradiation dose. The increment is likely to from the G-phase cluster as these two microstructural evolutions are always correlated. As a matter of fact, the sudden increment corresponds well with the chemical composition change of G-phase clusters where the concentration of Fe and Cr decrease significantly. Therefore, the increment of magnitude of spinodal decomposition can be explained. The compositional change of G-phase cluster leads to the ejecting of matrix atoms (Fe and Cr). The excluded Fe and Cr further decomposition to Fe and Cr rich region and further enhance the spinodal decomposition.

4.3.3 Temperature Dose Rate and Irradiation Dose Effect on G-phase Size

G-phase precipitation has been reported in both thermally aged and neutron irradiated ferrite. For both conditions, temperature is a key factor that plays a significant role. As there are more publications about the thermal aging effect, the temperature effect during thermal aging can be concluded. Y. Matsukawa et al [4] found in the ferrite/austenite duplex stainless steel G-phase variant aged at 400℃for 1000 and 2000 hours has mean size around 2.03 and 2.2 nm, respectively. Chen et al [62] found in Fe20Cr9Ni cast duplex stainless steel, the mean size of G phase aged at 475℃for 1000 and 2000 hours can be 13.45 and 21.54 nm, respectively. Although these two publications are not using the material with the exact same chemical composition. The results satisfy the general knowledge that higher temperature enhance the thermal aging as it can enhance the diffusion of all atoms. However, for neutron irradiation, the situation is complicated. The temperature, neutron irradiation dose and dose rate can all affect the size of G-phase. Among three elements, the temperature is most complicated. On one side, the higher temperature during irradiation, the diffusion of atoms will be improved. On the other side, the higher temperature will improve the vacancy or

interstitial atom recombination at sinks. Recently, Ce Zheng [63] investigated the effect of temperature during neutron irradiation on HT9 ferritic/martensitic steel and conclude that the higher temperature during neutron irradiation will leads to a larger G phase precipitates.

For irradiation dose effect, comparing our result: the 3 dpa condition with dose rate of 5×10^{-8} dap/s at around 307℃has a G-phase cluster size around 2.12 nm and 5 dpa condition with dose rate of 7×10^{-7} dap/s at around 320℃has 2.78 nm. The minor temperature difference should have very limited effect, the irradiation dose should be the dominate effect that result in the size of G-phase cluster.

For dose rate effect, Siwei Chen [39] investigated the low fluence neutron irradiation (~0.007 dpa) effect of ferrite in cast austenitic stainless steels. A relative low temperature ~ 290℃with low dose rate 7.9×10^{-9} dpa/s leads to Mn-Ni-Si cluster with diameter around 2.2 nm. Considering the size of G-phase for our 3 dpa condition is only 2.03 nm, Chen's condition has lower dose rate, lower temperature and lower irradiation dose. As low temperature and low irradiation dose should induce smaller precipitates size, their large precipitate size should be result from the low dose rate.

4.3.4 G-phase Formation Due to Neutron Irradiation

The TEM characterization at 110 zone axis of ferrite has shown that the Mn-Ni-Si clusters have formed a G-phase like structure at 5 dpa. As compared with Chen et al [62] and Y. Matsukawa et al [4], the invisibility of (400) diffraction spot indicates that the precipitation has compositional variation with the normal G-phase. As suggested by Y. Matsukawa [4] , they are referred as G-phase variant. As we can see in Error! Reference source not found., the size of G-phase variant increases from 2.6 nm to 3.2 nm while the irradiation dose increasing from 5 to 10 dpa. In contrast, as irradiation dose increases from 10 to 20 dpa, the size of G-phase variant decreases from 3.2 nm to 2.8 nm. The further irradiation to 40 dpa increases the size of G-phase variant again to 3.3 nm. The composition change is following the similar trend with the size evolution of G-phase variant: the concentration of matrix atoms (Fe, Cr) decreases from 5 to 10 dpa while the Ni is increasing; the concentration of Fe, Cr increases from 10 to 40 dpa while the Ni is decreasing. It is reasonable to assume that the size increment is not simply depend on the irradiation dose but also because of the chemical composition change. A reasonable assumption is that at 5 dpa, the G-phase variant with small size has formed. During the irradiation dose increasing from 5-10 dpa, the neutron irradiation induces the coarsening of G-phase variant. Matrix atoms are also included to form G-phase variant, thus the concentration of Ni, Si are decreasing. However, at 10 dpa, the G-phase variant reaches a critical size and composition adjustment of G-phase variant starts. The ejection of matrix atoms leads to the size reduction of G-phase variant. Once the matrix atoms have been excluded from the G-phase variant, the further irradiation continues the coarsening effect, thus the size of G-phase variant continues to grow. This assumption can explain the phenomenon we observed reasonably. Besides, the reason we keep calling it the G-phase variant is because that the concentration of Mn in G-phase variant is really low comparing with the normal G-phase, which means the compositional adjustment of G-phase variant is still ongoing.

As explained by Timothy [42], the G phase formation is because of the spinodal decomposition leads to Fe rich region and Cr rich region and Ni has very limited solubility in Cr. Therefore, the Ni has phase separation first. Then, as Mn and Si has greater miscibility in Ni than in Cr, they tend to diffuse into Ni and form cluster and later form G-phase. This is under the thermal aging condition. For neutron irradiate condition, the diffusion is mostly happened through vacancy-interstitial diffusion, the atoms with smaller size has higher mobility than large atoms. Therefore, Si has a much higher mobility than Ni because of the atomic radius. Though the Ni atoms should form cluster prior to Si thermodynamically, after considering the diffusion effect, they form cluster almost at the same time. For Mn, it forms cluster after Ni thermodynamically and its mobility is lower than Ni kinetically due to atomic radius, thus, it forms cluster much slower than Ni and Si. The Pearson correlation coefficient plot in Error! Reference source not found. **Error! Reference source not found.**proves that the Ni and Si has a very close Pearson correlation coefficient at different dose and the phase separation has completed at 5 dpa, while the Pearson correlation coefficient for Mn is still increasing indicating that the phase separation of Mn is still ongoing.

4.4 Compare Effect Between Thermal Aging and Neutron Irradiation

Previous low dose neutron irradiation experiment to 0.007 and 0.08 dpa suggests that thermal aging before irradiation induce a more enhanced spinodal decomposition and G-phase precipitation [39, 43]. Here, for our result, comparing the 3 dpa condition w./wo. thermal aging, the wavelength and magnitude of spinodal decomposition is similar indicating the neutron irradiation has already dominated the spinodal decomposition at this dose. For the G-phase clusters, the chemical composition, number density, mean size as well as the volume fraction are all very close for 3 dpa condition w./wo. thermal aging showing the G-phase clusters are also dominated by neutron irradiation at such dose. Overall, at neutron dose around 3 dpa, the primary microstructure of ferrite is due to the neutron irradiation where thermal aging only has a minor effect.

4.5 Correlation between Mechanical Property and Microstructure of Neutron irradiated CASSs

As discussed in previous chapter, neutron irradiation can induce spinodal decomposition and G-phase precipitation. Both microstructural evolutions have significant effect on material's mechanical property. Spinodal decomposition leads to ferrite phase decompose into Fe rich α phase and Cr rich α' phase. The sinusoidal composition modulations induce a periodic strain, which will affect the movement of dislocations. For G-phase precipitation, plenty of publications have reported it appears as spherical particles, thus, its effect on the dislocation movement can be addressed with precipitation hardening models. As the yield strength is closely relevant to movement of dislocation, in the following sections, the yield strength increment due to spinodal decomposition and G-phase precipitation will be discussed in detail.

4.5.1 Irradiation Hardening Due to Spinodal decomposition

Previous researchers have proposed different hardening models to explain the spinodal decomposition hardening. According to a review paper by Wagner [64], two theories of spinodal decomposition hardening seems applicable at that time, after a large quantity of test over a long time period. The first one is proposed by Cahn [65], whose model suggests that the spinodal decomposition hardening is linearly dependent on the wavelength of spinodal decomposition. The second model proposed by Kato [66], however, suggests that spinodal decomposition hardening is independent of the wavelength. Later, Ardell considered the diffuse character of the spinodal decomposition as the fact that spinodal decomposition is not made of perfect sinusoidal concentration waves and further improved Cahn's model [67]. In this project, the Ardell's model is utilized to analyze the spinodal decomposition hardening.
For Ardell's model, the critical resolved shear stress necessary to initiate dislocation slip due to spinodal decomposition is given by the following equation:

$$\tau_{CRSS}^{\alpha/\alpha'} = \beta(\Delta C_{Cr})\delta Y)^{\frac{5}{3}}(\frac{b\lambda}{\Gamma})^{\frac{2}{3}} \quad (4\text{-}1)$$

β is the obstacle strength while ΔC_{Cr} and λ are the amplitude and the wavelength of the spinodal decomposition. $\delta = \frac{a_{\alpha'} - a_{\alpha}}{a_{\alpha'}}$ is lattice mismatch between α and α' ($a_{\alpha'} = 0.2882$ nm, $a_{\alpha'} = 0.2866$ nm, respectively). Y is equal to $Y = \frac{(C_{11}-2C_{12})\,(C_{11}-C_{12})}{C_{11}}$ calculated from the pure iron elastic constants and the elastic constants are acquired from a reference paper . b is the Burgers vector of edge dislocations in BCC while Γ is the line tension of the dislocation. The expression $\Gamma = \frac{1}{2}\,\mu b^2$ is used to estimate Γ with μ, and the shear modulus is assumed to be 77 GPa, as used in reference paper [39]. As in BCC structure, the Burges vector of edge dislocation is always ½ <111>, thus b is calculated to be 0.248 nm and Γ is calculated to be 2.55×10^{-9} N.

Then the ferrite yield strength strength due to spinodal decomposition is calculated from the following equation:

$$\Delta\sigma_y = \mathrm{M}\cdot\tau_{CRSS} \quad (4\text{-}2)$$

M is the Taylor factor, which is 3.06 for both BCC and FCC steel.

4.5.2 G-phase Hardening

The G-phase appears as spherical particles. Precipitation hardening models have thus been used and G-phase precipitates were assumed to be shearable obstacles distributed evenly within the ferrite phase. The change in yield strength ($\Delta\sigma_y$) induced by solute clusters is givenequation 4-3:

$$\Delta\sigma_y = M\alpha_G\mu b\sqrt{N_G d_G} \quad (4\text{-}3)$$

M is the Taylor factor, α_G is the strength of G phase particles while N_G and d_G are number density and diameter of the precipitates, respectively.

4.5.4 Convertion Between Hardness and Yield Strength

The correlation equation between nanoindentation hardness with Berkovich indenter and Vickers hardness is acquired from Nanoindentation textbook [68], which is:

$$\Delta H_V = 0.094495\Delta H \tag{4-4}$$

Where ΔH_V is Vickers hardness in kgf/mm^2 and ΔH is Berkovich hardness in MPa. The equation has been applied by other researchers, giving them optimal results [69, 70].

For ferritic steels, the correlation factor between the change in yield stress and the change in Vickers hardness is 3.06 [71]:

$$\Delta\sigma_y = 3.06\Delta H_V \tag{4-5}$$

Combining equation 4-1 to 4-5, the change in the nanoindentation hardness due to G-phase precipitation can be deduced as:

$$\Delta H_G = \frac{\alpha\mu b\sqrt{Nd}}{0.094495} \tag{4-6}$$

And the nanoindentation hardness due to spinodal decomposition is calculated as:

$$\Delta H_{SD} = \frac{\beta(\Delta C_{Cr})\delta Y)^{\frac{5}{3}}(\frac{b\lambda}{\Gamma})^{\frac{2}{3}}}{0.094495} \tag{4-7}$$

4.5.3 Combined Hardening Effect Due to Spinodal Decomposition and G-phase Precipitation

To fully quantifiy the total critical shear stress of the ferrite after neutron irradiation, hardening due to both spinodal decomposition and G-phase precipitation need to be added together. As a first guess, it is reasonable to add hardening part due to spinodal decomposition and G-phase precipitation linearly. However, Sylvain performed dislocation dynamics simulations to characterize the individual and the superposed contributions of two major mechanisms of crystal plasticity and found that a quadratic rule of mixtures gives a better result [72]. Therefore, here the total hardening is calculated using both linear and quadraticrule of superposition.

The calculated and experimental nanoindentation hardness as well as the characteristic parameters of spinodal decomposition and G-phase precipitation of neutron irradiated CASS to 20 and 40 dpa are listed in Table 4-1. As can be seen, the calculated hardness is pretty close to the experimental hardness. It needs to be pointed out that the irradiation induced defects are not included in the calculation. However, as ferrite is more resistant to neutron irradiation, the density of dislocation loop is much less than it is within austenite phase by one or two order of magnitude. Chen investigated CF-3 CASS that is neutron irradiated to 24.5 and 45 dpa, the dislocation loop density and size result is shown in Table 4-2 [73]. Therefore, the dislocation loop density of ferrite phase is assumed to be about $10^{21}\ m^{-3}$. According to Tan's calculation

[74], obstacle strength for dislocation loop at such size is around 0.6. Hence, the nanoindentation hardening due to dislocation loop for ferrite phase can be roughly estimated to be around 0.38 GPa and 0.42 GPa. Consider the minor hardening effect from neutron irradiation to ferrite phase, our calculation is very close to the experimental result for 20 dpa condition. For 40 dpa, the experimental result for nanoindentation is lower than 20 dpa, which is unusual. A possible explanation is the grain orientation effect [75, 76]. CASSs has hugh grain size and the nearby grains have a similar orientation. Therefore, during the nanoindentation experiment, if different indents are not conducted at a distance that is far enough, the result may affected by grain orientation.

Table 4-1. Characteristic parameters of spinodal decomposition and G-phase precipitation obtained by APT for ferrite phase of irradiated CASSs together with their experimental and calculated nanoindentation hardness using both linear superimpose and square superimpose. The as-cast CASS is also listed for comparison.

		Spinodal decomposition		G-phase precipitation		Experimental hardness (GPa)	Calculated hardenss (GPa)	
Aging condition	Irradiation	Wavelength (nm)	Magnitude (%)	Size (nm)	Number density (m^{-3})		Linear	Square
Unaged	Unirr	N/A	N/A	N/A	N/A	3.63±0.037	N/A	
Unaged	20 dpa	14.93	29.66	3.02 ± 0.3	$(7.16 \pm 0.73)\times 10^{23}$	6.74±0.021	6.08	5.95
Unaged	40 dpa	16.47	32.74	3.52 ± 0.06	$(4.18 \pm 0.31) \times 10^{23}$	6.07±0.078	6.29	6.26

Table 4-2. dislocation loop quantification of austenite phase for highly irradiated CF-3.

Material	Dose (dpa)	Density ($\times 10^{22} m^{-3}$)	Size (nm)
CF-3	24.5	2.8	8.5
	45	6.2	10.1

Overall, quantify the hardening effect from both spinodal decomposition and G-phase precipitation is a plausible method, and this method has been proved to work well on thermally aged CASSs. The work from this project shows that it is promising for neutron irradiated CASSs, however, the calculation is still too rough. In the future, more data from different aspects are needed to build up a more accurate equation. First, the density and size of dislocation loop need to be measured directly from irradiated ferrite. Second, the empirical relationship between yield strength and Vickers hardness needs to be investigated more carefully for irradiated speicmens, as currently the relationship is acquired from a non-rad ferritic steel. Third, the current correlation between nanoindentation hardness and Vickers hadness is based on a theoretical calculation, and it can be further modified by performing indentation on same standard materials with same force.

REFERENCE

1. Callister, W. and D. Rethwisch, *Materials science and engineering, vol. 5 New York.* NY: John Wiley & Sons, 2011.
2. Bramfitt, B.L., *Structure/Property relationships in irons and steels.* Materials Park, OH: ASM International, 1998., 1998: p. 153-173.
3. Byun, T. and J. Busby, *Light Water Reactor Sustainability: Cast Stainless Steel Aging Research Plan.* ORNL/LTR-2012/440 (www. energy. gov/sites/prod/files/CastStainlessSteelAgingResearchPlan_September2012. pdf), 2012.
4. Matsukawa, Y., et al., *The two-step nucleation of G-phase in ferrite.* Acta Materialia, 2016. **116**: p. 104-113.
5. Mateo, A., et al., *Characterization of the intermetallic G-phase in an AISI 329 duplex stainless steel.* Journal of Materials Science, 1997. **32**(17): p. 4533-4540.
6. Franke, P. and D. Neuschütz, *Binary Systems. Part 4: Binary Systems from Mn-Mo to Y-Zr· Mo-Ni: Datasheet from Landolt-Börnstein-Group IV Physical Chemistry· Volume 19B4: Binary Systems. Part 4: Binary Systems from Mn-Mo to Y-Zr*. 2006, Springer-Verlag Berlin Heidelberg.
7. Franke, P. and D. Neuschütz, *Thermodynamic Properties of Inorganic Materials: Binary Systems. Part 3: Elements and Binary Systems from Cs–K to Mg–Zr*. 2005, Springer-Verlag, Berlin.
8. Franke, P. and D. Neuschutz, *Landolt-bornstein–Group IV Physical Chemistry Vol 19B2. Binary Systems. Part 2: Elements and Binary Systems B-C to Cr-zr*. 2006, Springer Books.
9. Ponomareva, A.V., et al., *Effect of multicomponent alloying with Ni, Mn and Mo on phase stability of bcc Fe-Cr alloys.* Acta Materialia, 2018. **150**: p. 117-129.
10. DeHoff, R., *Thermodynamics in materials science*. 2006: CRC Press.
11. Michaud, W., et al., *Tensile-property characterization of thermally aged cast stainless steels*. 1994, Nuclear Regulatory Commission, Washington, DC (United States). Div. of ….
12. Byun, T.S., et al., *Thermal Aging Phenomena in Cast Duplex Stainless Steels.* Jom, 2015. **68**(2): p. 507-516.
13. Zinkle, S.J., *Microstructures and mechanical properties of irradiated metals and alloys*, in *Materials Issues for Generation IV Systems*. 2008, Springer. p. 227-244.
14. Zinkle, S., P. Maziasz, and R. Stoller, *Dose dependence of the microstructural evolution in neutron-irradiated austenitic stainless steel.* Journal of Nuclear materials, 1993. **206**(2-3): p. 266-286.
15. Maziasz, P., *Overview of microstructural evolution in neutron-irradiated austenitic stainless steels.* Journal of nuclear materials, 1993. **205**: p. 118-145.
16. Kenik, E.A. and J.T. Busby, *Radiation-induced degradation of stainless steel light water reactor internals.* Materials Science and Engineering: R: Reports, 2012. **73**(7-8): p. 67-83.
17. Chopra, O.K. and A.S. Rao, *A review of irradiation effects on LWR core internal materials – Neutron embrittlement.* Journal of Nuclear Materials, 2011. **412**(1): p. 195-208.

18. Lechtenberg, T., *Irradiation effects in ferritic steels.* Journal of nuclear materials, 1985. **133**: p. 149-155.
19. Busby, J.T., et al., *Materials degradation in light water reactors: life after 60.* ORNL Report, ORNL/TM-2008/170, 2008.
20. Zhang, X., et al., *In situ high-energy X-ray diffraction study of tensile deformation of neutron-irradiated polycrystalline Fe-9%Cr alloy.* Acta Materialia, 2017. **126**: p. 67-76.
21. Xu, C., et al., *In-situ high-energy X-ray characterization of neutron irradiated HT-UPS stainless steel under tensile deformation.* Acta Materialia, 2018. **156**: p. 330-341.
22. Wang, L., M. Li, and J. Almer, *Investigation of deformation and microstructural evolution in Grade 91 ferritic–martensitic steel by in situ high-energy X-rays.* Acta Materialia, 2014. **62**: p. 239-249.
23. Wang, L., M. Li, and J. Almer, *In situ characterization of Grade 92 steel during tensile deformation using concurrent high energy X-ray diffraction and small angle X-ray scattering.* Journal of Nuclear Materials, 2013. **440**(1-3): p. 81-90.
24. Miao, Y., et al., *On the microstructure and strengthening mechanism in oxide dispersion-strengthened 316 steel: A coordinated electron microscopy, atom probe tomography and in situ synchrotron tensile investigation.* Materials Science and Engineering: A, 2015. **639**: p. 585-596.
25. Liu, X., et al., *Investigation of thermal aging effects on the tensile properties of Alloy 617 by in-situ synchrotron wide-angle X-ray scattering.* Materials Science and Engineering: A, 2016. **651**: p. 55-62.
26. Li, M., et al., *Study of irradiated mod.9Cr–1Mo steel by synchrotron extended X-ray absorption fine structure.* Journal of Nuclear Materials, 2013. **441**(1-3): p. 674-680.
27. Degueldre, C., S. Conradson, and W. Hoffelner, *Characterisation of oxide dispersion-strengthened steel by extended X-ray absorption spectroscopy for its use under irradiation.* Computational Materials Science, 2005. **33**(1-3): p. 3-12.
28. Cammelli, S., et al., *Polydispersity and EXAFS simulations.* Journal of Physics: Conference Series, 2009. **190**.
29. Van Swygenhoven, H. and S. Van Petegem, *In-situ mechanical testing during X-ray diffraction.* Materials Characterization, 2013. **78**: p. 47-59.
30. ToMOTA, Y. and I. TAMURA, *Mechanical behavior of steels consisting of two ductile phases.* Transactions of the Iron and Steel Institute of Japan, 1982. **22**(9): p. 665-677.
31. Abràmoff, M.D., P.J. Magalhães, and S.J. Ram, *Image processing with ImageJ.* Biophotonics international, 2004. **11**(7): p. 36-42.
32. Mente, T. and T. Boellinghaus, *Mesoscale modeling of hydrogen-assisted cracking in duplex stainless steels.* Welding in the World, 2013. **58**(2): p. 205-216.
33. Daymond, M.R., *The determination of a continuum mechanics equivalent elastic strain from the analysis of multiple diffraction peaks.* Journal of Applied Physics, 2004. **96**(8): p. 4263-4272.
34. Valvoda, V. and M. Järvinen, *On the Harris texture index.* Powder Diffraction, 1990. **5**(4): p. 200-203.

35. Tomchik, C., et al., *High energy X-ray diffraction study of the relationship between the macroscopic mechanical properties and microstructure of irradiated HT-9 steel.* Journal of Nuclear Materials, 2016. **475**: p. 46-56.
36. Ungár, T. and A. Borbély, *The effect of dislocation contrast on x- ray line broadening: a new approach to line profile analysis.* Applied Physics Letters, 1996. **69**(21): p. 3173-3175.
37. Lind, J., et al., *Tensile twin nucleation events coupled to neighboring slip observed in three dimensions.* Acta materialia, 2014. **76**: p. 213-220.
38. Li, S., et al., *A brittle fracture mechanism in thermally aged duplex stainless steels revealed by in situ high-energy X-ray diffraction.* Materials Science and Engineering: A, 2019. **739**: p. 264-271.
39. Chen, S., et al., *Effects of thermal aging and low-fluence neutron irradiation on the mechanical property and microstructure of ferrite in cast austenitic stainless steels.* Acta Materialia, 2019. **179**: p. 61-69.
40. Badyka, R., et al., *Quantification of hardening contribution of G-Phase precipitation and spinodal decomposition in aged duplex stainless steel: APT analysis and micro-hardness measurements.* Journal of Nuclear Materials, 2019. **514**: p. 266-275.
41. Zhou, J., et al., *Quantitative evaluation of spinodal decomposition in Fe-Cr by atom probe tomography and radial distribution function analysis.* Microsc Microanal, 2013. **19**(3): p. 665-75.
42. Lach, T.G., et al., *Co-dependent microstructural evolution pathways in metastable δ-ferrite in cast austenitic stainless steels during thermal aging.* Journal of Nuclear Materials, 2018. **510**: p. 382-395.
43. Li, Z., et al., *Irradiation response of delta ferrite in as-cast and thermally aged cast stainless steel.* Journal of Nuclear Materials, 2015. **466**: p. 201-207.
44. Devaraj, A., et al., *Nanoscale phase separation in epitaxial Cr-Mo and Cr-V alloy thin films studied using atom probe tomography: Comparison of experiments and simulation.* Journal of Applied Physics, 2014. **116**(19): p. 193512.
45. Chen, Y., P.H. Chou, and E.A. Marquis, *Quantitative atom probe tomography characterization of microstructures in a proton irradiated 304 stainless steel.* Journal of Nuclear Materials, 2014. **451**(1-3): p. 130-136.
46. Vitek, J., et al., *Low temperature aging behavior of type 308 stainless steel weld metal.* Acta metallurgica et materialia, 1991. **39**(4): p. 503-516.
47. Ravel, B. and M. Newville, *ATHENA, ARTEMIS, HEPHAESTUS: data analysis for X-ray absorption spectroscopy using IFEFFIT.* Journal of synchrotron radiation, 2005. **12**(4): p. 537-541.
48. Booth, C. and F. Bridges, *Improved self-absorption correction for fluorescence measurements of extended X-ray absorption fine-structure.* Physica Scripta, 2005. **2005**(T115): p. 202.
49. Newville, M., *EXAFS analysis using FEFF and FEFFIT.* Journal of synchrotron radiation, 2001. **8**(2): p. 96-100.
50. Kelly, S., D. Hesterberg, and B. Ravel, *Analysis of soils and minerals using X-ray absorption spectroscopy.* Methods of soil analysis. Part 5. Mineralogical methods, 2008. **5**: p. 387-464.

51. Newville, M., *Fundamentals of XAFS.* Reviews in Mineralogy and Geochemistry, 2014. **78**(1): p. 33-74.
52. Schwarm, S.C., *Microstructural Evolution and the Resultant Mechanical Behavior of Duplex Stainless Steels*. 2018.
53. Schwarm, S.C., et al., *Characterization of phase properties and deformation in ferritic-austenitic duplex stainless steels by nanoindentation and finite element method.* Materials Science and Engineering: A, 2017. **680**: p. 359-367.
54. Weiss, B. and R. Stickler, *Phase instabilities during high temperature exposure of 316 austenitic stainless steel.* Metallurgical and Materials Transactions B, 1972. **3**(4): p. 851-866.
55. Sourmail, T., *Precipitation in creep resistant austenitic stainless steels.* Materials science and technology, 2001. **17**(1): p. 1-14.
56. Lo, K.H., C.H. Shek, and J.K.L. Lai, *Recent developments in stainless steels.* Materials Science and Engineering: R: Reports, 2009. **65**(4-6): p. 39-104.
57. Escriba, D.M., et al., *Chi-phase precipitation in a duplex stainless steel.* Materials Characterization, 2009. **60**(11): p. 1214-1219.
58. Chen, W.-Y., et al., *In situ TEM study of G-phase precipitates under heavy ion irradiation in CF8 cast austenitic stainless steel.* Journal of Nuclear Materials, 2015. **464**: p. 185-192.
59. Reese, E.R., et al., *Dose rate dependence of Cr precipitation in an ion-irradiated Fe 18Cr alloy.* Scripta Materialia, 2018. **146**: p. 213-217.
60. Ke, J.-H., et al., *Flux effects in precipitation under irradiation – Simulation of Fe-Cr alloys.* Acta Materialia, 2019. **164**: p. 586-601.
61. Fujii, K. and K. Fukuya, *Effects of radiation on spinodal decomposition of ferrite in duplex stainless steel.* Journal of Nuclear Materials, 2013. **440**(1-3): p. 612-616.
62. Chen, Y., et al., *The characterization of G-phase in Fe20Cr9Ni cast duplex stainless steel.* Materials Characterization, 2019. **149**: p. 74-81.
63. Zheng, C., et al., *Microstructure response of ferritic/martensitic steel HT9 after neutron irradiation: Effect of temperature.* Journal of Nuclear Materials, 2020. **528**.
64. Wagner, R., *Hardening in spinodally decomposed alloys.* Czechoslovak Journal of Physics, 1981. **31**(2): p. 198-208.
65. Cahn, J.W., *Hardening by spinodal decomposition.* Papers, 1963: p. 375.
66. Kato, M., *Hardening by spinodally modulated structure in bcc alloys.* Acta Metallurgica, 1981. **29**(1): p. 79-87.
67. Ardell, A., *Precipitation hardening.* Metallurgical Transactions A, 1985. **16**(12): p. 2131-2165.
68. Fischer-Cripps, A.C. and D. Nicholson, *Nanoindentation. Mechanical engineering series.* Appl. Mech. Rev., 2004. **57**(2): p. B12-B12.
69. Krumwiede, D.L., *Correlation of Nanohardness to Bulk Mechanical Tensile and Shear Properties through Direct Characterization and Comparison of Neutron-Irradiated Steels*. 2018, UC Berkeley.
70. Akhtanova, G., *NANOINDENTATION HARDNESS MEASUREMENTS OF ION IRRADIATED 21CR32NI AND 800H ALLOYS.* 2019.

71. Busby, J.T., M.C. Hash, and G.S. Was, *The relationship between hardness and yield stress in irradiated austenitic and ferritic steels.* Journal of Nuclear Materials, 2005. **336**(2-3): p. 267-278.
72. Queyreau, S., G. Monnet, and B. Devincre, *Orowan strengthening and forest hardening superposition examined by dislocation dynamics simulations.* Acta Materialia, 2010. **58**(17): p. 5586-5595.
73. Chen, Y., et al., *Void Swelling and Microstructure of Austenitic Stainless Steels Irradiated in the BOR-60 Reactor*. 2012, Argonne National Lab.(ANL), Argonne, IL (United States).
74. Tan, L. and J.T. Busby, *Formulating the strength factor α for improved predictability of radiation hardening.* Journal of Nuclear Materials, 2015. **465**: p. 724-730.
75. Csanádi, T., et al., *Orientation-dependent hardness and nanoindentation-induced deformation mechanisms of WC crystals.* Acta Materialia, 2015. **83**: p. 397-407.
76. Chen, T., et al., *The effect of grain orientation on nanoindentation behavior of model austenitic alloy Fe-20Cr-25Ni.* Acta Materialia, 2017. **138**: p. 83-91.

APPENDIX

Publication

A. Y. Lu, Z. Li, Y. Chen, Y. Yang, "Characterization of Ferrite Phase in Neutron Irradiated CF3 Cast Stainless Steels at dose of 5, 10, 20 and 40 dpa", to be submitted to Journal of Nuclear Materials, 2020.
B. Y. Lu, M. Warren, J. Terry, S. Li, Y. Chen, and Y. Yang, "Understand the thermal aging effect on mechanical response of duplex stainless steem using in-situ synchrotron wide-angle X-ray scattering" to be submitted to Journal of Nuclear Materials, 2020.
C. Li, Z,. Chen Y. *Rao A. S.*, Yang, Y. (2018), Effects of Thermal Aging and Low Dose Neutron Irradiation on the Ferrite Phase in a 308L Weld, In: Jackson J., Paraventi D., Wright M. (eds), Proceedings of the 18th International Conference on Environmental Degradation of Materials in Nuclear Power Systems –Water Reactors, pp 689-702, EDM 2017. The Minerals, Metals & Materials Series. Springer, Cham
D. Y. Yang and Z. Li, "Irradiation Response of the Ferrite Phase in CF3 Cast Stainless Steel", Transactions of the American Nuclear Society, v116, p 390-391, 2017, Transactions of the American Nuclear Society, ANS 2017.
E. ***Abstract for oral presentation***, Y. Lu, S. Li, Y. Chen and Y. Yang, Presentation Abstract "Understand the Phase Transformation and Mechanical Behavior of Thermally Aged and Neutron Irradiated Duplex Stainless Steels Using High-Energy X-ray Beamline Experiments" Accepted to TMS 2019
F. ***Oral presentation*****,** Y. Yang, "Irradiation Response of the Ferrite Phase in CF3 Cast Stainless Steel", American Nuclear Society Summer Meeting, San Francisco, CA, June 11-15, 2017
G. ***Oral presentation*****,** Y. Yang, "Effects of Thermal Aging and Low Dose Neutron Irradiation on the Ferrite Phase in a 308L Weld", 18th International Conference on Environmental Degradation of Materials in Nuclear Power Systems –Water Reactors
H. ***Oral presentation,*** Y. Yang, "Understand the phase transformation of thermally aged and neutron irradiated duplex stainless steels used in LWRs using advanced high energy X-ray Technologies.", NSUF 2016 Annual Review Meeting, DC, Nov 1-2, 2016

Graudate students:

Zhangbo Li, PhD, Materials Science and Engineering, University of florida, Gradauted in Dec 2017

Yu Lu, PhD candidate, Materials Science and Engineering, University of florida, Degree Expected: May 2020

Yashu Rao, PhD candidate, Materials Science and Engineering, University of florida, Degree Expected: May 2021